Constraining lateral thickness variations in Ganymede with JUICE

MSc Thesis

TU Delft

Daniel León Calliess

Constraining lateral thickness variations in Ganymede with JUICE

MSc Thesis

by

Daniel León Calliess

to obtain the degree of Master of Science
at the Delft University of Technology,
to be defended publicly on Thursday February 6th, 2025, at 09:30 AM.

Student number:	4869710	
Project duration:	March 10, 2024 – February 6, 2025	
Thesis committee:	Dr. ir. Marc Rovira Navarro,	TU Delft, supervisor
	Dr. ir. Dominik Dirkx,	TU Delft, chair
	Dr. ir. Wouter van der Wal,	TU Delft, external examiner

Cover: Leona Wehrenberg
Style: TU Delft Report Style, with modifications by Daan Zwaneveld

An electronic version of this thesis is available at http://repository.tudelft.nl/.

TU Delft

Preface

This thesis marks the culmination of a challenging yet incredibly rewarding journey, and I would like to take this opportunity to express my gratitude to those who have supported me throughout this endeavor.

First and foremost, I owe an immense debt of gratitude to my supervisor, Dr. Marc Rovira Navarro, whose guidance and expertise shaped this thesis into what it is today. Thank you for introducing me to this fascinating research topic and granting me the opportunity to contribute to your research on tides. I deeply appreciate your consistent support and thoughtful guidance during our weekly meetings, which proved invaluable to the success of this project. Your unwavering encouragement, coupled with your accessibility for feedback and questions at any time, has been a cornerstone of my progress. For all of this, I am profoundly grateful.

Secondly, I would like to extend my sincere thanks to Dr. Dominik Dirkx for his exceptional assistance with Tudat and for providing insightful comments and ideas during our meetings. Your input has been crucial in shaping and enhancing this work. Additionally, I wish to express my gratitude to Dr. Wouter van der Wal for serving on the committee and generously dedicating his time to review and evaluate my thesis.

I would also like to express my heartfelt gratitude to my family, whose loving support has been fundamental to me both personally and academically. Therefore, my deepest thanks go to my mother, Iris, and my brother, David. Thank you for being two strongstanding pillars in my life and for always caring and looking out for me. Your encouragement has been a guiding light, helping me navigate even the most challenging moments.

To my better half and longtime partner, Leona Wehrenberg, I am deeply thankful for your love, patience, and constant presence. Thank you for being my emotional anchor and a source of endless motivation and joy.

Lastly, I would like to extend my appreciation to all my friends. Thank you for providing me with laughter and perspective when I needed it most.

Completing this thesis would not have been possible without the support of these incredible people. I dedicate this work to all of you with heartfelt gratitude.

Daniel León Calliess
Delft, January 2025

Summary

The search for life beyond Earth is one of humanity's most profound scientific pursuits and drives space exploration. The icy moons of the outer planets in our solar system have recently received particular attention as several of them contain liquid water beneath their ice shells. For this reason, the exploration of icy moons and their potential habitability is one of the major targets of space agencies worldwide (eg. NASA and ESA). ESA's JUICE mission, currently on its way to the Jupiter system, will focus on characterizing the interior of Ganymede, an icy moon of Jupiter with a confirmed subsurface ocean. The structure of Ganymede's ice shell is critical to the question of habitability, since it influences the process of tidal heating, heat and material transportation in the interior, interactions between the ice and subsurface ocean and Ganymede's orbital evolution.

Tides raised by Jupiter on Ganymede deform its ice shell, creating time-varying variations in its gravitational field. JUICE will measure these signals with exceptional accuracy after entering a low circular orbit phase (GCO500). Previous research has mostly focused on studying tides with a spherically symmetric interior structure, limited to radially varying interior parameters. Lateral variations in the ice shells of icy moons have been found for Europa and Enceladus and can be maintained by the distribution of tidal heating and dynamic interactions inside the ocean and ice layers. The presence of lateral variations leads to a more complex tidal response. Different to a spherically symmetric body, where the tidal forcing and response wavelength are equal, the response modes are coupled in case of lateral variations and multiple wavelengths are excited. This research aims to answer the question whether JUICE measurements are precise enough to constrain lateral variations in the ice shell of Ganymede.

A covariance analysis is performed to obtain the estimated uncertainty of the additional tidal signals, produced by lateral variations, with respect to JUICE observations. The covariance analysis involves implementation of extended Love numbers into the Tudat software, distinguishing between forcing and response wavelength, and removal of the permanent tide from the signals. Synthetic range and Doppler observations are generated based on the expected mission trajectory, selected dynamical model and realistic measurements noise. An arc-wise orbit determination is set up spanning 100 days during the GCO500 phase, estimating the arc-wise state of JUICE and empirical accelerations, Ganymede's gravity field (up to degree 15) and gravitational Love numbers. The results indicate that tidal signals resulting from a degree 2 forcing can be measured with an accuracy of around 4×10^{-4}. This is true for both diagonal and off-diagonal mode coupled Love number (eg. k_{20}^{30} ...). The latter result is unexpected, since higher order responses are expected to produce lower signals. Furthermore, the current parametrization showed high correlation and difficulties in distinguishing the combined effect of two forcing signals at one response wavelength (eg. k_{20}^{20}, k_{22}^{20}).

A sensitivity analysis of Love numbers to the interior of Ganymede was done, studying the magnitude of tidal signals expected if lateral variations are present. It is also explored how sensitive these signals are to the interior structure. An interior model of Ganymede, consistent with current literature is built and the elastic response of Ganymede to a degree 2 forcing is calculated. The results showed that magnitude of additional signals arising depends on the amplitude of lateral variations, their wavelength and position inside Ganymede. The largest tidal signals result from lateral variations of degree 1 and 2 within the ice shell, notably from zonal (order=0) variations. For lateral variations with amplitudes of at least 5 % these signals are on the verge of the expected uncertainty (4×10^{-4}). More complex lateral variations would require amplitudes of 6 % to 17 %. It was also seen that lateral variations in the mantle and deeper layers produce a much weaker response, requiring very large lateral variations, thus showing that the tidal response is most sensitive to the ice shell.

Contents

List of Figures

List of Tables

Nomenclature

Abbreviations

Abbreviation	Definition
DSA	Deep Space Antenna
ESA	European Space Agency
FEM	Finite Element Method
GALA	Ganymede Laser Altimeter
GCO	Ganymede Circular Orbit
GPS	Global Positioning System
Gyr	Giga Years (1 Billion)
HAA	High Accuracy Accelerometer
JUICE	Jupiter Icy Moons Explorer
MESSENGER	Mercury Surface, Space Environment, Geochemistry and Ranging
NASA	National Aeronautics and Space Administration
NSR	Non-synchronous rotation
PM	Point mass
RMS	Root-mean-square
ROW	Roadmaps to Ocean Worlds
SH	Spherical Harmonics
SPICE	Spacecraft, Planet, Instrument, Camera-matrix, Events
SRP	Solar Radiation Pressure
3GM	Geodesy and Geophysics of Jupiter and the Galilean Moons experiment
...	

Symbols

Symbol	Definition	Unit
Latin symols A	Area	m^2
A_k	Kaula coefficient	-
C	Axial moment of inertia	kgm^2
C_D	Drag coefficient	-
$\bar{C_n}$	Mean degree power at degree n	m^4/s^4
C_{nm}, S_{nm}	Spherical harmonic coefficients of degree n and order m	-
$\bar{C}_{nm}, \bar{S}_{nm}$	Normalized spherical harmonic coefficients of degree n and order m	-
C_R	Solar radiation pressure coefficient	-
d^*	Distance between center of masses	m
E	Eccentric Anomaly	rad
e	Eccentricity	-
Fe	Iron	-
FeS	Iron-sulfide	-
G	Gravitational constant	m^3/kgs^2
GM	Gravitational parameter	m^3/s^{-2}

Symbol	Definition	Unit
g	Gravitational acceleration	m/s^2
g	Global parameters	-
$\mathbf{H}$	Design matrix	-
H	Thickness	m
H_{nm}	Lateral variations of degree n and order m	-
H_S	Atmosphere scale height	km
h_{nm}	Radial tidal displacement Love number at degree n and order m	-
$h(x)$	Nonlinear design matrix	-
i	Inclination	rad
J	Spring rigidity	GPa
J_2	Spherical harmonic coefficient at degree/order (2,0)	-
k_{nm}	Gravitational Love number at degree n and order m	-
$k^{nm}_{n_\alpha m_\alpha}$	Gravitational Love number at degree and order (n,m) due to forcing at degree and order (n_α, m_α)	-
$\mathcal{K}$	Real valued gravitational Love number	-
l	Local parameters	-
l	degree	-
l_{nm}	Tangential tide displacement Love number at degree n and order m	-
M	Mass	kg
M	Mean anomaly	rad
$\mathbf{M}$	Vector of non-conservative forces	N
$MgSO4$	Aqueous magnesium sulfate	-
m	Rotational parameter	-
m	Order	-
N_{nm}	Normalization factor of degree n and order m	-
N_r	Number of radial points	-
$NMoI$	Normalized moment of inertia	-
n	Degree	-
n	Mean motion	rad/s
P	Covariance matrix of estimated parameters	-
P_{nm}	Legendre polynomial of degree n and order m	-
$\bar{P}_{nm}$	Normalized Legendre polynomial of degree n and order m	-
p	Pressure	Pa
Q_{nm}	potential stress	GPa
R	Radius	m
$\mathbf{R}_{nm}, \mathbf{S}_{nm}, \mathbf{T}_{nm}$	radial spheroidal, tangential spheroidal and toroidal stress tensors	GPa
$\mathcal{R}(), \mathcal{J}()$	Real, Imaginary part of complex number	-
r	position vector	m
t	Time	s
t_{nm}	Toroidal tidal displacement Love number at degree n and order m	-
U	Vertical surface displacement	m
U	Gravitational potential	m^s/s^2
U_{nm}, V_{nm}, W_{nm}	radial spheroidal, tangential spheroidal and toroidal deformations	-
$\mathbf{u}$	Displacement vector	m
V_{nm}	Tidal Forcing at degree n and order m	m^2/s^2
v	viscosity	$Pa \cdot s$
$\mathbf{W}$	Weight matrix	-
$\mathbf{x}$	State Vector	-

Symbol	Definition	Unit
Y_n^m	Spherical harmonics at degree n and order m	-
$\mathcal{Y}_n^m$	Real valued spherical harmonics at degree n and order m	-
$\mathbf{z}$	Observation vector	-
γ	Tide induced libration	rad
Δ	Volume variation of particle	m^3
δ_{0m}	Kronecker delta	-
ϵ	Error vector	-
$\epsilon_{\mathbf{D}}$	Strain tensor	-
θ	Co-latitude	rad
κ	Adiabatic bulk modulus	Pa
λ	Longitude	rad
μ	Rigidity, Shear modulus	GPa
ρ	Residual vector	-
ρ	Correlation coefficient	-
ρ	Density	kgm^{-3}
σ	Cauchy stress tensor	Pa
σ	Uncertainty	-
Φ^T	Tidal potential	$[m^2/s^2]$
ϕ, φ	Longitude	rad
Ψ	Angle between vectors $\mathbf{r}$ and $\mathbf{d}^*$	rad
ω	Rotation rate	rad/s

1

Introduction

The search for life beyond Earth in the universe is one of humanity's most profound questions. Italian physicist Enrico Fermi posed the famous question of "Where is everybody?" in response to the seemingly silent and dead universe, given the infinite number of stars and planets out there. Answering the questions of whether life is rare, whether we are alone in the universe and how and where life emerges are part of the quest to understand our own origins. A key ingredient for life as we know is water, which is why the discovery of subsurface oceans under the ice shells of these moons was a major milestone in the search of life in our Solar system. Until the Cassini and Galileo missions to Saturn and Jupiter, these icy moons were considered frozen and lifeless. Clear evidence of global subsurface oceans present on Enceladus, Callisto, Europa, Ganymede and Titan and the possibility of similar conditions on other moons has reshaped our perspective of these ocean worlds.

In this context, the exploration of the icy moons in the outer solar system and search for life have been identified as one of the key goals for the future of space exploration. Both the National Aeronautics and Space Administration (NASA) and European Space Agency (ESA) define the exploration of icy moons in our Solar system as main science goal addressed in their future scientific framework, leading the development of new space missions for the next decades to come (Hendrix et al. 2019; Martins, Z. et al. 2021). The NASA Roadmaps to Ocean Worlds (ROW) group defines its main goal as to:

"Identify ocean worlds, characterize their oceans, evaluate their habitability, search for life, and ultimately understand any life we find."

This ambitious goal outlines a stepwise approach to exploring ocean worlds and assessing their potential habitability. Once an ocean is identified on a candidate world, the immediate focus shifts to characterizing the ocean's physical and chemical properties. This includes understanding how the ocean interacts with its surrounding environment, as these interactions provide essential clues about the system's potential to support life. The ice shell is of interest, since it determines the exchange of energy and material between the ocean and the surface, the evolution and dynamics of the underlying ocean and thus is crucial in assessing the habitability. One of the objectives in both NASA's and ESA's framework therefore specifically addresses the need to characterize the ice shell's properties in detail. This includes the spatial distribution of the ice shell thickness, its composition and rheology.

Europa Clipper and Jupiter ICy moons Explorer (JUICE) are two recently launched space missions on their way to the Jovian system to answer these research questions and significantly advance our understanding of the Jupiter and its moons. While NASA's Europa Clipper focuses on Europa, the European JUICE mission will investigate Ganymede in detail. Figure 1.1 shows the current state of knowledge of icy moons and the objectives leading to the search for life. Ganymede has been identified as an ocean world following the Galileo spacecraft, however its interior and ocean characterization remains on a basic level.

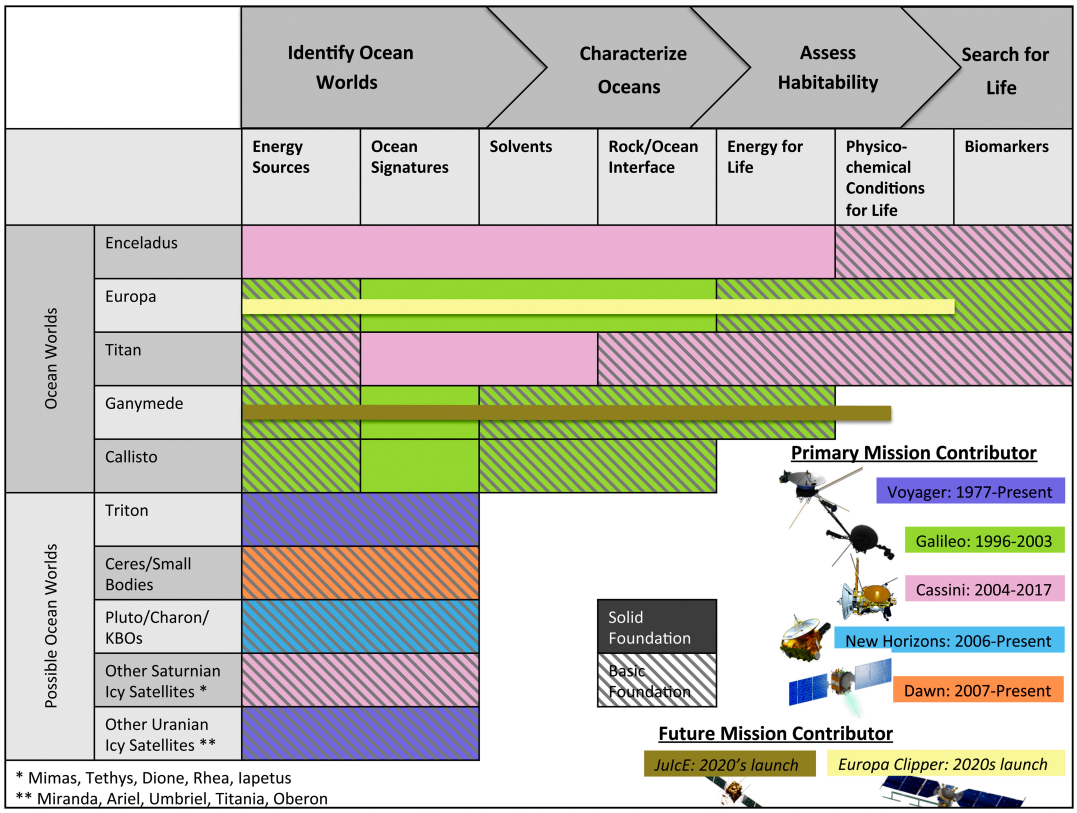

Figure 1.1: Current state of knowledge of each icy moon and (potential) target for life. Colors represent which missions provided the majority of information about each target. A solid color represents a solid foundation and a hashed color represents only a basic foundation. Image Credit: NASA Roadmap to Ocean worlds (Hendrix et al. 2019).

JUICE will be the first spacecraft to orbit a moon in the outer Solar System and allow to study the Jovian system with unprecedented detail. After arrival in 2031 and flybys of the other moons it enters a low circular orbit around Ganymede to characterize its interior. The 3GM (Geodesy and Geophysics of Jupiter and the Galilean Moons) radio science experiment allows to measure the gravitational field and tidal response of Ganymede. The tidal response of a body is linked to its interior structure, which is why studying the tidal response of Ganymede allows to constrain the interior and thus ice shell of Ganymede.

Traditionally, the tidal response is estimated by assuming that the interior parameters vary only in radial direction, assuming spherical symmetry. Relaxing this assumption by assuming that lateral variations might be present in its ice shell, leads to a more complex tidal response. The tidal response due to lateral variations produces additional tidal signals next to the main signal (from a spherically symmetric interior). These additional signals are much weaker but the accuracy of JUICE might make it possible to observe them and thus constrain the ice shell further. This thesis will investigate whether observations of the JUICE mission will be precise enough to pick up additional tidal signals and if these signals allow to constrain lateral variations in the interior of Ganymede.

The outline of the presented thesis is as follows: A literature review is found in Chapter 2, focusing on several key areas such as a historical perspective and most recent knowledge about Ganymede's interior structure. The extent of possible lateral variations on Ganymede, the concept of tides and their resulting deformation of a celestial body is discussed. The tidal response of spherically symmetric and laterally heterogeneous body are compared and the method to which tidal observations are used to infer interior properties. It is also shown how a spacecraft can measure tidal signals from orbit, with a special focus on the recently launched JUICE mission and its expected accuracy/uncertainty in obtaining the degree 2 tidal signals at Ganymede.

The thesis methodology is split into two parts. To assess if radio-tracking of JUICE allows to pick up the additional signals, arising from the presence of lateral variations in the ice shell, during its circular orbit phase, a covariance analysis is performed. This is found in Chapter 3. This results in the expected uncertainties of the gravitational Love numbers to the observations of JUICE. Chapter 4, presents a sensitivity study performed to investigate which tidal response and thus Love numbers are obtained for a range of lateral variations in the interior of Ganymede. Only the gravitational Love numbers are of interest, since they describe the tidal deformation of Ganymede to changes in its gravitational field that are then "felt" by JUICE and will perturb its orbit. Chapter 5 contains the overall conclusion and implications of this work and provides suggestions for future work on this topic.

2

Background

Before answering the question of whether future measurements taken by the JUICE mission could allow to constrain lateral variations in the ice shell of Ganymede, an overview over the relevant literature in this field is provided. This chapter presents a historical perspective on the knowledge of Ganymede and the most recent developments in the field of interior models of these icy moons in Section 2.1. A key part of this thesis is the relation of tidal forces on Ganymede to its interior structure, especially the effects of potential lateral variations. The concept of tides and how the tidal response of a body is related to its interior is in Section 2.2. Section 2.3 explores how tidal signals can be used to infer interior properties and assesses relevant literature on lateral variations in planetary bodies, parameter estimation from orbit estimation and the JUICE mission. The research questions are then introduced in Section 2.4 outlining the aim of the thesis.

2.1. The Interior of Ganymede

Ganymede is one of four Galilean satellites, discovered by Galileo Galilei in 1610. The moon is tidally locked to Jupiter and in a 1:2:4 mean motion resonance with two of the other Galilean satellites, Io and Europa. With a radius of 2631.2 km it is the largest moon in the solar system. Its interior structure consists of a dense iron core, a silicate rock mantle and a thick ice shell consisting of various high-pressure ices, that includes a subsurface ocean. Interesting characteristics of Ganymede are an intrinsic magnetic field, generated in its metallic core, that is unique to any solar system moon (Kivelson et al. 2002). Observations from the Hubble Space Telescope and evidence of an induced magnetic field suggest a potential subsurface ocean, sandwiched between the icy layers (Kivelson et al. 2002; Saur et al. 2015; Vance et al. 2014). The discovery of an ocean makes it an interesting target in the search for potential life. This section provides an overview over the current state of knowledge about Ganymede and interior models used in literature.

Prior to the flyby's of the Galileo spacecraft at Ganymede, there was only limited knowledge about its interior (Mueller and McKinnon 1988). Doppler radio observations of the Voyager and Pioneer missions at Jupiter allowed to estimate the gravitational parameter (GM), from which a mean density of roughly $1.940\,\mathrm{kgm}^{-3}$ was derived (Campbell and Synnott 1985). The mean density was used by various authors (e.g., (Null 1976) and (Schubert et al. 1981)) to infer that the interior structure must be differentiated and composed of roughly 60% rock and 40% ice.

The Galileo spacecraft and its six flyby's over Ganymede allowed to obtain further details of the gravitational field. (Anderson et al. 1996) fitted the observed radio Doppler signals to a basic orbital model, parameterized by Ganymede's gravitational parameter GM and the degree 2 coefficients of its spherical harmonics gravity field J_2 and C_{22}. Because these coefficients are correlated, an a-priori constraint on the ratio between both coefficients has been imposed ($J_2 = (10/3)C_{22}$). This constraint assumes Ganymede to be a tidally locked body in hydrostatic equilibrium, which is when the gravitational

forces are balanced by its internal pressure.

Assuming Ganymede is in hydrostatic equilibrium, the value of J_2 has been used to infer the moon's moment of inertia, which depends on its radial density profile. In this way, information on the gravitational field allows to compute the moment of inertia and get an idea of the interior mass distribution and thus interior structure.

The Radau-Darwin relationship gives a first approximation for the correspondence between the axial moment of inertia (C) normalized to MR^2 and J_2 (Helled et al. 2011):

$$NMoI = \frac{C}{MR^2} = \frac{2}{3}\left[1 - \frac{2}{5}\left(\frac{5m}{m+3J_2} - 1\right)^{1/2}\right] \tag{2.1}$$

where $m = \omega^2 R^3/GM$ is the rotational parameter, R the mean radius, M the mean mass and ω the rotation rate.

(Anderson et al. 1996) obtained a normalized moment of inertia (NMoI) of $C/MR^2 = 0.3105 \pm 0.0028$. This value of Ganymede is on the lowest side of planetary bodies in our solar system and underlines a strongly differentiated interior (Schubert et al. 2004), hence the heavy elements are located closer to the center. Using the NMOI, total mass, size, and other properties of ice and rock, interior models can be constructed that fit all the observations. One such a model is a three layer interior structure of Ganymede, proposed by (Anderson et al. 1996), containing a metallic core with radius 400 km to 1300 km, a silicate rock mantle and an 800 km thick layer of water-ice. Core compositions of either pure iron (Fe) or a combination of iron and sulfide (Fe-FeS) were proposed, with respective densities of 5150 kgm^{-3} and 8000 kgm^{-3}.

Galileo measurements also revealed a strong and unique intrinsic magnetic field (Gurnett et al. 1996; Kivelson et al. 1996), which could originate from dynamo action, magneto-convection or be due to remaining magnetisation of a previous active field (Schubert et al. 2004). The latter is excluded as source for the magnetic field on Ganymede (Crary and Bagenal 1998). (Schubert et al. 1996) argue that the intrinsic magnetic field is generated by dynamo action and thus requires an at least partially liquid inner core of iron or iron sulfide, where convection can occur (Schubert et al. 2004). Next to the permanent magnetic field, additional signatures are present, where (Kivelson et al. 2002) suggested an induced dipole moment excited by the time-varying Jupiter field as explanation. According to their studies, this response is consistent with an electrically-conducting subsurface ocean layer, at an estimated depth of 150 km.

(Sohl et al. 2002) extended the constant density three layer models with a more detailed approach implementing the equation of state for the ice shell, accounting for phase transitions in the ice shells. Using the available constraints of mass and moment of inertia, the core size was bound to 650 km to 900 km, depending on composition. The outer ice layer contains pressure-induced phase transitions into ice I, ice III, ice V, and ice VI layers (Journaux et al. 2020; Schubert et al. 2004). (Kuskov 2001) showed that the composition of the mantle can be described by L chondrites, in which case an iron-rich core is expected. The model of (McKinnon and Desai 2003) requires sub-solar composition of rock and iron in a differentiated Ganymede or small non-hydrostatic contributions of the mantle to the gravity field.

(Anderson et al. 2004) discovered that the second Galileo flyby (G2) Doppler data does not fit the second degree gravity models, thus additional contributions to the gravity field are required. Point mass anomalies at the surface were included by some authors (eg. (Anderson et al. 2004; Palguta et al. 2006)) to fit the G2 flyby line-of-sight Doppler accelerations. (Palguta et al. 2009) provided spherical disk mass anomalies that explain the mismatch of Galileo Doppler data of G2 flyby, proposing that positive mass anomalies may correlate with areas of darker terrain and vice versa. This is confirmed by recent studies of (Gomez Casajus et al. 2022) and (Hansen et al. 2022), who re-analyse the Galileo data and include data from the recent Juno spacecraft flyby with modern orbit determination techniques to update the gravity field models. A degree 2 gravity field is consistent with assuming hydrostatic equilibrium, while a field up to degree and order 5 is needed to fit all the data. The higher order gravity terms confirm the presence of non-hydrostatic features (eg. mass anomalies) found previously (Palguta et al. 2009). The

study of (Gomez Casajus et al. 2022) adjusted the flyby data to take into account possible errors from Io's Plasma Torus.

Similarly to other icy moons, Ganymede is thought to have a subsurface ocean (Soderlund et al. 2020). The presence of this ocean was detected by Galileo observations of an induced magnetic field, resisting the time-varying field of Jupiter, combined with aurora oscillations measured by the Hubble Space Telescope (Kivelson et al. 2002; Saur et al. 2015). (Schenk 2002) also attributed anomalous crater shapes to a presumably liquid layer below the outer ice shell. An electrically conducting ocean layer would require a minimum salt concentration of 0.9 gram MgSO4 per kg of water for an ocean depth of 150 km to 250 km (Soderlund et al. 2020).

The question of how such a liquid ocean could be sustainable on Ganymede is an ongoing research theme, involving its thermal and orbital history. Radiogenic heating, originating from radioactive decay in the iron core, is thought to play a major role, whereas the tidal forces are lower in magnitude than for Io and thus tidal heating plays less of a role in Ganymede's heat budget (Soderlund et al. 2020). (Bland et al. 2009) suggested that additional tidal heating could have been present in the past during periods of increased eccentricity in Ganymede's orbital evolution as it interacted with its neighbors Io and Europa (0.3 Gyr) (Downey et al. 2020). Evidence of its geological history and surface deformation due to tidal forces are seen in grooved terrain features with the formation of troughs and ridges. Additionally, the presence of other components such as salts or ammonia reduces its melting temperature and keeps it from freezing (Bland et al. 2009; Spohn and Schubert 2003).

(Vance et al. 2014) assessed the thickness of the icy layers, considering representative ocean compositions with aqueous magnesium sulfate (MgSO4). They inferred an upper ice layer between 13 km to 144 km, agreeing with the observed grooved terrain features on Ganymede (Hammond and Barr 2014). (Kamata et al. 2016) obtained a maximum shell thickness of the outer ice I layer of 155 km. Depending on the ocean salinity, different pressure-induced phases of water ice can form. These may be buoyant and separated by small regions of water as shown in Figure 2.1(Journaux et al. 2020). The salinity, composition and thickness of the ocean is only poorly constrained until new observations are made available (Soderlund et al. 2020).

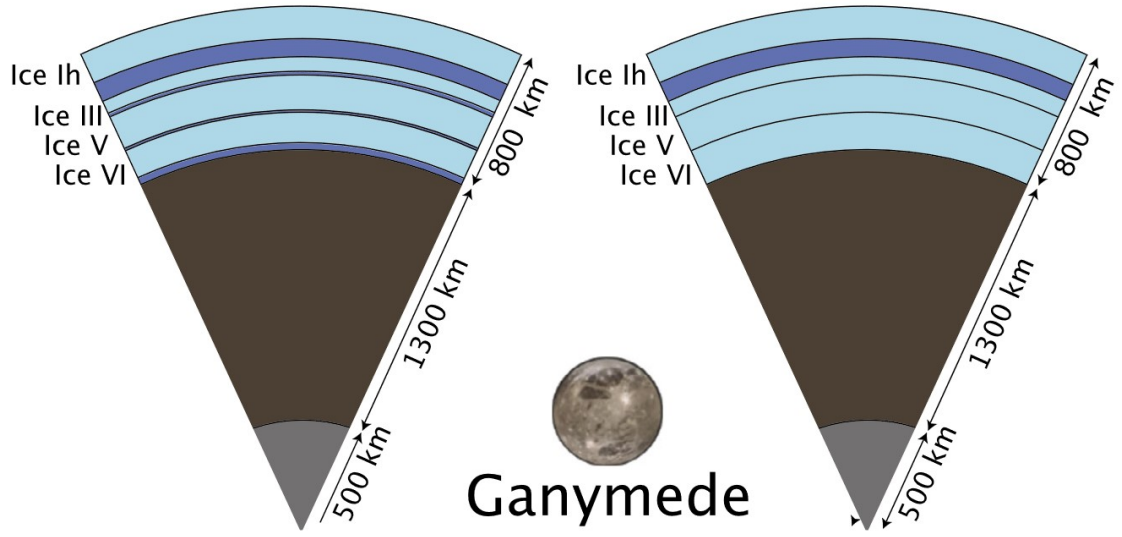

Figure 2.1: Possible spherically symmetric internal structures of Ganymede consistent with Galileo data. The right model includes a single subsurface ocean beneath the Ice Ih layer, while the left model proposes buoyant ice sheets in between small regions of liquid water ice. Image Credit: (Journaux et al. 2020)

Current interior models predominantly assume a 1-dimensional, spherically symmetric structure, meaning that internal properties vary solely with radius rather than with longitude or latitude. This approach simplifies the interior structure into some variation of the previously discussed layers (core, mantle, high-pressure ice, ocean, low-pressure ice) (A et al. 2014; Jara-Orué and Vermeersen 2016; Kamata et al. 2016; Vance et al. 2018; Wagner et al. 2013). Equations of state and thermodynamic

properties are used to model the icy layer's structure and composition, as detailed in works like (Choukroun and Grasset 2010). The interior models need to align with the avaiable constraints on mass and moment of inertia, mostly from Galileo data (Schubert et al. 2004). Figure 2.1 illustrates two potential interior structures of Ganymede, reflecting the current state of knowledge about its interior. Given the limited amount of observational data available, there is a large ambiguity in possible models that all fit the data until the next generation of spacecraft like JUICE arrive at Ganymede to provide more data (Grasset et al. 2013).

Although most interior models described in literature adopt the assumption of a spherically symmetric interior for Ganymede and other icy moons, this is not evidence based and rather due to resulting simplicity in the models. In fact, both planets and moons commonly exhibit lateral variations. The Earth's mantle and crust are heterogeneous as evident from seismic shear velocity observations (Ritsema et al. 2011). The crust of the Moon has lateral variations in density and porosity, correlating with the location of impact craters and crustal composition (Wieczorek et al. 2013). Mars features a north/south hemisphere dichotomy between the northern lowlands and southern highlands, reflecting in crustal thickness variation (Watters et al. 2007).

Lateral variations are also discussed as plausible for icy moons in literature. Measurements of the Cassini spacecraft at Titan and Enceladus, both icy moons of Saturn, reveal heterogeneities in their ice shells (Soderlund et al. 2020). Enceladus' shell thickness is thought to be $29 \pm 4km$ at the equator and only $7 \pm 4km$ at the south pole (Beuthe et al. 2016). This is confirmed by (Čadek et al. 2019), who find ice shell thickness ranging from 5 km to 30 km maintained by phase changes at the water/ice boundary. (Soderlund et al. 2024) present different dynamical interactions between the ocean, mantle and ice layers of icy moons that make thickness variations in the ice layers plausible (Soderlund et al. 2024).

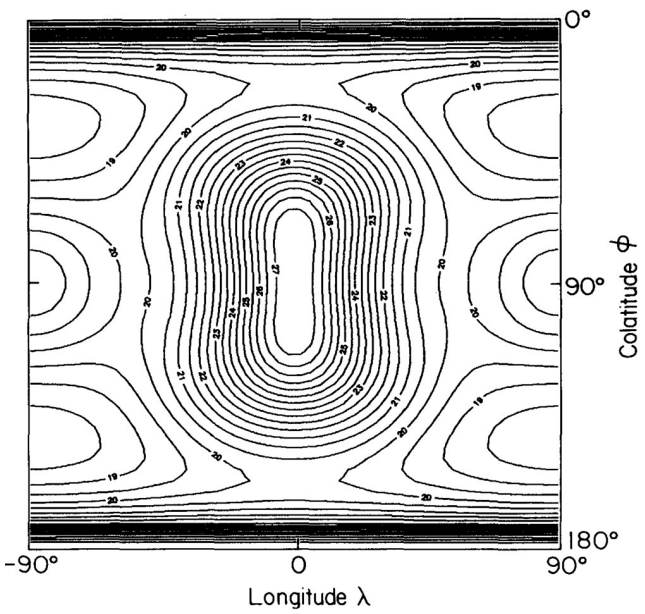

Figure 2.2: Equilibrium ice thickness of Europa's ice shell, assuming Maxwell rheology including heat flow from core. Units are kilometers. Image Credit: (Ojakangas 1989)

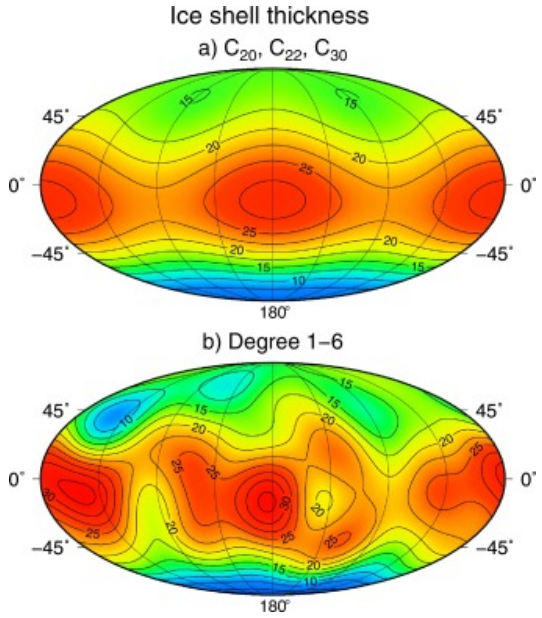

Figure 2.3: Ice shell thickness (km) of Enceladus obtained from a) the inversion of gravity and shape coefficients C20, C22 and C30. b) Ice shell thickness expanded to spherical harmonic degree 6. Image Credit: (Čadek et al. 2019)

(Ojakangas 1989) show that the tidal heat production in Europa's ice shell varies with longitude and latitude. As a result, they argue that if the outer ice shell is decoupled and in thermal conductive equilibrium, lateral variations in the ice shell thickness must naturally occur. (Nimmo et al. 2007) used limb profiles from Galileo images and could not find evidence for these lateral variations in Europa. They argue that either a thin ice shell (<35 km) would have small lateral variations not exceeding 7 km, thus too small to observe currently. Alternatively, they propose that there are no significant lateral variations present due to lateral flow or a convective ice shell smoothing them out over time.

Similar results were suggested for Io, where spatial variability of tidal heating induces significant lateral variations in the crust of about 10%, damped by convection processes (Steinke et al. 2020).

For Ganymede, the discovery of mass anomalies in its gravity field requires a non spherical shape (Anderson et al. 2004) and regional variations in heat flow could be possible, similar to Europa, as indicated by differences in crater relaxation patterns between the equator and the south pole (Singer et al. 2018). Although there is no information on the expected magnitude of lateral variations in Ganymede, these might be similar to other icy moons. Figure 2.2 shows the equilibrium ice shell thickness of Europa as computed by (Ojakangas 1989), while figure 2.3 shows the expected thickness variations in the shell of Enceladus, found by (Čadek et al. 2019). These examples give an insight into what kind of lateral variations may be expected in the interior of icy moons.

2.2. Tides and Love numbers

The tidal response of a body can reveal key information about its interior structure, evolution and origin. Tidal observations are a vital tool, especially when there are no in-situ measurements available. Except for the Earth, Moon and Mars where seismic data is available, most of the knowledge about planetary interiors in our solar system is derived from remote measurements of which tidal observations are an important tool that do not require any spacecraft landing and probing its surface. This section starts with a general introduction to the concept of tides in Subsection 2.2.1, while Subsection 2.2.2 presents the concept of tidal deformation and Love numbers, relating the interior of Ganymede to its tidal response.

2.2.1. The Tidal Force

Tides are the result of a gradient in the gravitational field across a celestial body, such as a planet or moon. As the gravitational force depends inversely on the distance, different parts of the body feel a slightly different gravitational pull. The side of the body facing the tide-raising body experiences a stronger pull than the opposite side, leading to a gradient of gravitational force. The force difference between an arbitrary point on a body and its center of mass, is defined as the tidal force and causes the body to deform and stretch. The tidal force is often expressed as the gradient of a scalar potential. According to (Kaula 1964), the tidal potential (Φ^T) caused by a secondary body (exerting the force) on a primary body (experiencing the force) can be described by a series of spherical harmonics:

$$\Phi^T = -\frac{GM^*}{\mathbf{d}^*} \sum_{l=2}^{\infty} (\frac{\mathbf{r}}{\mathbf{d}^*})^l P_n \cos(\psi) \tag{2.2}$$

where M^* and $\mathbf{d}^*$ are the mass of the secondary body and distance between both centers of masses. The potential is evaluated at a radial distance r to the center of the primary body and ψ the angle between both vectors $\mathbf{r}$ and $\mathbf{d}^*$. P_n is the Legendre polynomial function at degree n. The tidal potential is usually rewritten in a more useful way if the primary body orbits the secondary. In this case, $\mathbf{d}^*$ and ψ can be replaced with the orbital elements of the secondary body, see (Kaula 1964).

The amplitude of this tidal potential at the surface of the primary scales with the mass of the secondary body (M^*) and the ratio of its radius (R) and distance to the secondary body ($(r/\mathbf{d}^*)^n$). Because the tidal force decreases with distance from Jupiter, Io and Europa experience larger tidal potentials than Ganymede. As usual when working with spherical harmonics, degree 0 ($n = 0$) corresponds to a complete sphere, while higher degree terms correspond to smaller features. The amplitude of higher degree tidal terms also decreases rapidly. For this reason, the tidal effects on Ganymede can be safely considered using only the degree 2 tidal forcing effects by Jupiter, neglecting higher order terms.

After expressing Equation 2.2 in Jupiter's orbital elements with respect to a frame fixed to Ganymede and simplifying, the tidal potential can be expressed as shown in Equation 2.3. Ganymede's mean orbital eccentricity oscillates around ($e = 0.0015$) and its obliquity oscillates around ($i = 0.03$) with a maximum not above ($i = 0.06$) (Baland et al. 2012). Due to the low eccentricity and obliquity of Ganymede's orbit, only first order terms in eccentricity and obliquity are considered, as well as the effect

of non-synchronous rotation (NSR) on the eccentricity and obliquity tides (Jara-Orué and Vermeersen 2011).

$$\Phi^T = (nR)^2 \left[\Phi_0^T + \Phi_{ns}^T + \Phi_{e1}^T + \Phi_{e2}^T + \Phi_i^T\right] \tag{2.3}$$

where n is the mean motion of Ganymede's orbit. The individual expressions in this equation are described in (Jara-Orué and Vermeersen 2011).

There are several tidal effects that need to be introduced and the focus will be put on tides raised by Jupiter on Ganymede. The tidal potential in Equation 2.3 can be split into several constituents, a static time-invariant part (Φ_0^T) with zero frequency and a series of dynamic time-varying tides. (Φ_{ns}^T) describes the effect of NSR on the tidal potential and (Φ_{e1}^T, Φ_{e2}^T, Φ_i^T) the effects of eccentricity and inclination of Ganymede's orbit. If Ganymede's orbit was purely circular and co-planar to Jupiter's equatorial plane, then the relative position of Jupiter as seen from any point on Ganymede' surface would remain fixed, creating a constant tidal force. This constant tidal force creates a permanent tidal bulge (corresponding to J_2 and C_{22}) on Ganymede pointing in direction of the tide rising body (Jupiter). This static component is seen in both our Moon and icy moons, which have a slightly elongated shape due to their permanent tidal bulge.

Dynamic tides are caused by changes in the position of the primary with respect to the secondary, resulting in a periodically changing tidal potential along the orbit. The diurnal tides vary once per orbit with a period of roughly 7 days for Ganymede. For a moon in synchronous rotation $\Phi_{ns}^T = 0$ and these changes are the result of eccentricity and inclination of the orbit. Synchronous rotation refers to an equilibrium rotation state in which the spin rate equals the orbital period, which is the case for the Galilean satellites (Van Hoolst et al. 2024). NSR becomes a relevant and time-dependent part of the potential if a decoupled ice shell were to rotate non-synchronously with respect to the orbital rate (Wahr et al. 2009). This phenomenon occurs over timescales much larger than the orbital period, eg. for Europa the westward migration of the tidal buldge would take around 10000 years (Hoppa, Greenberg, et al. 1999)

For non-circular orbits ($e > 0$), eccentricity tides are caused by the elongation of the orbit and resulting varying orbital distance and velocity. There are two effects of an elliptic orbit, producing eccentricity tides (Φ_{e1}^T and Φ_{e2}^T). The variation in orbital distance between Ganymede and Jupiter causes the amplitude to vary, while the change in velocity over the orbit results in a longitudinal movement (libration) of Jupiter as seen from Ganymede's surface. If the orbit of the moon has an inclination (i) with respect to the equatorial plane of Jupiter ($i > 0$), there is a latitudinal libration over time of Jupiter's subplanet point as seen from Ganymede (Rovira-Navarro 2022), producing obliquity tides (Φ_i^T).

For a synchronous rotating moon in an eccentric orbit, the dynamic component of the tidal potential is given in Equation 2.4. Other tidal components can arise due to non-synchronous rotation or librations. Tidal effects due to non-synchronous rotation are neglected, these are on timescales much larger than of our interest and obliquity tides are neglected due to their very small amplitude compared to eccentricity tides. The term $O(e^2)$ indicates that higher order terms of the eccentricity tides are also neglected. Lastly, Ganymede is also subject to moon-moon tides raised by its neighbouring moons, but these tidal potentials are several orders of magnitude lower than the effect of Jupiter.

$$\Phi^T = r^2\omega^2 e[-\frac{3}{2}P_2^0 cos(\theta)cos(\omega t) + \frac{1}{4}P_2^2 cos(\theta)[3cos(\omega t)cos(2\phi) + 4sin(\omega t)sin(2\phi)]] + O(e^2) \tag{2.4}$$

ω is the orbital frequency, t is time, θ and ϕ are co-latitude and longitude. The associated Legendre function P_n^m is evaluated at degree n and order m (Kamata et al. 2016; Kaula 1964).

2.2.2. Tidal Deformation and Love numbers

This section introduces the concept of tidal deformation and Love numbers on an introductory level. A detailed explanation on how the tidal response of a body and its corresponding Love numbers are

derived is presented in the methodology in Section 4.2. In this way the focus of this Chapter is assessing the current state of literature while the detailed derivations are discussed in the methodology.

In response to the acting tidal potential Φ^T, the interior of Ganymede deforms periodically. The response of a celestial body to a perturbing tidal potential can be described by non-dimensional complex numbers called Love Numbers, first described by (Love 1911). The tidal potential of Jupiter, see equation 2.4, causes a vertical surface displacement $U(R, \theta, \varphi)$and a perturbation of the body's gravity field at the surface $\Phi(R, \theta, \varphi)$. R is the radius, θ and φ the colatitude and eastward longitude in body fixed frame. The tidal forcing potential is proportional to the deformation and depends on the Love numbers:

$$U = \frac{h\Phi^T(R, \theta, \varphi)}{g} \qquad \Phi = k\Phi^T(R, \theta, \varphi) \tag{2.5}$$

g is the gravitational acceleration at the surface and h and k are the radial displacement and gravitational Love number. The Love numbers indicate how much the body deforms under the tidal potential and depend on the interior properties. This approach assumes a spherically symmetric interior in which the interior properties vary only with distance from the center. The tidal potential is a sum of spherical harmonics and therefore Love numbers are defined at each spherical harmonic degree. Commonly used in literature are the Love numbers k_2, h_2, relating the tidal potential at degree 2 induced by Jupiter, to the resulting degree 2 response.

A realistic interior structure of Ganymede would be laterally heterogeneous and not limited to the assumption of a spherically symmetric body, as described in Section 2.1. The corresponding tidal response of such a body is more complicated to solve, since the tidal response modes are coupled and a tidal forcing with a certain degree/order also induces responses at other wavelengths. The concept of Love numbers has to be extended when lateral variations are used and this is in detail described in Section 4.2.

The tidal response of a body with lateral heterogeneity can be solved numerically with finite element methods (FEM) see (A et al. 2014; Berne et al. 2023; Berne et al. 2023). The governing equations are solved over a large grid of elements, making these methods computationally expensive. Alternatively, the traditional spectral method used for spherically symmetric bodies (see Section 4.2.1, (Sabadini et al. 2016)) can be extended to lateral variations. Spectral methods solving bodies with lateral heterogeneity are limited to small amplitude interior variations when using perturbation theory (Qin et al. 2014) or to a thin outer ice shell as in (Beuthe 2018). (Rovira-Navarro et al. 2024) present a spectral method that is computationally efficient and able to deal with high amplitude lateral deviations.

The software LOV3D computes the tidal response of laterally heterogeneous bodies using the spectral method and extended Love numbers as described by (Rovira-Navarro et al. 2024). In this way the effect of a non spherically-symmetric interior can be studied by observing all coupled response modes that may arise. The method of LOV3D is described in detail in Section 4.2.

2.3. Inferring Interior Properties from Tidal Observations

The relation between the tidal response and interior properties defining a planetary body can be used to probe the interior using spacecraft observations. A given interior and forcing potential produce a unique tidal response spectra that could be measured to obtain information about the body's interior. Examples of what can be learned from studying tidal observations and the concept of tidal tomography are introduced in Subsection 2.3.1. 2.3.2 follows with a discussion on the tidal constraints and expected Love numbers on Ganymede, the sensitivity of Love numbers to interior properties and implications for the use of tidal tomography to recover lateral heterogeneity in Ganymede. Subsection 2.3.3 details how tidal signals are measured from an observing spacecraft with a special focus on the role of the JUICE mission. The literature overview and background into the context of this research is concluded with the introduction of the research questions in Subsection 2.4.

2.3.1. Tidal Tomography

Before explaining the theory behind measuring tidal signals from spacecraft observations, a few examples are given on how studying tidal observations have helped to gain valuable information about the interior of some planets and moons.

Mercury's inner core size and core mantle boundary temperature have been constrained from interior models based on tidal observations of the Mercury Surface, Space Environment, Geochemistry and Ranging (MESSENGER) spacecraft (Padovan et al. 2014; Steinbrügge et al. 2018). Earth's deep-mantle buoyancy has been studied from Global Positioning System (GPS)-based measurements of surface deformation, caused by tidal forces of the Sun and Moon. The tidal deformation measured is sensitive to regions of varying density in its mantle (Lau et al. 2017). The radial structure of the lunar mantle was constrained from non-degree 2 tidal signals in satellite data (Zhong et al. 2012) and the process of tidal dissipation in its interior was studied with lunar laser ranging measurements from Earth (Williams and Boggs 2015). Body tides on Titan, exerted by Saturn, and the resulting pattern of diurnal tidal stresses were computed and found in agreement with the observed cryovolcanism on its surface (Sohl et al. 2014).

On icy moons tidal forces play in important role for their orbital evolution and the resulting tidal stresses are related to tectonic activities on the surface. Tidal dissipation is a source of heat, which can result in the formation of subsurface oceans, that might be important to life (Bagheri et al. 2022). On Europa the presence of a liquid layer underneath the ice shell is hypothesized to explain the amplitude of observed tensile cracks at the surface in response to variations in tidal stresses (Hoppa, Tufts, et al. 1999). Furthermore, the thickness of its ice shell was derived by the combination of tidal gravity measurements obtained from spacecraft tracking and surface displacement observations obtained from altimetry data (Wahr et al. 2006). The existence of a global sub-surface magma ocean on Io was recently precluded from Juno and Galileo flyby data (Park et al. 2024). The JUICE mission will go into orbit around Ganymede and measure its tidal response, allowing to determine the ice shell thickness, the subsurface ocean, composition, high-pressure ice layers and even potential lateral variations in its interior (Van Hoolst et al. 2024).

For a laterally-varying elastic body subject to a degree 2 forcing, additional tidal signals at other degrees arise that depend on the interior structure (Zhong et al. 2012). Tidal tomography refers to using observations of these additional tidal signals to infer the 3D structure of a planetary body, similar to seismic tomography. This inverse technique allows to map the measured tidal response spectra back to a possible 3D structure, which is challenging given the low amplitude of these additional tidal signals.

To understand if tidal tomography could be used to recover information about possible lateral variations from tidal observations on Ganymede, we need to understand both the sensitivity of the tidal response and corresponding Love numbers to the body's interior parameters as well as the observation accuracy of observing these tidal signals, which are the central two parts of this thesis. The degree to which this is possible depends on high quality observations of the near-surface gravity field of Ganymede, such that the gravitational tidal signals can be determined accurately enough to distinguish small variations among different tidal response modes. The recently launched JUICE mission presents a new opportunity for this case as it will measure the tidal response with unprecedented accuracy (Cappuccio et al. 2020).

2.3.2. Sensitivity of Love Numbers to Interior Structure

Current literature has focused mostly on measuring and interpreting the classical degree 2 Love numbers h_2 and k_2 of icy moons, which can be used to obtain information about the ice shell thickness or presence of a subsurface ocean, assuming a spherical symmetric elastic body. Detailed characterization of the geophysical parameters of the ice shell and ocean is limited due to the ambiguity of possible interior configurations corresponding to the same Love numbers (Jara-Orué and Vermeersen 2016).

The tidal surface displacement on Ganymede could show peak-to-peak variation as large as 7 m, depending on the ice rigidity, if a liquid ocean exists that decouples the ice shell from the remaining interior. Without an ocean, the expected tidal amplitude is much less with 0.5 m (Moore and Schubert

2003). Measuring the amplitude of h_2 would thus allow to identify a subsurface ocean. Ganymede models including an ocean result in h_2 values ranging from 1.1 to 1.6 (Kamata et al. 2016; Moore and Schubert 2003; Steinbrügge et al. 2015).

Similarly to h_2, determination of k_2 would equally allow to confirm the presence of an ocean on Ganymede. The magnitude of k_2 for Ganymede is expected to be less than 0.1 without an ocean and between 0.3 to 0.6 including an ocean (Moore and Schubert 2003; Vance et al. 2018). Assuming an ocean is present, both Love numbers are primarily sensitive to the thickness of the outer ice shell and ocean density, the latter parameter has a stronger influence on k_2 (Jara-Orué and Vermeersen 2016). After these major response parameters ice shell rigidity and density follow, while the thickness and configuration of deeper interior layers shows much less effect on the Love numbers, particularly h_2 (Jara-Orué and Vermeersen 2016; Steinbrügge et al. 2015; Van Hoolst et al. 2024; Vance et al. 2018).

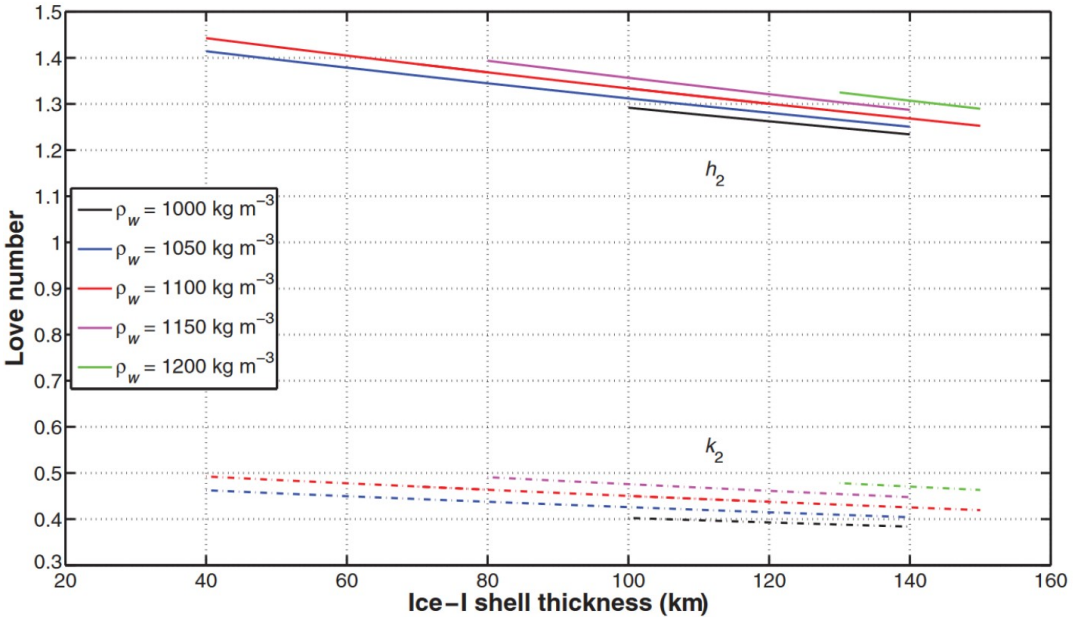

Figure 2.4: Magnitude of degree 2 Love numbers (k_2, h_2) as a function of ice shell thickness for different ocean densities. Density of ice shell is taken as $\rho_{ice-I} = 937 kgm^{-3}$ and ice rigidity $\mu_{ice-I} = 3.5 GPa$. Image Credit: (Jara-Orué and Vermeersen 2016)

Figure 2.4 shows the expected values of k_2 and h_2 as calculated by (Jara-Orué and Vermeersen 2016) for different shell thickness and ocean densities, the two dominant response parameters. The magnitude of both Love numbers decreases linearly with increasing shell thickness, which means there is a stronger response to the tidal forcing. The effect of ocean density can be large, especially for k_2. An increased ocean density results in larger magnitudes of both Love numbers and leads to changes of up to 6 % and 23 % for h_2 and k_2 in the evaluated density range of 1000 kgm^{-3} to 1200 kgm^{-3}. Thus, k_2 could be used to also constrain the ocean density, as was done for Titan by (Mitri et al. 2014). The density of the ice shell is far less important in this regard (Jara-Orué and Vermeersen 2016).

Larger values of the ice shell rigidity (μ) increase the magnitude of both Love numbers and also cause a stronger sensitivity to the ice shell thickness, corresponding to a steeper slope in Figure 2.4. For a large ice shell of 150 km, values of the k_2 Love number range from 0.32 to 0.47 using ice-I rigidities ranging from 1 GPa to 10 GPa. The ice rigidity is rather well constrained at around 3.5 GPa and therefore does not pose a large uncertainty (Steinbrügge et al. 2015). The effect of size and density of the HP ice layer on the Love numbers is low, while the sensitivity of the deeper layers on the magnitude of Love numbers is not noticeable (Kamata et al. 2016).

The ice viscosity is not well constrained and has a large influence on the magnitude of Love numbers. The models of (Moore and Schubert 2003) show that below a viscosity of about 1×10^{14} Pa · s the ice shell transitions from being elastic to a more fluid-like (visco-elastic) response and the Love numbers would be identical with or without an ocean. For low ice-I viscosity, the sensitivity of the magnitude of both Love numbers on ice thickness and rigidity variations would be greatly reduced, corresponding to more

horizontal lines in Figure 2.4. A visco-elastic response of Ganymede's ice shell is deemed unrealistic since higher temperatures of the shell would be required that are inconsistent with current studies estimating a surface temperature of 117 K (Steinbrügge et al. 2015; Van Hoolst et al. 2024).

With the expected accuracy of the instruments on the JUICE mission, the h_2 Love number could be measured to within 2 % assuming an ocean is present. This would allow to constrain the ice shell thickness to about ±30 km, assuming the ocean density and ice rigidity are known (Steinbrügge et al. 2015). Doing this with k_2 is less promising. (Wahr et al. 2006) propose a combined analysis of Love numbers using the linear combination $(1 + k_2 - h_2)$ for tides on Europa to constrain the ice shell thickness. This also works for Ganymede and could reduce the uncertainty to ±20 , as both Love numbers show slightly different sensitivity to ocean density and ice rigidity (Steinbrügge et al. 2015).

In the case of a laterally varying interior structure of Ganymede, a degree 2 forcing potential of Jupiter excites also non degree 2 tidal response modes and the overall response is more difficult to interpret (Van Hoolst et al. 2024). For instance, a degree 1 lateral variation in interior structure also causes changes in the degree 2 response, due to first order coupling (Rovira-Navarro et al. 2024; Zhong et al. 2012). This means that, next to the spherically symmetric response, a laterally varying Ganymede can have different tidal responses at different orders and also additional signals contributing to the degree 2 k_2 Love number (eg. additional first-order contributions of a degree 1 lateral variation). To correctly interpret tidal data obtained from JUICE, these effects have to be taken into account (Van Hoolst et al. 2024).

(A et al. 2014) compute the additional tidal response for Ganymede in case 3D thickness variations in the interior are present. They find that the additional tidal response is small and separating the spherically symmetric result from the additional signals allows to confirm the presence of an ocean (A et al. 2014) and constrain the ice shell thickness. In case lateral variations are present in Ganymede, the Love numbers would differ in order of the response, thus if one measures k_{20}, k_{21} and k_{22} much more can be learned about lateral variations, since these would be equal for a spherical symmetric body (Rovira-Navarro et al. 2024). Measuring the full tidal response can help to distinguish these overlapping tidal signal effects. The tidal response decreases in magnitude with order, hence only leading terms of the higher order additional response could be measured. While the amplitude of an additional tidal signal is stronger for the Moon and Mercury, changes in the mean shell thickness of 50 % could produce a signal of ~0.1 % to 1 % in Ganymede (Rovira-Navarro et al. 2024).

2.3.3. Observing the Tidal Response of Ganymede

The tidal response of a planetary body like Ganymede can be measured from an observing spacecraft. Two main tidal effects can be measured from orbit, the amplitude of radial tidal deformation corresponding to Love number h_2 and the change in the gravitational potential induced by the mass redistribution following the external tidal potential, corresponding to Love number k_2. The time-varying radial surface displacement can be measured using spacecraft altimetry, assuming there are enough crossover points where the spacecraft revisits the same point on the surface and the tidal potential is known. The time-dependent gravitational potential induced by the tidal forcing directly affects the spacecraft trajectory. Observing the spacecraft orbit over time allows to estimate the gravitational Love numbers. This requires precise knowledge of the spacecraft trajectory. Measuring the tidal signal in the gravitational field of Ganymede is easier than determining the surface deformation (Van Hoolst et al. 2024).

The gravitational Love numbers are estimated as parameters in the process of precise orbit determination, reconstructing the spacecraft trajectory from available observations. This can be done from both flyby's as done for the Galileo and Juno missions or using an orbiting spacecraft around the body like JUICE will do for Ganymede. In the process of orbit determination, the parameters controlling the spacecraft trajectory are adjusted to fit the given observations. The dynamical model includes all relevant forces acting on the spacecraft, part of which are the time-dependent changes in the gravitational field due to tides. As observation data, very accurate range and range-rate measurements can be obtained through radio tracking of the spacecraft from ground stations on Earth. Using least-squares, the parameters of the dynamical model are fit to the observations. A set of selected parameters to estimate typically include local parameters such as the spacecraft state (position and velocity of the orbit) and global parameters like spherical harmonic coefficients of the gravity field among others. Including

the time-dependent tides in the dynamical model allows to include the gravitational Love numbers as estimated parameters.

JUICE (JUpiter Icy Moons Explorer) is a European Space Agency (ESA) mission to the Jovian system, launched on 14 April 2023, and the first European mission to the outer solar system. Upon its arrival in 2031, it will perform a detailed investigation of the Jovian system, which serves as a miniature solar system, and answer questions about the origins and conditions of life and our solar system. After arrival to Jupiter, it will perform 2 flyby's of Europa, 12 of Callisto and 15 around Ganymede before entering into orbit around Ganymede, which will be its primary focus of investigation (Grasset et al. 2013; Van Hoolst et al. 2024).

Detailed characterization of Ganymede and its interior will be performed during the final 130 day orbital phase around Ganymede. The goal is investigating the ocean and ice shell and these detailed studies on the interior require a close distance to the surface to obtain high accuracy gravity field and tidal deformation measurements. This includes first a circular orbit with an average altitude of 490 km (GCO500 phase) starting on 21st May 2035 for 100 days. The original mission plan has been extended to include a lower 200 km orbit phase (GCO200), due to a successful launch performance. This will be performed during the final 30 days and both at an inclination of 102 °. If resources allow, the GCO200 orbit could be extended beyond the 30 day schedule or lower altitude orbits might be included (Boutonnet et al. 2024).

JUICE carries a collection of state-of-the-art instruments to collect imaging, geophysical, magnetic and plasma measurements among others [1]. The Ganymede Laser Altimeter (GALA) will measure the amplitude of the time dependent radial surface displacements from orbit, which allows to estimate the displacement love number h_2. Using a cross-over approach the range total error of the range measurements will be about 7 m which allows to determine h_2 to an uncertainty of 2% (Steinbrügge et al. 2015).

The Gravity & Geophysics of Jupiter and Galilean Moons (3GM) radio science instrument performs geophysics and geodesy science at Ganymede its neighbors. Its objectives during GCO500 and GCO200 are to determine the static gravity field of Ganymede up to degree 30 and its rotational state, the tidal Love numbers and the ephemerides of the Galilean moons. To do this a two-way radio link is established between JUICE and a ground station on Earth, enabling pseudo-noise range and Doppler shift (range-rate) measurements with the Ka-band transponder (Cappuccio et al. 2025). A high-accuracy accelerometer (HAA) is used to estimate and account for the disturbance of propellant sloshing during the orbit reconstruction. The orbit of JUICE is reconstructed using these radio signals as observations together with a dynamical model and an estimation filter. This allows to estimate the magnitude of Love numbers, gravity field coefficients and other parameters affecting the spacecraft trajectory and thus study the interior of Ganymede.

The estimation of higher-order gravity fields allows to re-assess the assumption of hydrostatic equilibrium and the tidally-induced gravitational response allows to estimate the gravitational Love number k_2 (Cappuccio et al. 2020). Precise radio tracking is required to reconstruct the spacecraft orbit and estimate these parameters, as well as provide an accurate reference orbit for the GALA measurements (Steinbrügge et al. 2015). Together these two instruments allow to identify a subsurface ocean, characterize the ice-I shell and obtain information about heat dissipation through the tidal quality factor (Q) (Kamata et al. 2016).

The precise orbit reconstruction of JUICE is done via accurate range and range-rate measurements provided by a two-way Ka-band radio link with 34.5 GHz uplink and 32.2 GHz downlink. Range and range-rate (Doppler) observations are available at an accuracy of 0.012 mm/s at 60 s integration time and 20 cm over a few seconds, respectively (De Marchi et al. 2022). 9 h of tracking time is allocated for gravitational measurements each day using the 2.5 m High Gain Antenna (HGA) (De Marchi et al. 2022). ESA's Deep Space Antenna 3 (DSA 3) in Malargue, Argentina is used for communciations as the only ground station able to provide the multi-frequency radio link (X/X, X/Ka, Ka/Ka). These multi-frequency links allows to cancel ionospheric effects and interplanetary plasma noise (Bertotti, B. and Comoretto, G. 1993).

[1] https://www.esa.int/Science_Exploration/Space_Science/Juice/Juice_factsheet, Retrieved 10/05/2024.

The 3GM science team estimate the expected accuracy of JUICE to one standard deviation and find formal uncertainties of: $\sigma_{GM} = 3.8{*}10^{-4} km^3/s^2$ for the gravitational parameter, $\sigma_{J_2} = 8.6{*}10^{-10}$ for J_2 and $\sigma_{k_2} = 1 * 10^{-4}$ for the real part of k_2. Trajectory reconstruction of JUICE in the radial-normal-tangential (RTN) frame leads to 3D root-mean-square (RMS) errors of ~1 m in position and $\sim 1 \times 10^{-6}$ m/s in velocity (Cappuccio et al. 2020). If the predicted accuracy of $\sigma_{k_2} = 1 * 10^{-4}$ is not overly optimistic, this would be on the order of 0.1 % of Ganymede's actual Love number k_2. This level of accuracy opens the promising opportunity for JUICE to detect additional tidal responses caused by lateral variations in the interior such as k_{20}^{20}, k_{20}^{22} (Rovira-Navarro et al. 2024).

2.4. Research Questions/Aim

This chapter has shown that tidal observations have become a fundamental tool in studying the interior of planetary bodies in our Solar system. The recently launched JUICE mission will reach Jupiter and its icy moons in 2031 after which it will perform detailed geophysical studies of Ganymede. This includes the characterizing its ice shell and subsurface ocean by measuring the tidal response (Van Hoolst et al. 2024). The 3GM instrument in particular, will study the effect of tides on the orbit of JUICE and allow to estimate the gravitational Love number k_2 (Cappuccio et al. 2020).

This approach and most of current literature assume the interior properties to be spherically symmetric. The presence of lateral variations in Ganymede's interior significantly alters the tidal response and creates response modes at all wavelengths, requiring the introduction of extended Love numbers. Lateral variations are likely to exist in Ganymede's ice shell and were already proposed for other icy moons such as Enceladus (Čadek et al. 2019) or Europa (Ojakangas 1989). Lateral variations could be sustained by dynamical processes (eg. periodic melting) of ice and the pattern of tidal heating induced. Tidal tomography might make it possible to recover lateral variations in Ganymede after measuring the additional tidal signals that these would create. This was already proposed as promising technique for Ganymede long before the JUICE mission (A et al. 2014). The additional tidal signals will likely be small in amplitude, however the expected accuracy of JUICE ($\sigma_{k_2} = 1 * 10^{-4}$) offers an existing research case in this regard.

The development of new and more efficient spectral method compared to traditional FEM methods (Rovira-Navarro et al. 2024) allows to explore a large range of interior models and their tidal response. While the idea of measuring additional tidal signals arising from lateral variations has not been considered as use case for JUICE yet. The focus of this research, is therefore, to investigate whether it is possible to constrain lateral variations in Ganymede with JUICE. This leads to the central research question:

Will JUICE measurements be precise enough to constrain lateral variations in the thickness of Ganymede's ice shell?

To answer this research question, a number of sub-question arise that need to be explored and present the outline of the thesis work:

1. What additional tidal contributions are expected for Ganymede assuming an interior with lateral variations?
2. How sensitive are the tidal signals to changes in the interior parameters?
3. Does the observational error during JUICE's GCO500 phase allow to realistically observe higher order components (degree > 2) of Ganymede's tidal response?
4. What is the expected uncertainty in observing the additional tidal signals, and if it is low enough, which response modes could be observed?

3

Covariance Analysis of JUICE to Tidal Response of Ganymede

This chapter investigates the feasibility of measuring additional tidal signals, present due to lateral variations in Ganymede's interior, using the JUICE spacecraft during its final orbital phase. A covariance analysis is conducted to obtain the expected uncertainties associated with observing the gravitational Love numbers to the observations of the orbit, which is determined via radio-tracking from Earth. To achieve this, the chapter is structured as follows: Section 3.1 introduces the general framework of the orbit determination process in which simulated observations are obtained and fitted to the dynamical model defined, leading to the covariance of estimated parameters. Section 3.2 applies this approach to the case of simulating JUICE in its GCO500 phase, detailing the specific settings and parameters chosen and how the formal uncertainties are obtained. The implementation of extended Love numbers into the Tudat software is described. This incorporates tidal effects into Ganymede's time-varying gravity field, that arise due to lateral variations and allows to study their effect on JUICE - including the newly implemented extended Love numbers. A verification of results is done in Section 3.3 after which Section 3.4 presents the results of the covariance analysis.

3.1. Orbit Determination and Covariance Methodology

This section outlines the general methodology employed in determining the orbit of a spacecraft from observations and how a covariance analysis is performed. This is later used during the numerical simulations designed to evaluate JUICE's sensitivity to Ganymede's tidal response induced by Jupiter.

In the following, the general method of batch weighted least squares estimation is explained. The estimated dynamical parameters are contained in the state $\boldsymbol{x}(t)$, with $\boldsymbol{z}$ denoting the observation vector and $\boldsymbol{h}(\boldsymbol{x_0})$ the equations relating the parameters to the observation, evaluated at state $\boldsymbol{x_0}$ at epoch t_0. The observation equation is then:

$$\boldsymbol{z} = \boldsymbol{h}(\boldsymbol{x_0}) + \boldsymbol{\epsilon} \tag{3.1}$$

where $\boldsymbol{\epsilon}$ represents the measurement errors, which are typically randomly distributed around zero mean. The squared sum of the residuals vector $\boldsymbol{\rho}$, is now minimized to obtain a least squares best fit and reconstruct the orbit from the observations. Since the equations in h are non-linear, the equations can be linearised around a known reference state $\boldsymbol{x_0^{ref}}$ leading to an estimate of the residual vector:

$$\boldsymbol{\rho} = \boldsymbol{z} - \boldsymbol{h}(\boldsymbol{x_0}) \tag{3.2}$$

$$\boldsymbol{\rho} \approx \boldsymbol{z} - \boldsymbol{h}(\boldsymbol{x}_0^{ref}) - \frac{\delta \boldsymbol{h}}{\delta \boldsymbol{x}_0}(\boldsymbol{x}_0 - \boldsymbol{x}_0^{ref}) \tag{3.3}$$

$$\boldsymbol{\rho} = \Delta \boldsymbol{z} - \boldsymbol{H}\Delta \boldsymbol{x}_0 \tag{3.4}$$

where $\boldsymbol{\Delta x_0}$ is the difference between $\boldsymbol{x_0}$ and the reference state and $\boldsymbol{\Delta z}$ is the difference between the actual observations and the computed observations from the reference orbit ($\Delta \boldsymbol{z} = \boldsymbol{z} - \boldsymbol{h}(\boldsymbol{x}_0^{ref})$. The linearised version of the observation residuals vector introduces the design matrix ($\boldsymbol{H}$), containing the partial derivatives of the modeled observations with respect to the state vector at t_0. The general solution of the least squares problem has to be solved in an iterative way to converge to a solution and can be rearranged to (Montenbruck and Gill 2000):

$$\Delta \boldsymbol{x}_0^{lsq} = (\boldsymbol{H}^T \boldsymbol{H})^{-1}(\boldsymbol{H}^T \Delta \boldsymbol{z}) \tag{3.5}$$

where $\Delta \boldsymbol{x}_0^{lsq}$ is the least-squares estimated required correction of the reference state.

Weighted least-squares can be used when different measurements types are present with different errors and units and the observations cannot be treated with equal confidence. A weight can be applied to each residual through the weight matrix ($\boldsymbol{W}$), using the square of the inverse of the total expected error of each measurement σ_i (from i to n):

$$\boldsymbol{W} = \boldsymbol{S}^2 = diag(\sigma_1^{-2}, ..., \sigma_n^{-2}) \tag{3.6}$$

$\boldsymbol{S}$ is a square diagonal matrix. The formulation in Equation 3.6 requires uncorrelated observations, thus independent at each time step. However, off-diagonal terms can be added to describe correlation between measurements at one time-step. The corresponding weighted least squares solution is given as (Montenbruck and Gill 2000):

$$\Delta \boldsymbol{x}_0^{lsq} = (\boldsymbol{H}^T \boldsymbol{W} \boldsymbol{H})^{-1}(\boldsymbol{H}^T \boldsymbol{W} \Delta \boldsymbol{z}) \tag{3.7}$$

Neglecting any systematic errors and leaving only random errors in the residuals allows to obtain the covariance matrix of the estimated parameters ($\boldsymbol{P}$) as:

$$\boldsymbol{P} = (\boldsymbol{H}^T \boldsymbol{W} \boldsymbol{H})^{-1} = \begin{pmatrix} \sigma_1^2 & \rho_{12}\sigma_1\sigma_2 & \dots & \rho_{1n}\sigma_1\sigma_n \\ \rho_{12}\sigma_2\sigma_1 & \sigma_2^2 & \dots & \rho_{2n}\sigma_2\sigma_n \\ \dots & \dots & \dots & \dots \\ \rho_{1n}\sigma_1\sigma_n & \rho_{2n}\sigma_2\sigma_n & \dots & \sigma_n^2 \end{pmatrix} \tag{3.8}$$

The diagonal terms in P contain the square of the standard deviation of each parameter in the state vector (σ_i). This can be interpreted as a measure of accuracy and thus the expected formal uncertainty of each parameter. The off-diagonal components give the co-variances of each pair of parameters through the correlation coefficient ρ_i. By way of example, σ_{12} is the co-variance of parameter 1 and 2 and the correlation coefficient is defined as: $\rho_{12} = \sigma_{12}/(\sigma_1\sigma_2)$.

The covariance matrix provides a measure to the achievable a-priori orbit determination accuracy and the sensitivity of estimated parameters with respect to the observations. The correctness of the covariance matrix in evaluating the orbit accuracy, depends on constructing a realistic measurement weighting matrix **W**. Since **P** only uses the observation partials in **H** and the weighting matrix **W**, it does not contain any systematic measurements errors, which can only be found after the measurements are actually obtained (Montenbruck and Gill 2000).

In the context of the JUICE mission, a so called multi-arc least-squares determination is typically used for orbit determination (Cappuccio et al. 2020; De Marchi et al. 2022; Notaro et al. 2019). This splits the total trajectory during the GCO500 phase into several arcs, where each arc is handled independently. The parameters estimated are split into global parameters that are common to the entire dataset (eg. coefficients of the gravity field) and local parameters that are estimated on an arc-wise basis (eg. JUICE's

initial position and velocity). The arcs are non-overlapping and at the beginning of each arc the initial conditions are defined.

The state vector, evaluated at the reference state for a covariance analysis ($\mathbf{x_0}$), includes thus a set of global and local parameters (g and l):

$$\boldsymbol{x} = [g; l] \tag{3.9}$$

The observations are split into arcs 1 to n and arranged in the observation vector:

$$\boldsymbol{z} = [z_1, \ \dots, z_n] \tag{3.10}$$

The reason for this approach is that the force models used in the dynamical models are uncertain and errors in the propagation of JUICE build up over time. Furthermore, the spacecraft performs a number of maneuvers during its GCO500 phase to keep a predefined orbit geometry. By resetting the spacecraft after each arc to the predefined (expected) trajectory from the ESA SPICE files, uncertainties in the dynamics do not accumulate and the maneuvers altering the orbit are indirectly included in the updated initial state.

In a multi-arc estimation, the design matrix separates between global parameters ($\mathbf{g}$) and local parameters ($\mathbf{l}$) and the results of all arcs are combined together (De Marchi et al. 2022):

$$\begin{pmatrix} \Delta\mathbf{z}_1 \\ \Delta\mathbf{z}_2 \\ \vdots \\ \Delta\mathbf{z}_n \end{pmatrix} = \begin{bmatrix} \mathbf{H_{l1}} & 0 & \cdots & 0 & \mathbf{H_{g1}} \\ 0 & \mathbf{H_{l2}} & \cdots & 0 & \mathbf{H_{g2}} \\ \vdots & \vdots & \ddots & \vdots & \vdots \\ 0 & 0 & \cdots & \mathbf{H_{ln}} & \mathbf{H_{gn}} \end{bmatrix} \begin{pmatrix} \Delta\mathbf{l}_1 \\ \Delta\mathbf{l}_2 \\ \vdots \\ \Delta\mathbf{g} \end{pmatrix} \tag{3.11}$$

where n are the number of arcs, which are 100 arcs for the GCO500 of 100 days. The design matrix of a multi-arc approach is composed into the partial derivatives of each observation with respect to their corresponding local and global parameters. The observations of arc 1 (z_1) are then only linked to local parameters of that corresponding arc (l_1) and not to the remaining local parameters (Parisi, M. et al. 2012):

$$\boldsymbol{H} = \begin{bmatrix} \partial z_1/\partial l_1 & 0 & \dots & 0 & \partial z_1/\partial g \\ 0 & \partial z_2/\partial l_2 & \dots & 0 & \partial z_2/\partial g \\ \dots & \dots & \dots & \dots & \dots \\ 0 & 0 & 0 & \partial z_n/\partial l_n & \partial z_n/\partial g \end{bmatrix} \tag{3.12}$$

When a-priori information is available on the system, the weighted least squares solution is written as (De Marchi et al. 2022):

$$\Delta\mathbf{x_{est}} = (\mathbf{H^T W H} + \mathbf{W_{AP}})^{-1}(\mathbf{H^T W}\Delta\mathbf{z} + \mathbf{W_{AP}}\Delta\mathbf{x_{AP}}) \tag{3.13}$$

Compared to equation 3.7, $\Delta\mathbf{x}_{est}$ is the differential correction of the state vector, $\mathbf{W_{AP}}$ and $\mathbf{x_{AP}}$ are a-priori values of the weight matrix and state vector and the covariance matrix is now defined by:

$$\mathbf{P} = (\mathbf{H^T W H} + \mathbf{W_{AP}})^{-1} \tag{3.14}$$

The formal uncertainties of the estimated parameters can be obtained by taking the square root of the diagonal entries of the covariance matrix (P):

$$\sigma_i = \sqrt{P_{ii}} \tag{3.15}$$

3.2. Simulation of JUICE during GCO500

This section details how the general appraoch described in Section 3.1 is applied to simulate the JUICE mission around Ganymede. The dynamical model used to propagate JUICE during GCO500, includes most importantly the gravity field of Ganymede and time dependent effects from the tides raised by Jupiter. The time-varying gravity field model is explained in Subsection 3.2.1, which includes the representation of Ganymede's gravity field in terms of spherical harmonics, the inclusion of tidal effects, the implementation of mode coupled Love numbers into the simulation, the rotation model and the removal of the permanent tide effect. Subsection 3.2.2 presents the remaining aspects and parameters chosen in the dynamical model and specific settings used in the covariance analysis of JUICE. The generation of the synthetic 3GM observations is detailed in Subsection 3.2.3.

3.2.1. Time-varying Gravity Field of Ganymede

To conduct the covariance analysis and simulate the JUICE mission around Ganymede, the Technical University of Delft Astrodynamics Toolbox (Tudat)[1] is used. Tudat is a well-established software written in C++ for astrodynamics research, providing tools for simulating observations, propagating spacecraft trajectories and performing estimation problems. The core functionality is implemented in C++ allowing fast computation and the python interface Tudatpy is used to interact with the software. Tudat already includes functionality for modeling the effects of solid-body tides within dynamical models, providing a strong foundation for extending the tidal models to include the effect of bodies with lateral variations and corresponding extended Love numbers.

Effect of tides on gravity field

The gravity field of a body can be defined within the Tudat environment, which typically represents it using a spherical harmonics series expansion. Specifically, the external gravity field of Ganymede is described by the spherical harmonic expansion of the gravitational potential up to degree N. The gravitational potential at a point (r, θ, φ) is expressed as a sum of spherical harmonics, parameterized by the normalized gravitational coefficients $\bar{C}_{nm}$ and $\bar{S}_{nm}$ (Petit and Luzum 2010):

$$U(r,\theta,\varphi) = \frac{GM}{r}\sum_{n=0}^{N}\left(\frac{R}{r}\right)^{n}\sum_{m=0}^{n}[\bar{C}_{nm}\cos(m\varphi) + \bar{S}_{lm}\sin(m\varphi)]\bar{P}_{nm}(\cos\theta) \tag{3.16}$$

here R is the radius, r is the position vector measured from the body's center of mass and θ and φ are the body-fixed colatitude and longitude. $\bar{P}_{nm}$ are the normalized associated Legendre functions as discussed in Section 4.2. Similar to the Legendre functions, the normalized gravitational coefficients $\bar{C}_{nm}$ and $\bar{S}_{nm}$ can be related to the unnormalized coefficients by:

$$C_{nm} = N_{nm}\bar{C}_{nm} \quad and \quad S_{nm} = N_{nm}\bar{S}_{nm} \tag{3.17}$$

$$N_{nm} = \sqrt{\frac{(2n+1)(n-m)!(2-\delta_{0m})}{(n+m)!}} \quad \delta_{0m} = 1 \text{ if } m = 0, \delta_{0m} = 0 \text{ if } m \neq 0 \tag{3.18}$$

The leading term (n = 0) of Equation 3.16 corresponds to $\frac{GM}{r}$, which is the effect of treating the body as a point mass. The amplitude of gravitational coefficients at each degree, determines the contribution of each $\cos m\varphi$ and $\sin m\varphi$ component, where the $\bar{C}_{nm}$ coefficients correspond to cosine terms and $\bar{S}_{nm}$ to sine terms.

The potential field of Equation 3.16 represents the static gravity field. Any time varying effects of the gravity field such as secular variations, ocean or solid body tides can be taken into account as correction to the gravity field coefficients. The gravitational potential of Ganymede is perturbed by the tides raised by Jupiter and this effect is related to the forcing potential with gravitational Love numbers. As a result,

[1] Tudat Space, TU Delft: https://docs.tudat.space/en/latest/index.html, Last accessed on 23.12.2024

the time-varying part of the gravitational coefficients $\Delta\bar{C}_{nm}$,$\Delta\bar{S}_{nm}$ are related to the gravitational Love numbers. In Tudat, the effect of solid body tides on the gravity field of a body is implemented in the form of Equation 3.19(Petit and Luzum 2010):

$$\Delta\bar{C}_{nm} - i\Delta\bar{S}_{nm} = \frac{k_{nm}}{2n+1}\frac{GM_j}{GM}\left(\frac{R}{r}\right)^{n+1}\bar{P}_{nm}\cos(\theta)e^{-im\varphi} \tag{3.19}$$

with M and M_j being the mass of the tide-raising and deforming body respectively. The implementation in Tudat is done in terms of real spherical harmonics transforming this to:

$$\Delta\bar{C}_{nm} = \frac{k_{nm}}{2n+1}\frac{GM_j}{GM}\left(\frac{R}{r}\right)^{n+1}\bar{P}_{nm}\cos(\theta)[\cos(m\varphi)] \tag{3.20a}$$

$$\Delta\bar{S}_{nm} = \frac{k_{nm}}{2n+1}\frac{GM_j}{GM}\left(\frac{R}{r}\right)^{n+1}\bar{P}_{nm}\cos(\theta)[\sin(m\varphi)] \tag{3.20b}$$

Equation 3.20 models the effect of tides as changes in the normalized gravitational coefficients $\Delta\bar{C}_{nm}$ and $\Delta\bar{S}_{nm}$ at a specific degree n and order m, due to tidal forcing at the same degree and order, described by the Love numbers k_{nm}. Each forcing contribution (degree and order) corresponds to a single set of coefficients $\Delta\bar{C}_{nm}$ and $\Delta\bar{S}_{nm}$ at the same n, m. In the current Tudat functionality, equation 3.20 can be evaluated using either:

1. A single, traditional Love number $k_n = k_{nm}$ per forcing degree, such as k_2 or k_3, or
2. A set of Love numbers varying by order for each degree of forcing wavelength, e.g., k_{20}, k_{21}, k_{22}.

The first option corresponds to a spherically symmetric body where $k_{20} = k_{21} = k_{22}$ and the Love numbers are order independent. Option 2 is able to distinguish between different degree 2 forcings. This functionality enables the inclusion of several tidal forcings into the gravity field of a body but does not support modeling lateral variations, which require the use of extended Love numbers. The following two main functions are thus available:

Table 3.1: Available functions to add gravity field variations to a body in Tudat.

Function	Love numbers	Explanation
Solid Body Tide	k_2, k_3...	Equation 3.20 is evaluated with a single Love number for each forcing degree
Solid Body Tide for variable degree and orders	$[k_{20}, k_{21}, k_{22}], [k_{30}...]$	Equation 3.20 is evaluated with a set of real Love numbers at any forcing degree and order.

Implementation of extended Love numbers in Tudat

To extend the gravity field variations and make them include lateral variations, the introduction of extended Love numbers is necessary. These are derived in Subsection 4.2.2 and include tidal responses at any additional degree and order other to the forcing. Equations 3.21a and 3.21b are a more general version of Equation 3.20 in which extended Love numbers are used and related to the time varying components of the $\bar{C}_{nm}$ and $\bar{S}_{nm}$ coefficients.

$$\Delta\bar{C}_{nm} = \sum_{n_\alpha, m_\alpha} \frac{1}{2n+1}\frac{GM_j}{GM}\left(\frac{R}{r}\right)^{n+1}\bar{P}_{nm}(\cos\theta)[k^{nm}_{n_\alpha m_\alpha}\cos(m\varphi) + k^{nm}_{n_\alpha -m_\alpha}\sin(m\varphi)] \tag{3.21a}$$

$$\Delta\bar{S}_{nm} = \sum_{n_\alpha, m_\alpha} \frac{1}{2n+1}\frac{GM_j}{GM}\left(\frac{R}{r}\right)^{n+1}\bar{P}_{nm}(\cos\theta)[k^{n-m}_{n_\alpha m_\alpha}\cos(m\varphi) + k^{n-m}_{n_\alpha -m_\alpha}\sin(m\varphi)] \tag{3.21b}$$

For the spherically symmetric case the Love numbers reduce to $k^{nm}_{n_\alpha m_\alpha} = k_n$. Compared to the Equation 3.20, this expression, describes the change in the gravity field coefficient $\bar{C}_{nm}$ at a specific response (degree n and order m) as a sum of forcing contributions (n_α, m_α). With lateral variations, a response signal can contain contributions also from other forcing wavelengths. This was demonstrated in Section 4.4, where a (2,2) response was induced by both forcing contributions (2,0) and (2,2). Furthermore, positive forcing orders ($+m_\alpha$) correspond to the cosine forcing, while negative orders ($-m_\alpha$) are linked to the sine terms. The sine coefficient $\bar{S}_{nm}$ contains contributions from Love numbers with negative order (-m) responses while the cosine response is linked to positive order responses (+m).

As the extended Love numbers are mode-coupled, equations 3.21a and 3.21b are evaluated for all response modes where Love numbers are defined. For example, degree 3 gravity field coefficients now vary due to a degree 2 forcing. This approach properly accounts for the effects of lateral variations in the dynamics.

It is important to note that the Love numbers implemented here are real and not complex Love numbers, mainly due to time constraints of the thesis project. Real and complex Love numbers have the same order of magnitude, their difference being typically a factor of $\sqrt{2}$. The conversion from complex to real Love numbers is given in Equation 4.19a. Tudat itself uses real spherical harmonics in its implementation and can not deal with negative order Love numbers ($k^{nm}_{n_\alpha,m_\alpha}$) can be defined and this neglects the effects of a sine forcing on the response given by Love numbers $k^{nm}_{n_\alpha - m_\alpha}$ and $k^{n-m}_{n_\alpha - m_\alpha}$.

Obtaining the covariance matrix requires evaluating the partials of the observations (z) to the parameters. The primary interest is on obtaining the covariance to the mode coupled Love numbers, for which the following partial is evaluated in Tudat:

$$\frac{\partial z}{\partial k^{nm}_{n_\alpha m_\alpha}} = \frac{\partial z}{\partial \Delta C_{nm}} \frac{\partial \Delta C_{nm}}{\partial k^{nm}_{n_\alpha m_\alpha}} \tag{3.22}$$

z is the observation, for example from a Doppler measurement. The partial of the observation with respect to the Love number is split with the chain rule in calculating the partial of the observation to the gravity field coefficient at response degree n and order m, and in a second partial of the gravity field coefficient to the Love number. The second partial is different to the earlier tidal models as it now includes the mode coupled Love numbers instead of the previous simpler Love numbers. It is important to note that ΔC_{nm} is evaluated at the response wavelength corresponding to the superscript of $k^{nm}_{n_\alpha m_\alpha}$ and not at the forcing wavelength. The partial derivative of ΔC_{nm} to the Love number is then:

$$\frac{\partial \Delta C_{nm}}{\partial k^{nm}_{n_\alpha m_\alpha}} = \frac{1}{2n+1} \frac{GM_j}{GM} \left(\frac{R}{r}\right)^{n+1} \bar{P}_{nm}(\cos\theta) \cos(m\varphi) \tag{3.23}$$

Rotation Model of Ganymede

In this research, the focus is set on the effect of the eccentricity tides on Ganymede as the obliquity tides are much smaller and the former effect is dominant. Although the moon is tidally locked to Jupiter and thus in synchronous rotation, its longitude with respect to Jupiter in a body-fixed frame (φ) is not zero. Due to the slightly eccentric orbit, this angle varies over the orbit. A schematic of how a tidally locked Ganymede rotates around Jupiter is provided in Figure 3.1. In this representation the longitude is ψ, the true anomaly f and the rotation of the moon is θ.

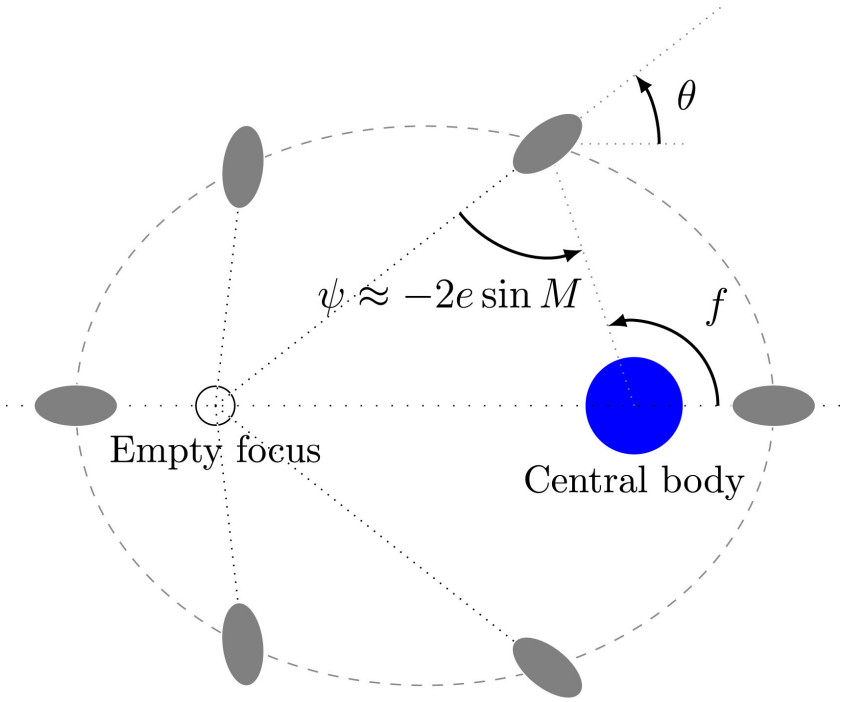

Figure 3.1: Schematic representation of the non-librating rotation of a tidally locked satellite on an eccentric planar orbit. Image Credit: (Dirkx et al. 2016)

A rotation model for Ganymede is chosen that fixes the equator of Ganymede to its orbital plane, so that the latitude is always zero. The longitude can be computed from the orbital state as:

$$\varphi = 2esinM - \gamma \approx e2sinE \tag{3.24}$$

where γ is the tide induced libration, a change in the rotation over the period of the orbit (Van Hoolst et al. 2013). The libration is neglected here and for low eccentricities the mean and eccentric anomaly are similar. This results in the expression ($2esin(E)$) to model the longitude variation with eccentricity (e) and eccentric anomaly (E). In this way the x-axis of Ganymede body centered frame always points to the empty focus point of the orbit as seen in Figure 3.1.

Figure 3.2 shows the radius, co-latitude and longitude of Ganymede's body fixed frame with respect to Jupiter over 100 days during the GCO500 phase. The initial states and ephemerides of Ganymede, Jupiter and other planetary bodies as well as the JUICE trajectory are obtained from ESA Spacecraft, Planet, Instrument, Camera-matrix, Events (SPICE) data files (kernel files), which can be accessed using SPICE. These files are mission-specific and created by spacecraft operation center responsible for the JUICE mission [2]. The planetary ephemerides and JUICE trajectory files used are juice_crema_5_0 and NOE_5 [3].

[2]NASA SPICE toolkit. Available at: https://naif.jpl.nasa.gov/naif/aboutspice.html, Accessed 23.12.2024
[3]ESA SPICE Data. Available at: http://spiftp.esac.esa.int/data/SPICE/JUICE/kernels/, Accessed 12.09.2024

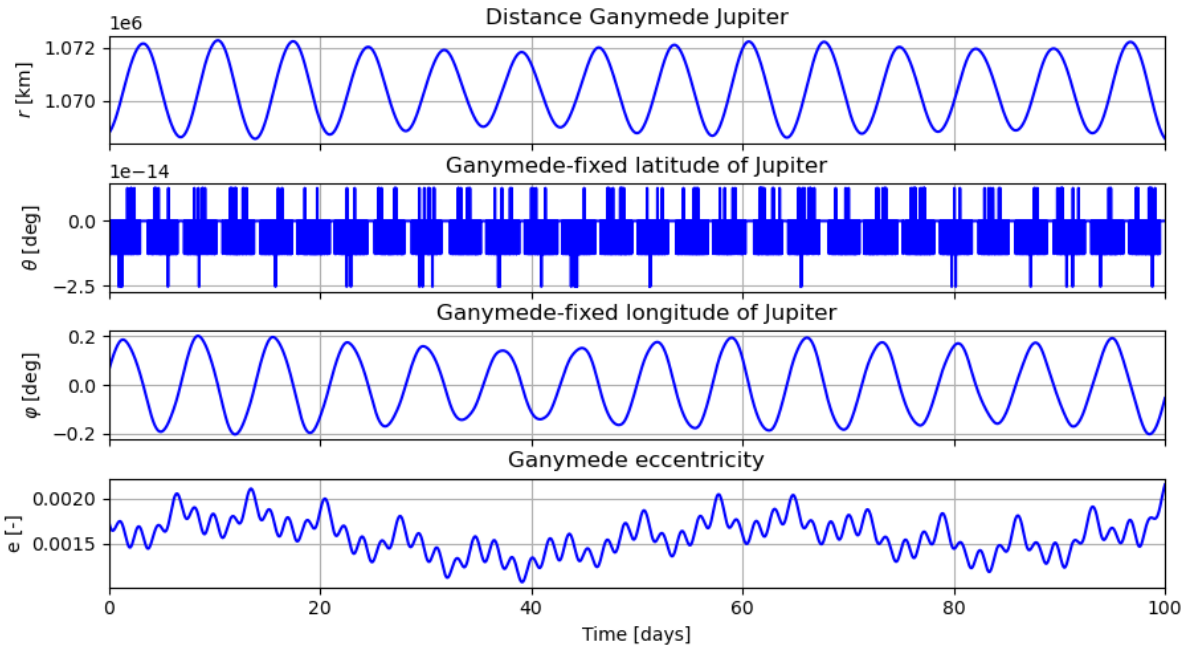

Figure 3.2: Spherical coordinates of Ganymede body-fixed frame with respect to Jupiter during GCO500 phase (100 days). Radius, colatitude, longitude and eccentricity of Ganymede are shown.

Figure 3.2 shows how the orbital distance of Ganymede oscillates around roughly 1 million kilometers. The latitude (θ) is essentially fixed to zero and the fluctuations around 1×10^{-14} are numerical noise. The longitude oscillates between ±0.2 degrees. With this rotation model, eccentricity tides caused by the variation in orbital distance are modeled and the effects of Ganymede librating with respect to Jupiter seen in the longitude variation, due to the velocity change along the orbit. Obliquity tides are not accounted for since the latitude is set to zero. The eccentricity ranges from 0.001 to 0.0021, which agrees with the expected mean value of 0.0015 during GCO500 (Van Hoolst et al. 2024).

Removal of permanent tide

During the covariance analysis, the effect of lateral variations on Ganymede's tides is included with the mode coupled Love numbers introduced before. The change in gravity field coefficients is evaluated in Tudat with equations 3.21a and 3.21b, using the spherical coordinates as input. The resulting tidal forcing is a function over time that is not necessarily zero-centered and thus includes the effect of the static time-invariant permanent tide.

Figure 3.3 shows the resulting tidal force at degree 2 computed from the right hand side (RHS) of equations 3.21a and 3.21b over 100 days. The mean value for some of the contributions is considerably larger than the actual variation of the time-varying tidal effect. By way of example, the tidal forcing $\Delta\bar{C}_{20}$ has an average value of -4.26×10^{-5}, however its oscillations only have an amplitude of 1×10^{-7}. The permanent tide masks the time-varying signal and should thus be removed, otherwise there might be a misrepresentation of the effect of the gravitational Love numbers on the orbit of JUICE during the covariance analysis.

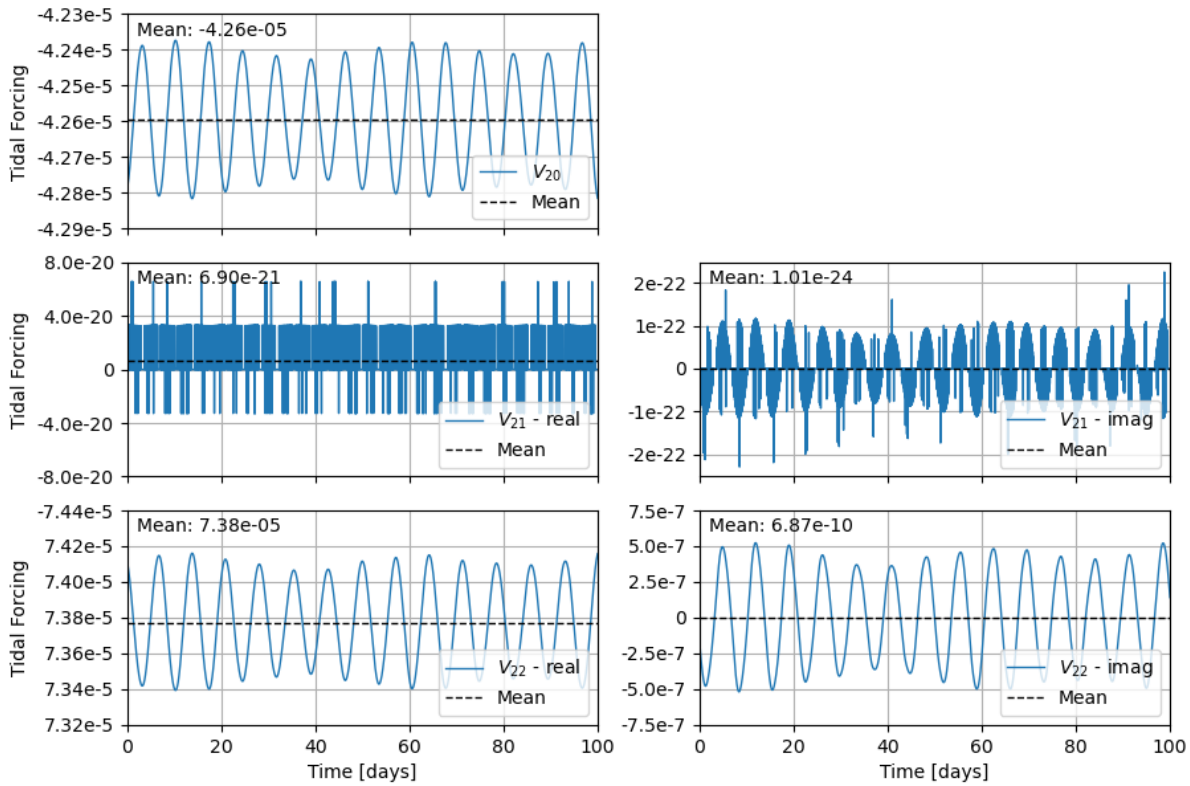

Figure 3.3: Tidal forcing at Ganymede at degree 2, computed from the RHS of equation 3.19. Real and imaginary parts of the forcing are computed over a period of 100 days during GCO500 and contain the permanent tide. The mean value of each contribution is computed as average and shown next to each signal.

Table 3.2: Tidal Forcing Components and mean values during GCO500

Tidal Forcing Component	Mean Value during GCO500
V_{20}	$-4.259344 \cdot 10^{-5}$
V_{21}	$6.903085 \cdot 10^{-21}$
V_{2-1}	$1.009588 \cdot 10^{-24}$
V_{22}	$7.377329 \cdot 10^{-5}$
V_{2-2}	$6.868871 \cdot 10^{-10}$
V_{30}	$1.242177 \cdot 10^{-23}$
V_{31}	$1.083726 \cdot 10^{-7}$
V_{3-1}	$5.053437 \cdot 10^{-13}$
V_{32}	$-1.603624 \cdot 10^{-23}$
V_{3-2}	$-4.688657 \cdot 10^{-27}$
V_{33}	$-1.399058 \cdot 10^{-7}$
V_{3-3}	$-1.957201 \cdot 10^{-12}$

The effect of the permanent tide has been removed from the tidal forcing in Tudat by computing the mean value of each tidal forcing contribution and removing them manually in the code. This was implemented as a temporary solution to not postpone the timeline of the thesis. The average value of

each coefficient of the tidal forcing for both degree 2 and 3 has been computed and is shown in Table 3.2. Since the number of orbits is not integer, the mean value is typically taken over an integer number of tidal cycles to get the best estimate of the permanent tide. Looking at Figure 3.3, there are around 14 complete tidal periods during the time span of 100 days which gives an accurate enough mean value. The mean values shown in Table 3.2 are subtracted from the coefficients at each degree and order of the forcing.

The tidal forcing of Ganymede during GCO500 for degree 2 and 3 with the permanent tide removed is shown in Figures 3.4 and 3.5. The magnitude of the tidal forcing is around 1×10^{-7} for degree 2 and 1×10^{-9} to 1×10^{-10} for degree 3. This is expected as the magnitude of the tidal effect decreases for higher order terms and is described by the ratio $(\frac{R}{r})^{n+1}$. With a radius of 2631.2 km and orbital radius of around 1×10^6 km the ratio of the magnitude of the degree 2 and 3 forcing is roughly: $(\frac{2631.2}{2631.2+1000000}) \approx 384$, which aligns with the two orders of magnitude observed in the figure.

Due to the assumption of the latitude being fixed to zero, a number of forcing contributions are not present. Specifically the tidal forcing contributions for degree and order (2,1), (3,0) and (3,2) are zero. This means that during the covariance analysis the dynamical model does not include these effects. The magnitude of these signals visible is due to numerical noise.

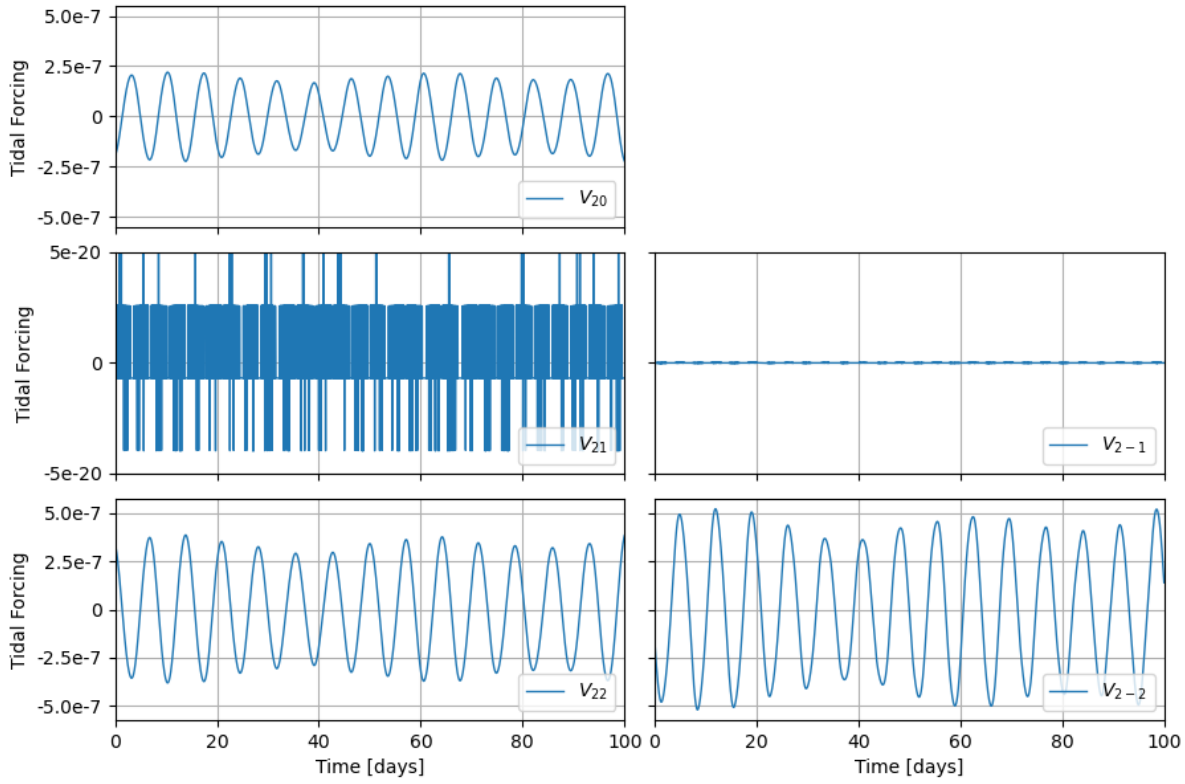

Figure 3.4: Tidal forcing of Ganymede at degree 2 computed from the RHS of equation 3.19 with the permanent tide removed during GCO500.

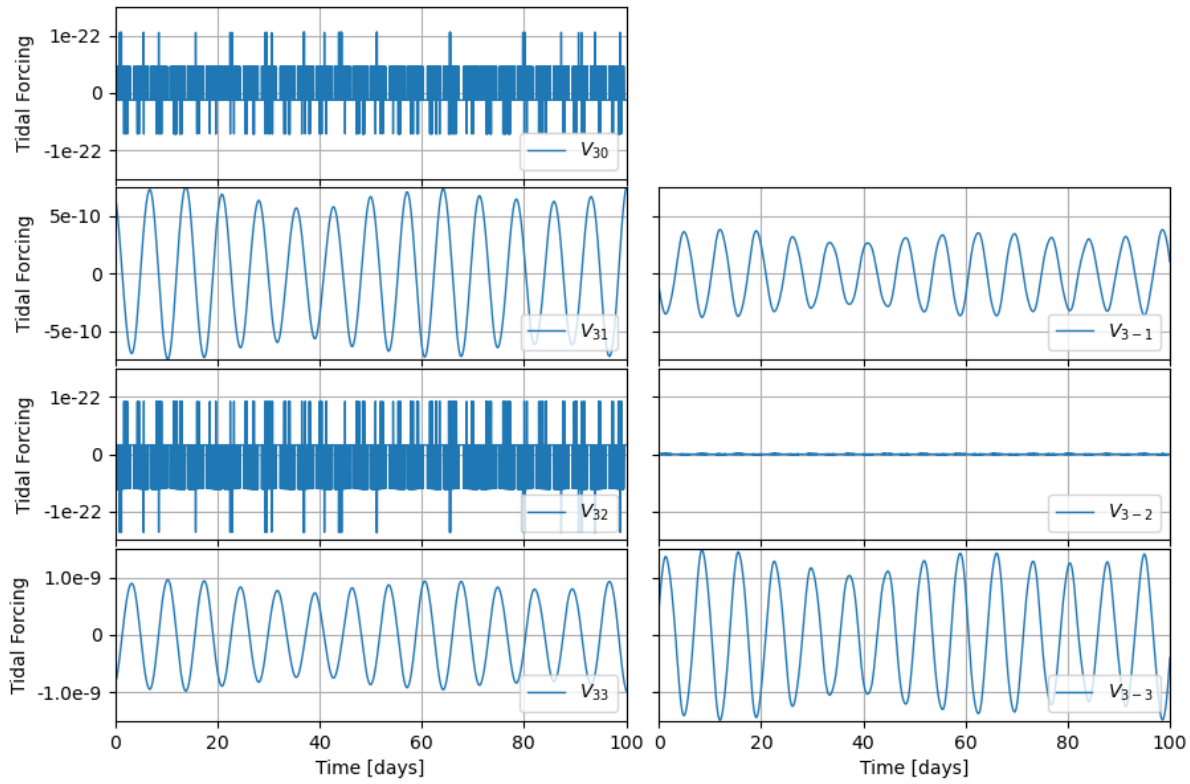

Figure 3.5: Tidal forcing of Ganymede at degree 3 computed from the RHS of equation 3.19 with the permanent tide removed during GCO500.

3.2.2. Dynamical Model and GCO500 Simulation Setup

A key focus of these simulations is the inclusion of mode-coupled Love numbers in the tidal model of Ganymede, the implementation of these was described in Section 3.2.1. Specifically, this Subsection discusses the force models included in the dynamical model, the choice of parameters estimated during the simulations and the general settings for the covariance analysis.

The dynamical model includes the gravity field of Ganymede up to degree and order 15. The gravity field is truncated at this point since beyond degree 15 there is no significant effect on the estimated uncertainties observed.

Two of the coefficients have been estimated using Galileo observations, which are $C_{20} = -127.8 \times 10^{-6}$ and $C_{22} = 38.3 \times 10^{-6}$. Higher order gravity field coefficients are unknown but their magnitude can be estimated using a power rule approximation (Kaula, W. M. 1966). Equation 3.25 provides the estimated amplitude of the gravity field spectra, which is a good approximation such as for Titan (Durante et al. 2019).

$$\bar{C_n}^2 = A_k \frac{10^{-10}}{n^4} \tag{3.25}$$

A_k is Kaula's coefficient, which will be adopted as 1. The tidal response of Ganymede to a forcing by Jupiter is included by specifying the corresponding gravitational Love numbers (single degree, mode coupled etc) see Section 3.2.1.

The gravity field of Jupiter is included up to degree and order 4. The perturbations of the Sun, Io, Callisto, Europa and Saturn are included as point mass accelerations. Solar radiation pressure (SRP) forces are modeled using a cannonball radiation model, assuming a surface area of JUICE of $A_{SRP} = 100m^2$ and radiation pressure coefficient of $C_R = 1.2$.

Lastly, drag on the JUICE spacecraft is caused by the exosphere present on Ganymede. (Plainaki et al. 2015) simulate the exosphere arising from sublimation of water ice on the surface, ionizing radiation and ion stuttering causing particles to be released. They provide analytical expressions for the density and scale height of the exosphere which can be used to set up a simple exponential atmosphere model. The scale height and surface density used are $H_s = 43.3km$ and $\rho_{atm} = 7.5 \times 10^{-12}$ (Plainaki et al. 2015) A drag coefficient of $C_D = 1.2$ and reference area of $A_D = 100m^2$ are selected.

Figure 3.6 shows the acceleration norm in (m/s^2) of all accelerations included in the dynamical model over the first 20 days during GCO500. As expected, the dominating effects are Ganymede and Jupiter, which justifies using a higher order gravity field. The effects of Io, SRP, Europa, Callisto and the Sun are between 1×10^{-7} to 1×10^{-9}, which is on the same order of magnitude as the amplitude of degree 2 and 3 tidal forcing signals observed in figures 3.4 and 3.5. The drag force and Saturn point mass contributions are 1×10^{-11} and 1×10^{-13} respectively. This is much lower than the tidal forcing, however since these accelerations can add up over a single arc of 1 day it was decided to include them in the model.

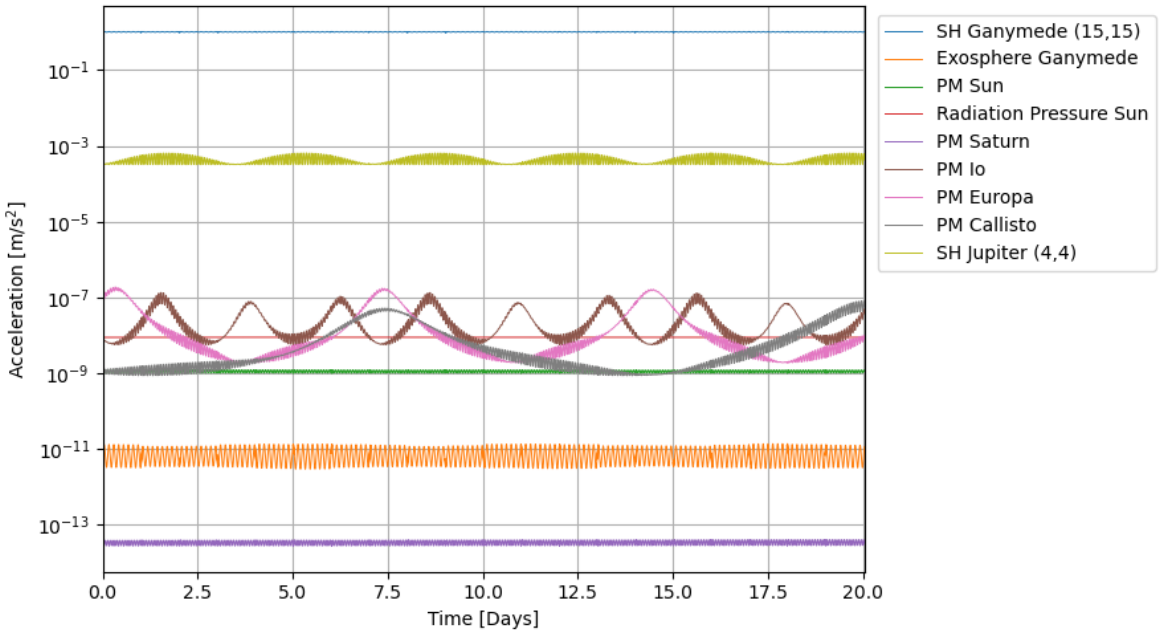

Figure 3.6: Acceleration norm of all perturbations included in the dynamical model during the first 20 days of GCO500. Point mass effects (PM) and spherical harmonic approximations (SH) shown.

The initial arc-wise state of JUICE and ephemerides of planets and moons are taken from the ESA SPICE files, discussed in Section 3.2.1. For the GCO500 phase the start date is 21st of May 2035 at 15h. JUICE is given a mass of 2500 kg, which is the rounded up dry mass value assuming there is some fuel left for maneuvers [4]. The general overview of all parameters and settings used for the covariance analysis can be found in Table 3.3.

[4]JUICE mass: https://www.esa.int/Science_Exploration/Space_Science/Juice/Juice_spacecraft_specs Accessed 26.12.2024

Table 3.3: Models and parameters used for the covariance analysis

Model/Parameter	Description
Estimation technique	Multi-arc batch least-squares estimation with a-priori information
Mission phase and time	GCO500 100 days and arc length of 1 day
GCO500 start time	21.05.2035 15:00h
Initial state and planetary ephemerides	ESA SPICE kernels (JUICE_CREMA_5 and NOE_5 files)[5]
Reference Frame and rotation model	J2000 frame, synchronous rotation model with fixed latitude to zero.
JUICE mass	2500 kg
Ganymede gravity	Spherical harmonic gravity truncated at (15,15)
	$C_{20} = -127.8 \times 10^{-6}$, $C_{22} = 38.3 \times 10^{-6}$ (Schubert et al. 2004)
Third body perturbations	Sun, Saturn, Io, Callisto, Europa, Jupiter SH gravity truncated at (4,4)
SRP	Cannonball model with $C_R = 1.2$ and $A_{SRP} = 100\,\mathrm{m}^2$
Drag	Exponential atmosphere with $H_s = 43.3\,\mathrm{km}$, $\rho_{atm} = 7.5 \times 10^{-12}$,
	$C_D = 1.2$, and $A_D = 100\,\mathrm{m}^2$ (Plainaki et al. 2015)
Tides	Tidal effect on Ganymede due to forcing by Jupiter
	included by defining mode-coupled Love numbers $k^{nm}_{n_\alpha,m_\alpha}$
	and evaluating ΔC_{nm}, ΔS_{nm} of equations 3.21a, 3.21b
Observations	Range data at 20 cm and 300 s integration time
	Doppler data at 0.012 mm/s and 60 s integration time
Ground station	DSA 3, based in Malargue, Argentina
Observables generation	Minimum elevation angle of 15 °, occultation of Ganymede, Jupiter,
	Io, Callisto and Europa, Sun avoidance angle (5 °)
	1st order relativistic light time correction
Estimated parameters	**A-priori uncertainty**
JUICE arc-wise position (local)	5 km
JUICE arc-wise velocity (local)	0.5 m/s
Ganymede GM (global)	$0.03 \times 10^9\,\mathrm{km}^3/\mathrm{s}^2$(Schubert et al. 2004)
Ganymede gravity coefficients from degree and	Uncertainty from Kaula's rule $A_k = 1$
order (2,0) up to (15,15) (global)	
C_{20}, C_{22}	2.9×10^{-6}, 0.87×10^{-6}
Love numbers (global)	unconstrained
Constant arc-wise empirical accelerations	$1 \times 10^{-8}\,\mathrm{m/s}$
in radial, tangential, normal direction (local)	

The list of estimated parameters includes the arc-wise initial state (position and velocity) of JUICE and the gravitational parameter (GM) of Ganymede. The spherical harmonic coefficients of Ganymede's gravity field up to degree and order 15 are estimated and the gravitational Love numbers (either single degree or mode coupled). Empirical accelerations acting on JUICE in radial, tangential and normal direction are estimated each arc to account for errors in the non-gravitational forces, for example solar and Jupiter radiation pressures or thermal emission by JUICE. Since these are constant per arc, they should not absorb the time-varying tidal effects. The choice to model these on an arc-wise basis and not globally was made as possible model inaccuracies would not be constant over the whole 100 day period and an arc-wise constant offset was seen as more realistic.

This leaves the initial state and empirical accelerations as local estimated parameters while the rest is global. To define the time varying gravity field in Tudat, a central value for the Love numbers must be

chosen. Since the covariance analysis is evaluated around a certain reference state there is not much dependence on the actual values used but and the estimated Love numbers depend much more on the orbit geometry, observations and their noise.

Assuming that a single degree 2 Love number k_2 is estimated, the estimated solution vector contains a total of 1154 parameters. This includes the 600 arc-wise states of JUICE, Ganymede's gravitational parameter, all cosine spherical harmonic coefficients from (2, 0) to (15, 15), the sine spherical harmonic coefficients, the 300 arc-wise empirical acceleration coefficients of JUICE and the tidal Love number at degree 2. A-priori values can be provided to the estimated parameters, providing known uncertainty where available. The uncertainty of the C_{20} and C_{22} gravity coefficients are known from Galileo observations as 2.9×10^{-6} and 0.87×10^{-6} respectively. Similarly, the uncertainty of GM was estimated as 0.03×10^{9} km^{3}s^{-2} (Schubert et al. 2004). The remaining gravity field uses Kaula's constraint as a-priori value with coefficient ($A_k = 1$). The position and velocity of JUICE are given a-priori values of 5 km and 0.5 m/s, while the empirical accelerations are set to 10 nm/s

3.2.3. Simulated 3GM Observations

The Doppler and range observations that will be obtained by the 3GM instrument are obtained via two-way Ka-band radio link with 34.5 GHz uplink and 32.2 GHz GHz downlink to the ground station on Earth. These observations are simulated by propagating the trajectory of JUICE and a constant noise per observable type is added in the weight matrix. The Doppler measurements have been simulated with a noise of 0.012 mm/s at 60 s integration time and the range measurements with 20 cm at 300 s of integration time . To track JUICE, ESA's Deep Space Antenna 3 (DSA 3) based in Malargue, Argentina is used and currently the only station capable of establishing a three-frequency radio link (X/X, X/Ka, Ka/Ka) (Cappuccio et al. 2020; De Marchi et al. 2022). For the generation of observables, a minimum spacecraft elevation angle of 15 ° is used to filter out low-elevation data affected by tropospheric signal delays. Furthermore, the occultation of Ganymede, Jupiter, Io, Callisto and Europa is accounted. A sun avoidance angle of larger than 5 ° is specified and first order relativistic light-time corrections are applied.

3.3. Verification

This section focuses on verification of the correctness and consistency of the covariance analysis results specifically regarding the newly implemented mode-coupled Love numbers within Tudat. In subsection 3.3.1, the orbit, ground track and viable observations per day are verified. In the process of obtaining the final covariance, the design matrix is constructed in Tudat. The partials of the JUICE observations with respect to the Love numbers are verified in Subsection 3.3.2. The magnitude of results obtained is compared to the existing implemented functions for non mode coupled Love numbers in Subsection 3.3.3, while Subsection 3.3.4 compares the obtained gravity field uncertainties to literature.

3.3.1. Orbit and Observations

As a rough visual verification of the GCO500 trajectory and sanity check, the trajectory and ground track of JUICE are shown. Figure 3.7 shows the trajectory of JUICE over time, it is in a retrograde orbit (inclination > 90 °) close to sun-synchronous and precesses over time. Only every 10th arc is shown for clarity. The ground track during the first arc (24h) is shown in Figure 3.8. The high inclination orbit provides good spatial coverage over Ganymede, which is important for its geophysical observations of the gravitational field and hence measuring the tidal response.

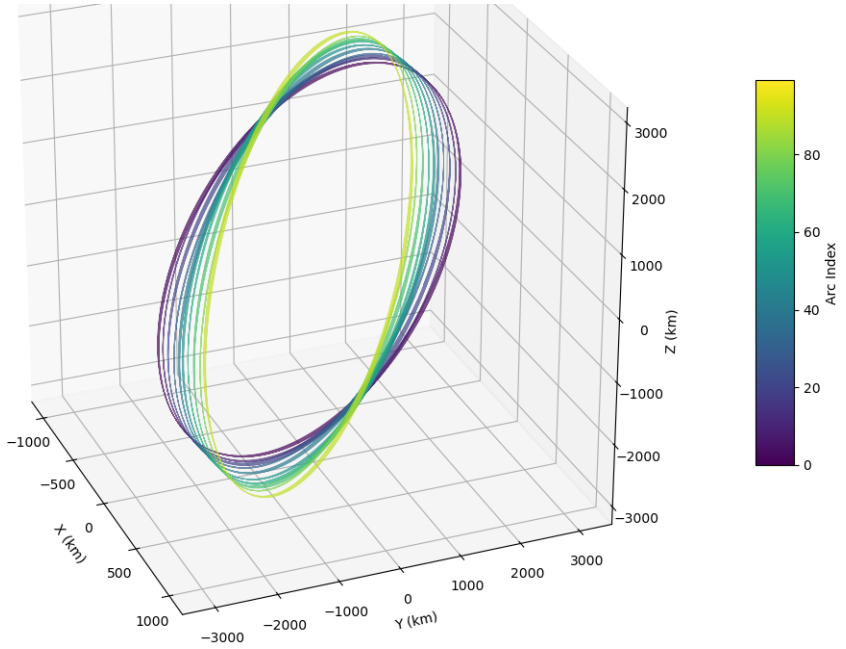

Figure 3.7: Trajectory of JUICE during GCO500 phase, showing every 10th arc for clarity.

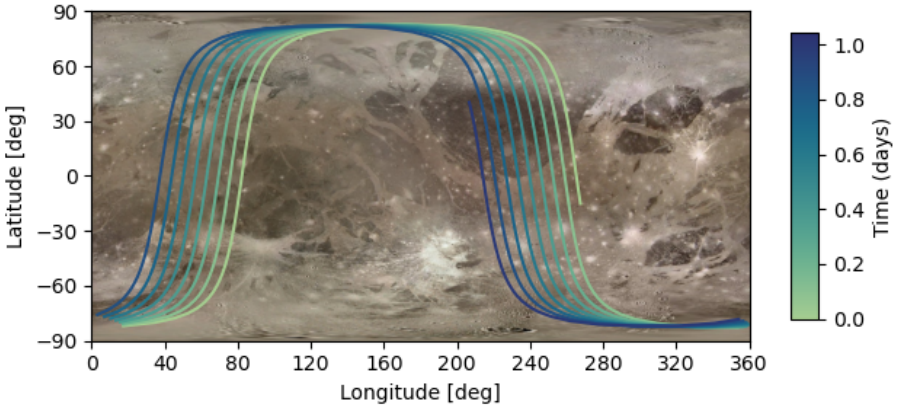

Figure 3.8: Ground track of JUICE during the first 24h of its GCO500 phase.

The correctness of the simulated observations must be verified, as they directly influence the quality of the results. Table 3.3 outlines the settings used to generate these observations (occultation of Ganymede etc), and the resulting observation times should align with the expected operational schedule. The 3GM instrument relies on the high-gain antenna to communicate with the ground station on Earth, during which observations are conducted to determine JUICE's orbit. A daily 8-hour window is planned, during which the high-gain antenna points towards Earth to transmit data and perform radio science range and Doppler measurements (Van Hoolst et al. 2024). Figure 3.9 shows the observation times, during which a viable radio communication link can be established. There is a tracking pass of around 8 h each day, consistent with the scheduled 8 h to 9 h reported by the 3GM team (Cappuccio et al. 2020). The timing of the tracking passes gradually shifts over the 100 day period, influenced by the orbital geometry of JUICE

and the alignment of all occulting bodies. This verifies that the simulated observations are consistent with the expected real observations once the JUICE mission enters Ganymede's orbit (Boutonnet et al. 2024).

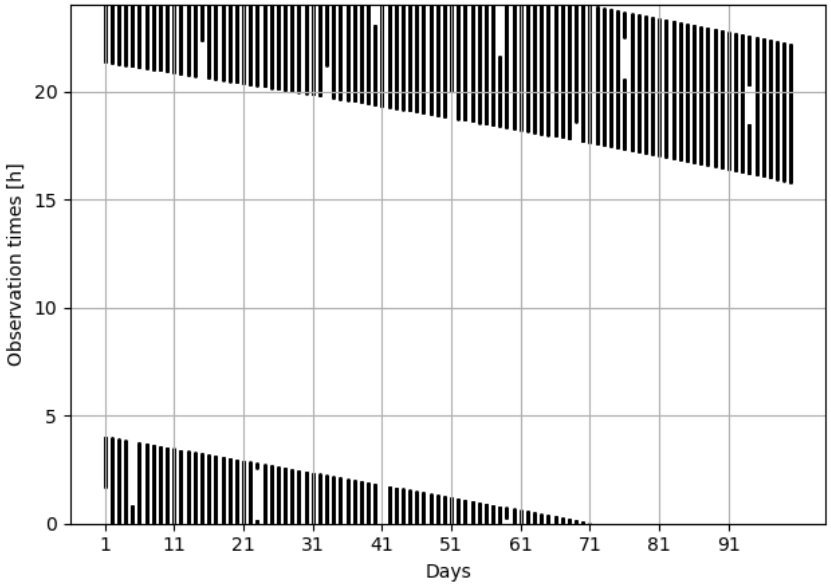

Figure 3.9: Observation times where direct contact of JUICE to ground station on Earth is possible over 100 days.

3.3.2. Partials in Design Matrix

To obtain the formal errors of Love numbers, the design matrix is computed. The design matrix, contains the partial derivatives of the observations to each estimated parameter. The general Tudat software is considered verified and is widely used for research. The mode coupled Love numbers and corresponding partials have been added for this work and must thus be verified. Assuming that a single mode coupled Love number (eg. k_{20}^{30}) is estimated, the design matrix contains the partials as shown in equation 3.22 in one of its columns. The left hand side partials are contained in one column, while the partials of the observations to the response gravity field coefficient ($\partial z/\partial C_{30}$) are contained in H as well, since the gravity field coefficients are part of the estimated parameters. The partials of the observations to the gravity field coefficients can be considered verified, as that is part of the publicly released Tudat software used in research. The right hand side partial ($\partial C_{30}/\partial k_{20}^{30}$) is new functionality and is computed by dividing the column of the specific Love number partials by the column of the response gravity field coefficient. The resulting partials ($\partial C_{30}/\partial k_{20}^{30}$) are analytically described by equation 3.23 and are equal to the tidal forcing at response degree and order (n,m) here (3,0).

The range and Doppler observations have been split and computed separately as they correspond to the same time frame. The resulting partials are computed over a time period of 10 days in GCO500. The partials obtained are converted to their real observation time to be able to plot them over time. The tidal forcing (V_{nm}) is plotted to verify if the partials have the correct shape and amplitude. The results for a degree 2 forcing are shown in Figure 3.10, comparing the existing order-varying Love number function (top row) to the new mode coupled Love numbers (bottom row). Both functions produce equivalent results, while the amplitude and distribution of computed partials for both range and Doppler measurements follows roughly the expected forcing signals. This is more evident for the (2,0) response than the (2,2) response, where they show a much wider spread. The (2,1) forcing and partials are both 0, as a result of the assumed rotation model for Ganymede. Since there are roughly 10 continuous tracking passes during the 10 days, the partials are grouped into 10 separated data fields. Due to the noise added to the simulated observations, the computed partials are normally distributed around the expected value leading to the vertical stripes observed.

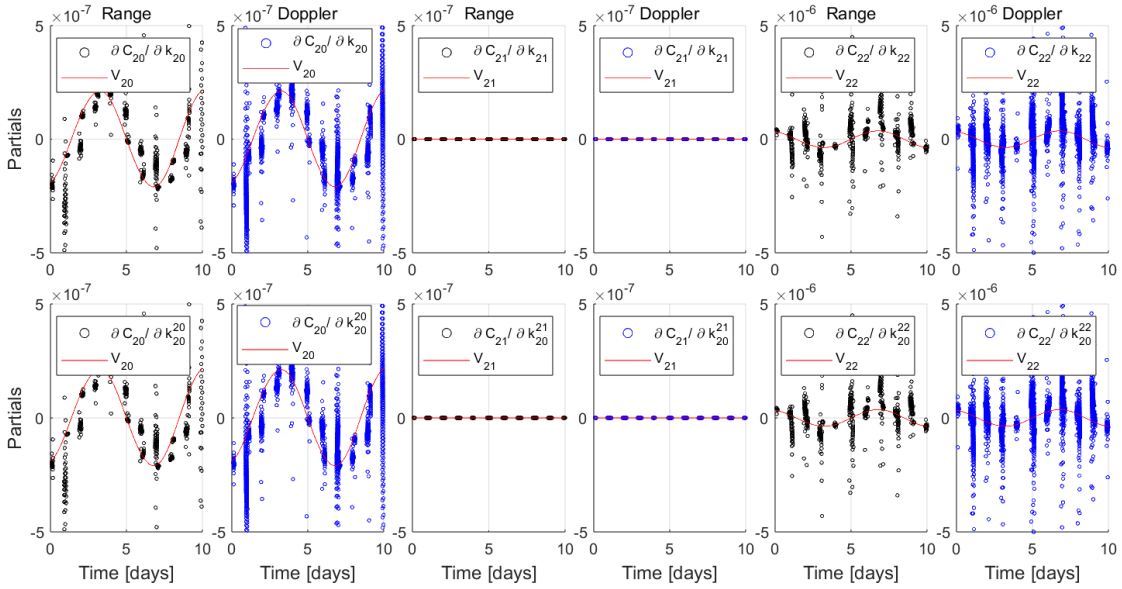

Figure 3.10: Partials ($\partial C_{nm}/\partial k^{nm}_{n_\alpha m_\alpha}$) obtained from design matrix for degree 2 forcing diagonal Love numbers. Top row: Results from order varying Love number function (k_{nm}). Bottom row: Results from mode coupled Love number function. Range and Doppler observations are shown in black and blue respectively, tidal forcing signal shown in red.

Figure 3.11, shows similar results but for a degree 3 forcing. The Doppler and range observations have equal behavior and the range observations are omitted here. In both cases the diagonal Love numbers produce equivalent results, regardless whether mode coupled or existing functions are used. The (3,0) and (3,2) signals and partials are zero due to the assumed rotation model. FOr a (3,1) and (3,3) response the partials have a constant offset of roughly 2×10^{-7}, while the forcing signals are on the order of 1×10^{-9}. This might have to do with correcting the permanent tide for degree 3 forcing where a manual offset was applied.

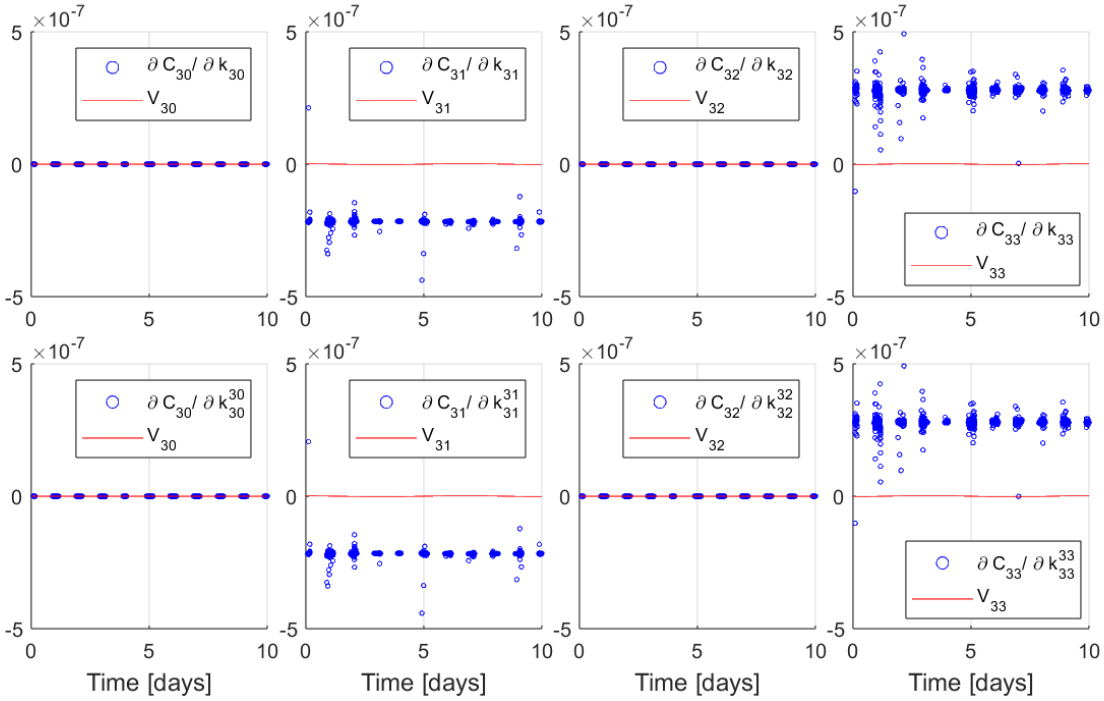

Figure 3.11: Partials ($\partial C_{nm}/\partial k^{nm}_{n_\alpha m_\alpha}$) obtained from design matrix for degree 3 forcing diagonal Love numbers. Top row: Results from order varying Love number function (k_{nm}). Bottom row: Results from mode coupled Love number function. Doppler observations are shown in blue and tidal forcing signals in red.

Figure 3.12, shows the partials computed from Doppler observations for the case of mode coupled Love numbers and a forcing of (2,0). In all responses, the magnitude of partials follows the expected shape of (V_{20}), which shows that also off-diagonal Love numbers with responses different to the forcing wavelength are calculated correctly.

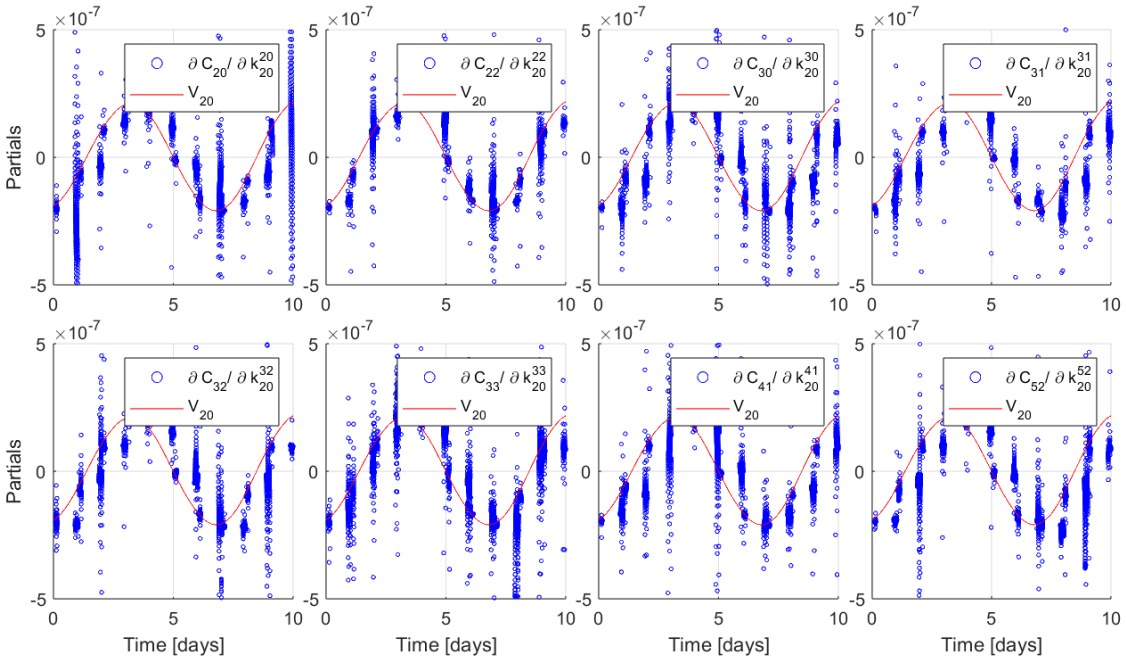

Figure 3.12: Partials ($\partial C_{nm}/\partial k^{nm}_{20}$) obtained from design matrix for (2,0) forcing off-diagonal Love numbers. Doppler observations are shown in blue and tidal forcing signals in red.

3.3.3. Magnitude of Formal Errors

In Section 3.2.1, the tide model was extended with the implemented of extended Love numbers in Tudat. To verify the correct functionality of this new implementation, the uncertainty of degree 2 Love numbers is obtained using all available functions and compared. The results obtained with the mode-coupled Love number function are expected to align with the uncertainties produced by the pre-existing, well-tested functions for k_n and k_{nm}, as summarized in Table 3.1. The covariance analysis is repeated for a number of simulations, using the parameters and settings from Table 3.3 and with different settings for the time-varying gravity field.

Table 3.4 shows the results of all simulations performed during verification. The Love numbers defined in the dynamical model are given in the second column, while the results with and without correcting for the permanent tide are shown column 3 and 4. In the first simulation, the traditional Love number k_2 is estimated, simulations 2 and 3 repeat the estimation with order-varying Love numbers (k_{20}, k_{21}, k_{22}) and mode coupled Love (k_{20}^{20}, k_{21}^{21}, k_{22}^{22}). Simulations 4-6 are identical but estimating degree 3 Love numbers.

Table 3.4: Verification of uncertainties obtained from covariance analysis over 100 days GCO500 with different tide models.

Simulation	Time-varying gravity field settings	Results with permanent tide correction
1	$k_2 = 0.469$	$\sigma_{k_2} = 1.854 \times 10^{-4}$
2	$k_{20} = 0.469$ $k_{21} = 0$ $k_{22} = 0.469$	$\sigma_{k_{20}} = 4.414 \times 10^{-4}$ $\sigma_{k_{21}} = 3.322 \times 10^{9}$ $\sigma_{k_{22}} = 2.053 \times 10^{-4}$
3	$k_{20}^{20} = 0.469$ $k_{21}^{21} = 0$ $k_{22}^{22} = 0.469$	$\sigma_{k_{20}^{20}} = 4.414 \times 10^{-4}$ $\sigma_{k_{20}^{20}} = 3.322 \times 10^{9}$ $\sigma_{k_{22}^{22}} = 2.052 \times 10^{-4}$
4	$k_3 = 0.281$	$\sigma_{k_3} = 3.158 \times 10^{-2}$
5	$k_{30} = 0$ $k_{31} = 0.281$ $k_{32} = 0$ $K_{33} = 0.281$	$\sigma_{k_{30}} = 1.845 \times 10^{12}$ $\sigma_{k_{31}} = 9.440 \times 10^{-2}$ $\sigma_{k_{32}} = 1.825 \times 10^{12}$ $\sigma_{k_{33}} = 3.322 \times 10^{-2}$
6	$k_{30}^{30} = 0$ $k_{31}^{31} = 0.281$ $k_{32}^{32} = 0$ $k_{33}^{33} = 0.281$	$\sigma_{k_{30}^{30}} = 1.845 \times 10^{12}$ $\sigma_{k_{31}^{31}} = 9.440 \times 10^{-2}$ $\sigma_{k_{32}^{32}} = 1.825 \times 10^{12}$ $\sigma_{k_{33}^{33}} = 3.322 \times 10^{-2}$

The results of the new function (3) produce identical results to the existing tide model in Tudat (2), confirming that the mode coupled Love numbers produce correct results when the traditional diagonal Love numbers are estimated (forcing = response wavelength). Estimating a single degree k_2 Love number (1) leads to an uncertainty that is twice as low as the corresponding estimates of k_{20}, k_{20}^{20}. This is true for both existing and new tide functions and arises as in the latter two cases (2 and 3) 3 parameters are estimated instead of 1 parameters for simulation 1. Consistent results are also obtained for degree 3 estimations as seen in simulation 4-6. It has also been verified that the resulting uncertainties do not change when the parameter with high uncertainty k_{21} is left out of the estimation.

The formal errors of k_{21}, k_{30} and k_{32} are all very large 1×10^9 to 1×10^{12}, which implies that the JUICE mission is not sensitive to these signals and cannot measure them. This is a result of the synchronous rotation model assumed which leads to parts of the tidal force having zero contribution. These correspond to coefficients $\bar{C}_{21}$,$\bar{C}_{30}$ and $\bar{C}_{32}$ which are all zero, see figures 3.4 and 3.5. In reality, these

tidal forcing contributions do exist and with different models used an uncertainty of k_{21} could be assessed.

In section 3.2.1, the mean value of each gravity field coefficient was computed and removed to correct for the static permanent tide. Results after applying this correction are shown in Table 3.4, but only differ from the uncorrected case by at most 4×10^{-6} for k_{20}^{20} and are basically equivalent for degree 3 estimations. Although the magnitude of the tidal forcing after removal of the permanent tide reduces from 1×10^{-5} to 1×10^{-7} for the $\bar{C}_{20}$ coefficient, there seems to be little effect on the resulting uncertainty.

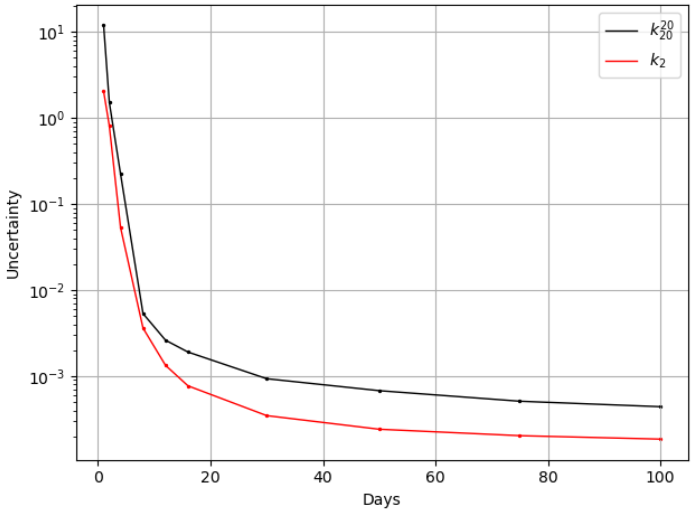

Figure 3.13: Estimated uncertainty in k_2 and k_{20}^{20} Love numbers as a function of the number of days during GCO500.

The uncertainty of estimated Love numbers can be compared when running the covariance analysis for a range of different time frames. Figure 3.13 illustrates the estimated uncertainty in the k_2 and k_{20}^{20} Love numbers as a function of the number of days propagated during GCO500. The x-axis represents the number of days propagated, while the y-axis shows the estimated uncertainty in each Love number. The uncertainty decreases exponentially when only a few days are spend in GCO500, thus the result is highly sensitive to the number of days spend in orbit. When the simulation time increases beyond 50 days, only marginal changes in the uncertainty are observed (eg. 1×10^{-4} going from 75 to 100 days). The uncertainty of the new function (k_{20}^{20}) exhibits the same behavior as the already implemented function for k_2. This also shows that to achieve an uncertainty below 1×10^{-3}, the JUICE mission must stay in orbit at least 20 days to 30 days.

3.3.4. Gravity Field

Table 3.5 presents the obtained uncertainties of Ganymede's gravitational parameter, its degree 2 coefficients and the single degree Love number k_2. To assess whether the obtained uncertainties are in the correct order of magnitude they can be compared to the corresponding values reported by the 3GM science team. As seen in the second row of table 3.5, the gravity field uncertainties obtained are close for $\bar{C}_{21}$, $\bar{S}_{21}$ and $\bar{C}_{22}$ and a factor of 5-10 lower for GM, $\bar{C}_{20}$ and $\bar{S}_{22}$. The uncertainty of the k_2 Love number is on the same order of magnitude also when looking at the results obtained with the mode coupled Love number $\sigma_{k_{20}^{20}} = 4.4\times10^{-4}$. Although the general setup and parameters of this research and the study done by (Cappuccio et al. 2020) are similar, the type of estimated parameters and their constraints differ and not all of their model choices (eg. rotation model of Ganymede) are known. The results should thus not be taken as true model, but act as a good verification comparison.

Table 3.5: Estimated uncertainties of Ganymede's GM, degree 2 normalized gravity field coefficients and k_2 Love number. Results obtained from covariance analysis using parameters from Table 3.3 in row 1 and uncertainties reported by 3GM science team in row 2, adapted from (Cappuccio et al. 2020).

	GM	$\bar{C}_{20}$	$\bar{C}_{21}$	$\bar{S}_{21}$	$\bar{C}_{22}$	$\bar{S}_{22}$	k_2
Results	1.2×10^{-3}	7.83×10^{-11}	8.60×10^{-11}	5.18×10^{-11}	1.17×10^{-10}	1.44×10^{-10}	1.8×10^{-4}
3GM team	3.8×10^{-4}	3.84×10^{-10}	1.06×10^{-10}	4.49×10^{-11}	1.61×10^{-10}	2.74×10^{-9}	1×10^{-4}

The 3GM team also reports the gravity field spectrum, computed from the normalized gravity field coefficients and resulting in a mean power value per degree. The mean degree power is computed as (Cappuccio et al. 2020):

$$\bar{C}_n = \sqrt{\frac{1}{2n+1} \sum_m (\bar{C}_{nm}^2 + \bar{S}_{nm}^2)} \tag{3.26}$$

Figure 3.14 shows the gravity spectrum reported by the 3GM team, with the uncertainty as dashed line and simulated gravity field for ($A_k = 4$) as solid line. The results of the covariance analysis can be computed as mean degree power using equation 3.26 and are plotted in red in Figure 3.14. As expected, the uncertainty per degree of estimated gravity field coefficient rises. The slope of both results is consistent, while the order of magnitude obtained from this covariance analysis is around one order of magnitude lower than by the 3GM team. Different to the 3GM results, the covariance stops at degree 15.

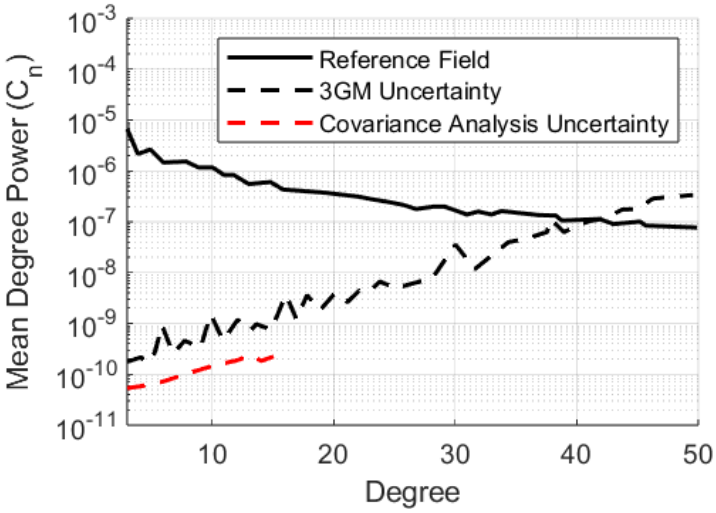

Figure 3.14: Uncertainty of Ganymede gravity power spectra obtained from covariance analysis in red compared to uncertainty reported by 3GM science team in dashed black. Simulated gravity field in solid black with Kaula coefficient $A_k = 4$. Results use parameters from Table 3.3 and 3GM report (Cappuccio et al. 2020).

3.3.5. Empirical Accelerations

In this study, the estimated empirical accelerations are defined locally, hence for 100 arcs an additional 300 parameters are estimated. It is important to check that this does not lead to an overall degradation of other estimated parameters, specifically the Love numbers. Figure 3.15 shows the correlation matrix of experiment 1, where degree 2 and 3 diagonal Love numbers are estimated. The first 600 parameters show high correlation to the observations as these are the arc-wise initial states of JUICE. There are visible but quite weak correlations of parameters 853-1100 which are part of the 300 empirical accelerations to the initial states. The uncertainty of empirical accelerations over time is shown in Figure 3.16, showing that

at arc 60, the uncertainty increases by a factor of 3, corresponding to the arcs with less correlation to the empirical accelerations.

The 3GM team treats the empirical accelerations as global parameters reducing the set of parameters to only 3. Switching to global empirical accelerations reduced the difference of results with respect to their results, however it is not clear which method is 'better suited'. For the estimated uncertainties, the choice of local and global empirical accelerations did not change the magnitude and thus conclusion of results in this work.

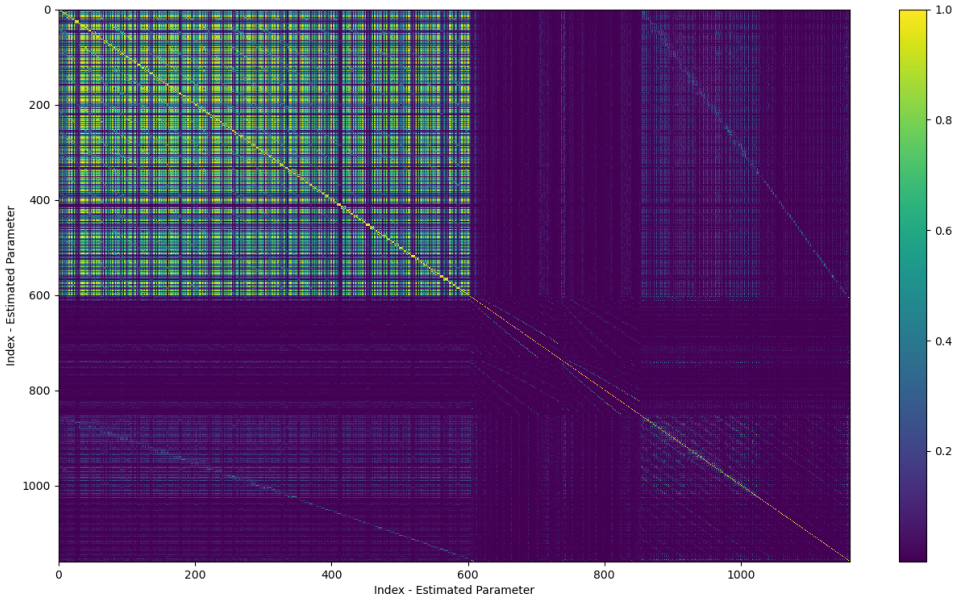

Figure 3.15: Correlation matrix of Experiment 1, estimating diagonal degree 2 and 3 Love numbers with arc-wise constant empirical accelerations.

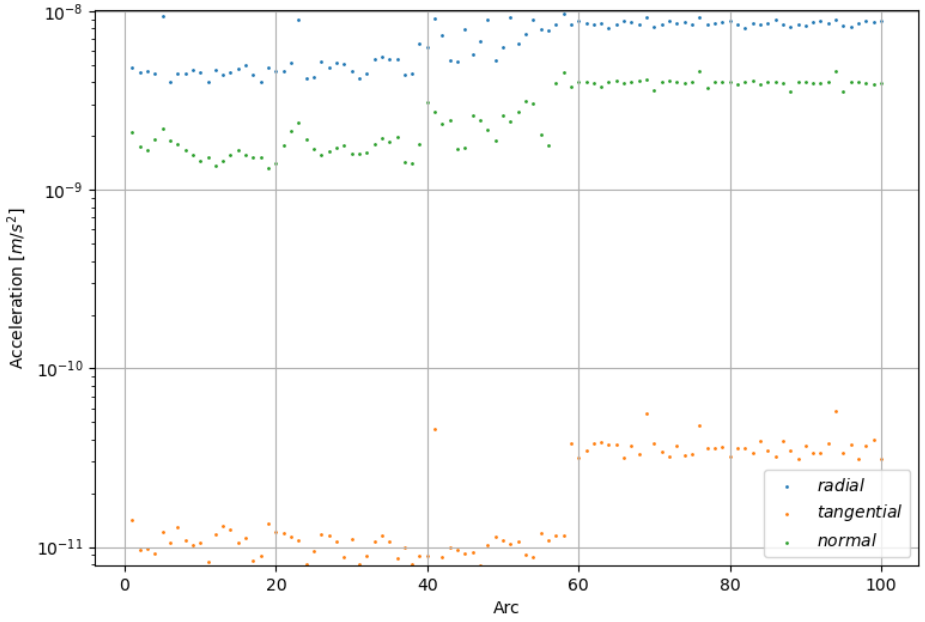

Figure 3.16: Formal uncertainty of empirical accelerations estimated in experiment 1. Radial, tangential and normal direction of JUICE per arc.

3.4. Results

This section reports the results obtained from performing a covariance analysis of JUICE to the tidal response of Ganymede with lateral variations in its interior. Simulated range and Doppler observations are used with realistic measurement noise during 100 days of the GCO500 phase to estimate the real part of the mode coupled Love numbers. All results are performed using the parameters and simulation settings described in Table 3.3 and with the new tide function (mode coupled Love numbers) implemented in Section 3.2.1. The assumption is made that the tide is fully observable by JUICE. The expected accuracy in measuring mode coupled Love numbers with JUICE is computed for a set of four different experiments that increase in complexity and number of parameters estimated. The experiments considered are described in Table 3.6.

Table 3.6: Experiments performed during covariance analysis of JUICE during GCO500 with settings from Table 3.3.

Experiment	Estimated Love numbers	Description
1	$k_{20}^{20}, k_{21}^{21}, k_{22}^{22}, k_{30}^{30}, , k_{31}^{31}, k_{32}^{32}, k_{33}^{33}$	Diagonal Love numbers of degree 2 and 3.
2	$k_{20}^{20}, k_{20}^{30}, k_{22}^{22}, k_{22}^{32}$	Largest tidal signals expected for purely zonal lateral variations.
3	$k_{20}^{20}, k_{20}^{22}, k_{20}^{30}, k_{20}^{31}, k_{20}^{32}, k_{20}^{33}, k_{20}^{41}, k_{20}^{52}$	Largest tidal signals due to (2,0) forcing
4	$k_{20}^{20}, k_{20}^{22}, k_{20}^{30}, k_{20}^{31}, k_{22}^{20}, k_{22}^{22}, k_{22}^{31}, k_{22}^{32}, k_{22}^{33}$	Largest tidal signals due to (2,0) and (2,2) forcing

In experiment 1, all diagonal Love numbers corresponding to a tidal forcing at degree 2 and 3 (k_{2m}^{2m}, k_{3m}^{3m}) are estimated. These are the parameters typically estimated in similar gravity determination studies. Assuming that the Love numbers at one degree are not equal (eg $k_{20}^{20} \neq k_{22}^{22}$), this implies lateral thickness variations (H) in the interior. Experiment 2 estimates the Love numbers arising due to a degree 2 forcing and purely zonal lateral variations in the interior (H_{10}, H_{20}, H_{30}). These include the degree 3 responses (k_{20}^{30} and k_{22}^{32}), which are the leading mode signals arising for these types of lateral variations. In the third experiment, all leading mode signals for lateral variations ranging from degree 1 up to degree 3 are estimated ($H_{10}, H_{11}, .., H_{33}$) for a tidal forcing at (2,0) only. This includes higher order responses up to degree 5 (k_{20}^{41} and k_{20}^{52}). The degree 4 and 5 responses arise due to shorter wavelength lateral variations of degree 3. In experiment 4, the contribution of both eccentricity tides (2,0) and (2,2) is included and 9 leading mode Love numbers up to degree 3 are estimated. These correspond to having lateral variations of type $H_{10}, H_{11}, H_{20}, H_{22}, H_{30}, H_{31}$ in the ice shell.

The resulting uncertainties of the estimated Love numbers for the four experiments are provided in Table 3.7. The correlation of the estimated Love numbers and their corresponding degree 2 and 3 gravity field coefficients is shown in Figure 3.17. The results of experiment 1 have been used for verification against literature in Section 3.3 but are discussed here for completeness. The results show that the uncertainty in estimating degree 2 diagonal Love numbers is $\sigma_{k_{20}^{20}} = 4.4 \times 10^{-4}$ and $\sigma_{k_{22}^{22}} = 2.1 \times 10^{-4}$. Comparing this to the values of k_2 of Ganymede ($k_2 = 0.469$) these signals are realistically measurable. Due to the assumption that there is no obliquity tide (see rotation model chosen), there is a high uncertainty and thus no sensitivity of JUICE to measure k_{21}^{21}, k_{30}^{30} and k_{32}^{32}. The uncertainty of degree 3 diagonal Love numbers is $\sigma_{k_{31}^{31}} = 9.4 \times 10^{-2}$ and $\sigma_{k_{33}^{33}} = 3.3 \times 10^{-2}$. The expected degree 3 Love number of Ganymede is equal to $k_3 = 0.281$, see Section 4.2. The formal uncertainties of a covariance analysis tend to be on the optimistic side, depending on the estimation technique used (Park et al. 2011). Considering this and assessing the magnitude of degree 3 uncertainties ($\sigma_{k_{33}^{33}} \approx 0.1$), this would imply that degree 3 Love numbers lie on the verge of detectability.

The uncertainty in k_{22}^{22} is a factor of 2 lower than for k_{20}^{20} suggesting that JUICE is more sensitive to observing the tidal response corresponding to degree and order (2,2) than (2,0). The correlation matrix for experiment 1 reveals that the Love numbers are correlated with their corresponding response-type gravity field coefficients, such as k_{30}^{30} with C_{30} and so on. This correlation is particularly strong for $k_{31}^{31}$and k_{33}^{33}, which show significant correlation with C_{31} and C_{33}, respectively. This suggests that the tidal (time-varying) effects at these wavelengths are difficult to separate from the static contributions to the gravity field. The effects of a forcing at degree 3 are two orders of magnitude smaller, which is also

visible in the uncertainties of k_{3m}, making it difficult to observe these higher order tidal responses.

Table 3.7: Combined results of experiments 1 to 4. Uncertainties of estimated Love numbers obtained from covariance analysis of JUICE during the GCO500 phase. Parameters and models are taken from Table 3.3.

Experiment	Parameter	Uncertainty
Experiment 1	k_{20}^{20}	4.414×10^{-4}
	k_{21}^{21}	3.322×10^{9}
	k_{22}^{22}	2.053×10^{-4}
	k_{30}^{30}	1.845×10^{12}
	k_{31}^{31}	9.440×10^{-2}
	k_{32}^{32}	1.825×10^{12}
	k_{33}^{33}	3.322×10^{-2}
Experiment 2		
	k_{20}^{20}	4.41×10^{-4}
	k_{20}^{30}	4.17×10^{-4}
	k_{22}^{22}	2.05×10^{-4}
	k_{22}^{32}	1.38×10^{-4}
Experiment 3		
	k_{20}^{20}	4.80×10^{-4}
	k_{20}^{22}	7.85×10^{-4}
	k_{20}^{30}	4.18×10^{-4}
	k_{20}^{31}	4.18×10^{-4}
	k_{20}^{32}	4.56×10^{-4}
	k_{20}^{33}	1.73×10^{-4}
	k_{20}^{41}	3.88×10^{-4}
	k_{20}^{52}	3.99×10^{-4}
Experiment 4		
	k_{20}^{20}	2.046×10^{-1}
	k_{20}^{22}	1.770×10^{-3}
	k_{20}^{30}	4.175×10^{-4}
	k_{20}^{31}	6.430×10^{-4}
	k_{22}^{20}	1.181×10^{-1}
	k_{22}^{22}	4.662×10^{-4}
	k_{22}^{31}	1.926×10^{-4}
	k_{22}^{32}	1.389×10^{-4}
	k_{22}^{33}	9.280×10^{-5}

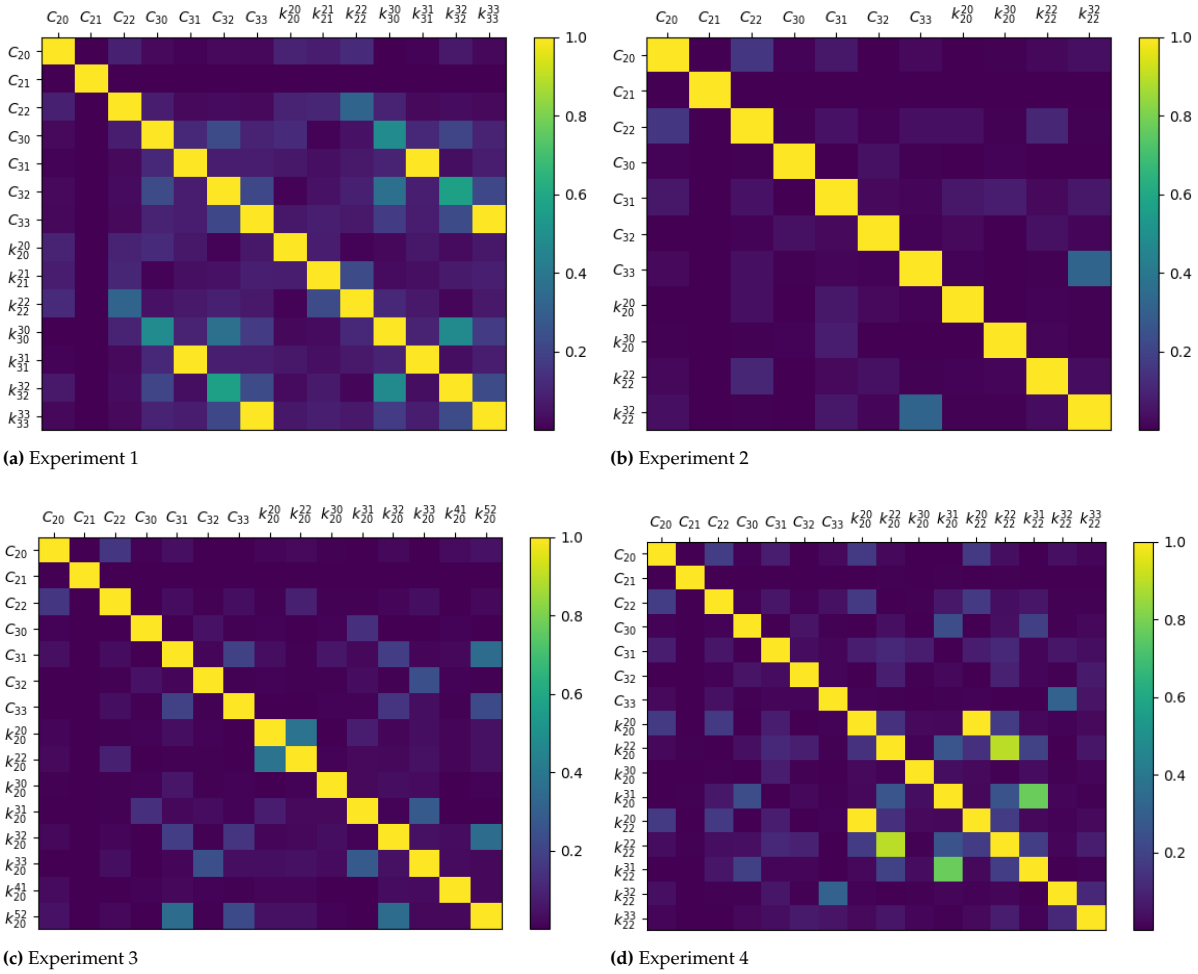

(a) Experiment 1

(b) Experiment 2

(c) Experiment 3

(d) Experiment 4

Figure 3.17: Correlation matrix of the four experiments showing the correlation of estimated Love numbers and gravity field coefficients (C_{nm}) up to degree and order 3. Darker colors indicate a lower correlation coefficient, while bright colors indicate a strong correlation of parameters.

In experiment 2, the formal error of the degree 2 diagonal Love numbers remains equal, while the degree 3 response signals are similar in magnitude to their degree 2 response ($\sigma_{k_{20}^{30}} \approx \sigma_{k_{20}^{20}}$ and $\sigma_{k_{22}^{33}} \approx \sigma_{k_{22}^{22}}$). These results suggest that JUICE is equally sensitive to a degree 2 and degree 3 response. This is not expected, since a higher order response, and off-diagonal Love number (k_{2m}^{3m}) should in theory be significantly harder to measure and a higher uncertainty than the diagonal Love numbers is expected. The tidal perturbation of the gravity field given by equation 3.21a is proportional to the ratio $(R/r)^{n+1}$. For $R = 2631.2km$ and $r \approx 2631.2 + 500$ the ratio of degree 2 to 3 response is around 0.84. Thus the signal expected at degree 3 should be roughly a factor 0.84 smaller than at degree 2 and the uncertainty of degree 3 is expected to be $1/0.84$ higher.

The same justification can be applied to the results of experiment 3, where Love numbers associated with the leading modes of lateral variations of degree 1 up to 3 are estimated. The uncertainty of a degree 5 response (k_{20}^{52}) shows the same magnitude as the lower order responses. Here, the expected uncertainty of degree 5 should be roughly twice as high as for degree 2 ($\sigma_{k_{20}^{5m}} \approx 2 \cdot \sigma_{k_{20}^{2m}}$) since the tidal potential scales with a factor of $(R/r)^3 \approx 0.5$.

Increasing the number of estimated parameters also degrades the overall quality of results and leads to more correlations between estimated Love numbers. This is seen in Figure 3.17 where experiment 3 shows significantly more correlation in Love numbers than experiment 2. The correlation matrix of experiment 4 is especially interesting, since certain pairs of Love numbers have strong correlation. In experiment 4, both forcing contributions of degree and order (2,0) and (2,2) were considered which

directly results in some estimated Love numbers of the same response and different forcing to be correlated (eg. k_{20}^{20} and k_{22}^{20}). The formal uncertainty in these parameters is large ($\sigma \approx 0.1$) which is significantly larger than the remaining parameters and means JUICE would not be sensitive to these signals.

To understand this effect, it is useful to introduce the concept of effective Love numbers. The gravity signal arising at a specific response mode can be rearranged from equation 3.21a:

$$\Delta\bar{C}_{nm} = k_{n_\alpha m_\alpha}^{nm} \Phi_{n_\alpha m_\alpha}^{T} \tag{3.27}$$

JUICE observes the tides indirectly by measuring and estimating the gravitational field at Ganymede. The signal measured by JUICE at a specific wavelength (n,m) is determined by $\Delta\bar{C}_{nm}$, the Love number relating the response to the tidal force and the forcing at degree and order (n_α, m_α). When only one forcing mode is considered, as done in experiment 1 to 3, there is one estimated parameter for each response wavelength and no problem with correlating parameters.

A tidal signal can contain contributions from multiple forcing wavelengths. The spacecraft does not measure the individual forcing contributions and extended Love numbers but observes the complete response, defined by the gravity field coefficient $\bar{C}_{nm}$ at degree and order (n,m). Therefore, effective Love numbers ($\bar{k}$) can be defined that introduce the effect of having multiple signals in the gravitational response:

$$\Delta\bar{C}_{nm} = \sum_{n_\alpha m_\alpha} \bar{k}_{nm} \Phi_{n_\alpha m_\alpha}^{T} -> e\,g.\; k_{20}^{20}\Phi_{20}^{T} + k_{22}^{20}\Phi_{22}^{T} \tag{3.28}$$

As seen in experiment 4, both a forcing at (2,0) and (2,2) creates a tidal response at the (2,0) wavelength and these responses overlap into one signal, leading to the high correlation of parameters k_{20}^{20} and k_{22}^{20}. The Love numbers corresponding to the response signal $\bar{C}_{20}$ have a correlation of 1 and are thus completely dependent. The remaining two pairs of Love numbers $(k_{20}^{22} - k_{22}^{22})$ and $(k_{20}^{31} - k_{22}^{31})$ do not suffer from high formal errors and have uncertainties on the order of 1×10^{-4}, even though they have a correlation of roughly $\rho \approx 0.7$.

These results suggest that JUICE is able to recover the individual signals contributing to the $\bar{C}_{22}$ gravity field response but is cannot distinguish the signals contributing to $\bar{C}_{20}$. The extent to which the tide can be observed is dependent on the orbit geometry (Park et al. 2011). The GCO500 orbit has a high inclination and is optimal to estimate the static gravity field and observe the complete surface, as most of the surface is uniformly sampled, see Figure 3.7. The C_{20} response is associated with the oblateness of Ganymede and does not have longitudinal variation (zonal term). The C_{22} term varies with longitude and latitude and thus one explanation could be that JUICE is able to sample this component at different longitudes over time making it more sensitive and able to distinguish tidal contributions. The same argument goes for C_{31}, but the degree component is additionally much smaller in magnitude which makes it harder to resolve any contributing effects.

In addition to the covariance analysis, an estimate of the higher order responses of experiment 2 can obtained (k_{20}^{30} and k_{22}^{32}). From the relation of gravity field coefficients to the Love numbers given in Equation 3.27 the uncertainty can be estimated. If there are no significant correlations and the tide is assumed observable, the uncertainties can be related as such:

$$\sigma_{\bar{C}_{nm}} \approx \sigma_{k_{n_\alpha m_\alpha}^{nm}} \Phi_{n_\alpha m_\alpha}^{T} \tag{3.29}$$

Using the uncertainty obtained during the covariance analysis ($\sigma_{k_3} \approx 0.1$ as conservative estimate), and given that the magnitude of the tidal force for degree 2 and 3 was shown to be 1×10^{-7} and 1×10^{-9} respectively, an approximation of the expected uncertainty of the off-diagonal Love number ($\sigma_{k_{20}^{30}}$) can be found.

$$\sigma_{k_{2m}^{3m}} \approx \Phi_{3m}^{T} \sigma_{k_{3m}^{3m}} / \Phi_{2m}^{T} = 1 \times 10^{-3} \tag{3.30}$$

To assess the expected uncertainty of degree 2 and 3 tidal signals caused by zonal lateral variations, the uncertainty of gravity field coefficients is used (1×10^{-10}) (Cappuccio et al. 2020). Zonal lateral variations of H_{10} and H_{20} induce tidal signals corresponding to the Love numbers of experiment 2. The additional signals due to H_{10} and H_{20} are $k_{2m}^{2m}\Phi_{2m}^{T}$ and $k_{2m}^{3m}\Phi_{2m}^{T}$ respectively. Figure 3.18 shows the relevant tidal forcing (V_{nm}) signals of degree 2 and 3, with the permanent tide removed. The shaded region marks the expected uncertainty of gravity coefficients. The black lines are the signals corresponding to a spherically symmetric Ganymede (eg. $k_3 V_{3m}$). The red and green lines are the the expected time-varying signals arising due to lateral variations in the ice shell thickness variations of 10% in (1,0) and (2,0) respectively.

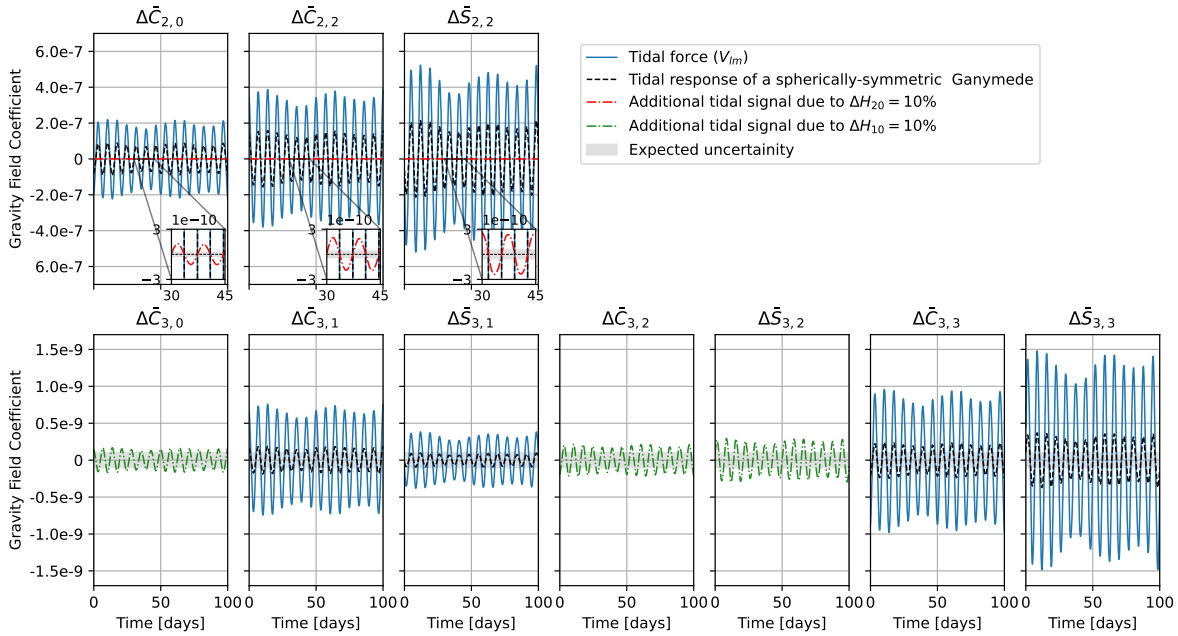

Figure 3.18: Tidal forcing without permanent tide at Ganymede induced by Jupiter V_{lm} and additional tidal signals arising expressed in terms of time-varying gravity field coefficients. The spherically symmetric response, and signals from lateral variations H_{10} and H_{20} are shown (amplitude 10%). Shaded region marks the expected uncertainty of JUICE in observing gravity field coefficients (1×10^{-10}).

The signals in Figure 3.18 are of similar magnitude but slightly larger than the assumed uncertainty of gravity field coefficients measured by JUICE. Sine these signals correspond to Love numbers arising for thickness variations of 10%in the ice shell, these zonal lateral variations are detectable.

4

Sensitivity of Love numbers to lateral variations in Ganymede

This chapter presents a sensitivity analysis of Love numbers to lateral variations in Ganymede and explores the expected tidal signals for various interior configurations to answer research sub-questions 1 and 2. An interior model of Ganymede is constructed in section 4.1 based on the current state of knowledge about Ganymede and is implemented in the software LOV3D. Section 4.2 presents the tidal response of a spherically symmetric body, the response with lateral variations and the methodology of LOV3D in computing the Love numbers with lateral variations in Ganymede. It also addresses the experiments performed during the sensitivity study. Although the software LOV3D has been verified against other models, its numerical accuracy, new features such as a liquid ocean layer and general results are verified in Section 4.3. The results of the sensitivity study are presented and discussed in Section 4.4 after which a conclusion follows in Chapter 5, combining all findings with chapter 3 to address the research questions.

4.1. Interior Model of Ganymede

To simulate Ganymede's tidal response, a model of the moon's interior without lateral variations is needed as reference. During the sensitivity study, a large range of models with lateral variations are explored, based on this reference model. The chosen interior model of Ganymede corresponds to the current state of knowledge found in literature and therefore consists of five layers: a liquid metallic iron core, a silicate mantle, a high-pressure ice layer, a subsurface ocean and low pressure outer ice shell. Although the high pressure ice layers likely consist of several layers of different pressure induced variants of water ice (ice VI, ice V, etc.), these are modeled as one layer to simplify the sensitivity analysis.

Table 4.1 contains the orbital rate and period of Ganymede and known properties of Ganymede, that can be used as constraints on constructing interior models. With the gravitational parameter (GM) and moment of inertia (C/MR^2) of Ganymede known from Galileo observations, the interior model must be consistent to this data.

The model parameters are constant for each layer and the chosen parameters are shown in Table 4.2. The radius of each layer is taken from a Ganymede model with an ocean salinity of 10% $MgSO_4$ and a bottom melting temperature of the ice-Ih ice shell of 250 K, see (Vance et al. 2014). Although the interior is not well constrained, the models of (Vance et al. 2014), represent the latest state of knowledge on Ganymede's interior. Density and temperature profiles of the ocean and ice layers are construct using recent thermodynamic data and the corresponding equations of state of aqueous MgSO4 and various phases of ice. The model is consistent with the observations, mass and inertia of Ganymede as discussed in Section 2.1. The liquid iron core is a requirement for the, probably dynamo-driven, intrinsic magnetic

field observations of Ganymede and the liquid water layer agrees with the confirmed subsurface ocean on Ganymede, described in Section 2.1.

Table 4.1: Properties of Ganymede and available constraints from observations. Data taken from (Kamata et al. 2015; Schubert et al. 2004)

Symbol	Parameter	Quantity	Unit
GM	Gravitational parameter	9887.837 ± 0.003	$km^3 s^{-2}$
C/MR^2	Normalized moment of inertia	0.3115 ± 0.0028	-
ω	Orbital rate	1.016×10^{-5}	rad/s
P	Orbital period	7.155	days
R	Radius	2631.2 ± 1.7	km

The iron core has a radius of 713 km and density of 7030 kgm^{-3}, which corresponds to an iron-silicate (FeS) composition of 25 %. This is in agreement with the range of expected core sizes and densities of 5150 kgm^{-3} to 8000 kgm^{-3} for either 100% FeS or pure iron composition (Bland et al. 2009; Schubert et al. 2004). The thickness of each layer is thus: ice shell - 145.2 km, ocean - 31 km, high pressure ice - 654 km, mantle - 1088 km and core - 713 km. Values for the shear modulus (rigidity) of the mantle and ice layers are taken from (Kamata et al. 2016; Vance et al. 2018), from which the HP ice layer uses a representative mean value, being simplified to a single layer. The iron core and ocean layer are liquid and have a shear modulus of zero.

Each layer of the interior model is incompressible and purely elastic. Both of these are assumptions made in computing the tidal response. Only considering the elastic response neglects any viscoelastic long-term response and thereby any induced tidal phase lag between the sub Jovian point and the tidal bulge which might be up to a few degrees for k_2, but does not significantly influence its magnitude (Hussmann et al. 2016). The visco-elastic response is of interest when studying the process of energy dissipation through tides (tidal dissipation) or time-dependent effects such as the long-term relaxation of the ice shell. Regarding the short time-scale (100 days) of observations made by JUICE, this assumption is valid and simplifies the analysis. Incompressibility neglects changes in the volume as a result of the tidal forcing but this effect is typically not considered for icy moons.

Table 4.2: Parameters of reference interior model of incompressible and elastic Ganymede. Data from: (Kamata et al. 2016; Vance et al. 2014; Vance et al. 2018). Value of ρ_m adjusted to fit Ganymede's GM and C/MR^2 constraints.

Layer	Outer radius [km]	Thickness [km]	Density [kgm^{-3}]	Rigidity [GPa]
Core	713	713	7030	0
Mantle	1801	1088	3206.06	82
HP ice layer	2455	654	1310	6.5
Ocean	2486	1180	31	0
Ice shell	2631.2	145.2	1000	3.3

Surface temperature: 110 K

Fluid properties at ice-shell to ocean interface: $T = 250K$, $\alpha = -0.32 \times 10^{-4} K^{-1}$, $C_p = 2.24 \times 10^3 J/kg/K$

(Vance et al. 2014)

The total mass and moment of inertia can be calculated iteratively as a sum of spherical shells, using the

radius and density of each layer and starting from the core. The mass and axial moment of inertia of a spherical shell with constant density are given as:

$$M_1 = M_0 + \frac{4\pi}{3}\rho_1(R_1^3 - R_0^3) \tag{4.1}$$

$$C_1 = C_0 + \frac{8\pi}{15}\rho_1(R_1^5 - R_0^5) \tag{4.2}$$

The mass and moment of inertia of a given layer (M_1 and C_1) (eg. mantle) are calculated using information from the layer beneath it (eg. core), integrating upwards. The density of the silicate mantle was adjusted from its nominal value of 3250 kgm^{-3} (Vance et al. 2014) to 3206.06 kgm^{-3}, to ensure that both the mass and moment of inertia constraints from Table 4.1 are satisfied, resulting in an internally consistent interior model. The radius, gravitational parameter, and moment of inertia of Ganymede in the reference model (Table 4.2) are equal to the central values of the observation confidence intervals provided in Table 4.1.

4.2. Method of Obtaining the Tidal Response

With the interior model constructed, the tidal response of Ganymede can be calculated. This methodology is organized into three sections. First, the tidal response of a spherically symmetric body is derived in Section 4.2.1, providing the foundation for understanding Ganymede's basic tidal behavior. Section 4.2.2 describes the tidal response of a body with lateral variations, introducing the complexities of heterogeneous interior structures. Finally, the method used by LOV3D and the approach for the sensitivity analysis is presented in Section 4.2.3

4.2.1. Tidal Response of a Spherically Symmetric Body

The response of a self-gravitating celestial body to external forces such as the tidal potential by Jupiter on Ganymede can be obtained by solving the viscoelastic gravitational problem (Sabadini and Vermeersen 2004). A brief summary of the general approach is given here with the aim to derive the Love numbers of a spherically-symmetric body.

The approach starts with the momentum, Poisson and continuity of mass equations which need to be solved. The equations are linearised around an initial state of hydrostatic equilibrium, i.e. gravitational and pressure forces for the celestial body balance. In this way the incremental momentum, Poisson and mass equations are derived (Sabadini et al. 2016):

$$\nabla\boldsymbol{\sigma}^{\boldsymbol{\delta}} + \nabla(\mathbf{u}\cdot\nabla p_0) - \rho^{\Delta}\nabla\Phi_0 - \rho_0\nabla\Phi^{\Delta} - \rho^{L}\nabla\Phi_0 + M = 0 \tag{4.3a}$$

$$\nabla^2\Phi^{\Delta} = 4\pi G(\rho^{\Delta} + \rho^{L} + \rho^{T}) - 2\omega^2 \tag{4.3b}$$

$$\rho^{\Delta} = -\rho_0\Delta - \mathbf{u}\cdot\nabla\rho_0 \tag{4.3c}$$

where $\boldsymbol{\sigma}$ is the Cauchy stress tensor, $\mathbf{u}$ the displacement vector, G the gravitational constant, M the non-conservative forces and ω the angular velocity of the body. p, ρ, Φ are pressure, density and gravitational potential respectively. Δ is the volume variation of a particle. The density is split into incremental, load (L) and tidal(T) density, where the latter is relevant to analyse tides.

A constitutive equation is required, relating material incremental stress to strain and thus deformation. The Maxwell model has been widely used to describe the interior of a planetary body. It represents the rocky or icy interior of a body with an elastic spring and a viscous dash-pot as damper, describing elastic short term responses with spring rigidity (μ) and long term viscous effects with damper viscosity (ν) (Sabadini et al. 2016). In the Maxwell model, the spring and dash-pot components are arranged in series. In this way the modeled material that experiences instantaneous elastic deformation when loaded and infinite viscous relaxation when unloaded. There are various other viscoelastic models with a different configuration of components such as the Voigt-Kelvin or Andrade model (McCarthy and

Castillo-Rogez 2013; Renaud and Henning 2018), see Figure 4.1. The aim of these rheological models is to represent the real physical interactions of a material both on a micro- and macro-scale, seen in laboratory data and other observations (Renaud and Henning 2018)

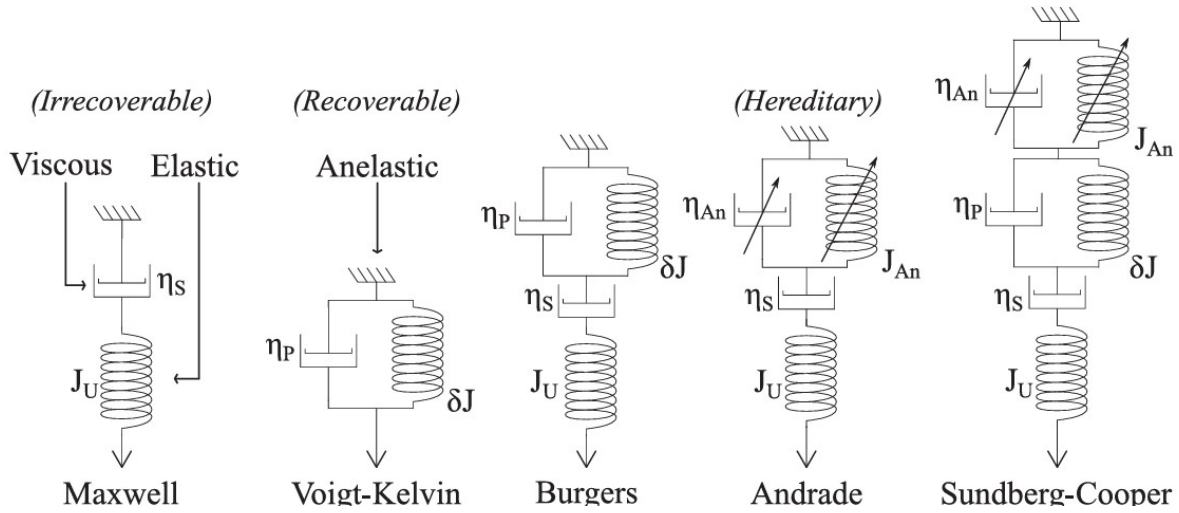

Figure 4.1: Examples of rheological models used in literature study. A Spring has rigidity J and a dashpot viscosity η. J_u represents the "unrelaxed" state, immediately after a load is applied. The defect compliance δJ is defined as the difference between the relaxed and unrelaxed states, $\delta J = J_r - J_u$. Subscript "An" stands for the hereditary mechanism, which retains some material memory after unloading. The arrows represent the ability to include a broad range of spring/damper constants for softening effects. Image Credit: (Renaud and Henning 2018)

As illustrated in Equation 2.4, the tidal forcing is time-dependent. Equations 4.3a-4.3c can be solved in the temporal domain or alternatively in the Laplace (normal mode) (Sabadini et al. 2016) or Fourier domain (Rovira-Navarro et al. 2024), to get the tidal response. The correspondence principle states that the viscoelastic solution in the time domain equals the elastic solution in the Laplace domain after Laplace transforming the constitutive stress/strain equation. The constitutive equation in the Laplace domain takes similar form as Hooke's law and is:

$$\sigma^{\delta} = \kappa \Delta I + 2\mu \epsilon_D \tag{4.4}$$

with κ the adiabatic bulk modulus, μ the shear modulus and ϵ_D deviatoric strain tensor.

The resulting incremental differential equations are transformed using spherical harmonics basis functions of order l and degree m, to only depend on radial direction. Assuming that initial parameters such as density and chemical composition vary only radially, the equations are simplified to only include the radial direction. Furthermore, the displacement vector $\mathbf{u}$ is decomposed into spheroidal ($\mathbf{u_S}$) and toroidal displacements ($\mathbf{u_T}$). Accordingly, the spherical harmonics vectors are $\mathbf{R_{lm}}$, $\mathbf{S_{lm}}$ and $\mathbf{T_{lm}}$ for radial spheroidal, tangential spheroidal and toroidal stresses. The scalar spherical harmonics coefficients $\Phi_{lm}, U_{lm}, V_{lm}$ and W_{lm} refer to potential, radial spheroidal, tangential spheroidal and toroidal displacements. The choice of this decomposition, separates between toroidal and spheroidal deformations (Sabadini et al. 2016).

The expression of the displacement vector in the traditional radial, tangential and toroidal decomposition is given by:

$$\mathbf{u}(r,\theta,\phi,t) = \sum_{l,m} (U^{+}_{lm}(r)\mathbf{R_{lm}}(\theta,\phi) + V^{+}_{lm}(r)\mathbf{S_{lm}}(\theta,\phi) + W^{+}_{lm}(r)\mathbf{T_{lm}}(\theta,\phi))e^{i\omega t} + c.c. \tag{4.5}$$

where c.c. refers to the complex conjugates and + to the $+\omega$ component of the tidal force (Rovira-Navarro et al. 2024).

For a spherically symmetric body, the spheroidal and toroidal equations are uncoupled and there are no toroidal displacements, thus $\mathbf{T_{lm}}$ and W_{lm} disappear. Six differential equations emerge that can be numerically integrated with proper boundary conditions, leading to the spheroidal solution vector $\mathbf{y_{lm}}$:

$$\mathbf{y_{lm}} = (U_{lm}, V_{lm}, \mathbf{R_{lm}}, \mathbf{S_{lm}}, \Phi_{lm}, Q_{lm},) \tag{4.6}$$

the components in order refer to radial and tangential displacements, radial and tangential stresses, potential and potential stress (Q_{lm}). The solution vector needs to solved at each forcing frequency and degree/order of spherical harmonics. The solution in Equation 4.6 can be also be expressed in terms of non-dimensional Love numbers (Love 1911). Evaluating the first, second and fifth component of $\mathbf{y_{lm}}$ at the surface of the body and at tidal forcing of degree 2 leads to the degree 2 Love numbers:

$$U_2 = \frac{h_2 \Phi_T}{g}, \qquad V_2 = \frac{l_2 \Phi_T}{g}, \qquad \Phi_2 = k_2 \Phi_T, \tag{4.7}$$

where g is the gravitational acceleration at the surface, and Φ_T is the tidal potential of degree 2. Ganymede deforms in response to a tidal potential raised by Jupiter (Φ_T), with the extent of the deformation depending on the assumed viscoelastic properties of its interior. The potential causes the body to form a solid tidal bulge in radial direction outwards and deform horizontally. There will also be a perturbation in the gravitational potential of Ganymede since it mass distribution changes. Love numbers h_2 and l_2 relate the resulting surface deformation in radial and tangential direction (U_2,V_2) to the forcing potential. Love number k_2 describes the resulting gravitational potential after the tidally induced redistribution of mass.

In case the body is spherically-symmetric, a specific tidal forcing only results in the same degree and order of tidal response. This means a degree 2 forcing produces a tidal response at degree 2, with the corresponding degree 2 Love numbers (k_2, h_2, l_2). Furthermore, the response is independent of the order of forcing and thus for each frequency-dependent forcing, there are a set of Love numbers. In the notation of Equation 4.7, the order of tidal forcing and degree of tidal potential are dropped. The Love numbers are complex variables, with the absolute value describing the magnitude of response and argument describing the tidal phase lag (Kamata et al. 2016; Rovira-Navarro et al. 2024).

4.2.2. Tidal Response of a Body with Lateral Variations

The method described in (Rovira-Navarro et al. 2024) transforms equations Equations 4.3a-4.3c to the spectral domain using tensor spherical harmonics. The stress tensor is decomposed into spheroidal and toroidal components and a Zerilli projection is performed (Zerilli 1970) to reduce the stress tensor from 9 to 6 independent components. The transformed equations are evaluated at each degree and order and radially integrated from the boundary layer to the surface. The solution vector is given by:

$$\mathbf{y} = (U_n^m, V_n^m, \mathbf{R_n^m}, \mathbf{S_n^m}, \Phi_n^m, \partial_r \Phi_n^m, W_n^m, \mathbf{T_n^m}, ...) \tag{4.8}$$

with the toroidal components of the displacement vector now coupled to the radial and tangential. $\Phi_n^m, \partial_r \Phi_n^m$ are the gravitational potential and its gradient.

With lateral variations accounted for in the interior, the solution vector is now much more complex. The response modes of different wavelength are coupled and a particular forcing of degree and order (n,m) might also excite response modes at different wavelengths other than the forcing mode (n,m). Also unlike in the spherically symmetric case, the order of response can not be neglected. In theory, this would result in an infinite set of response modes ie. from degree and order $(1/0), (1/1), (2/0)$ up to (∞/∞), making it impossible to obtain an exact solution to this problem.

However, only certain parts of the response are dominant, while the rest have very small amplitude. To what extent a certain response mode of degree and order (n,m) is involved in the tidal response, depends on the combination of forcing wavelength (n_f, m_f) and wavelength of lateral variations in

the interior (n_{LV}, m_{LV}). Selection rules can be used to obtain the coupling coefficients and a-priori higher order modes. This allows to cut off the response spectra to the most relevant part and get an approximate solution to the problem.

By recursively applying the selection rules, the coupled modes can be computed (Qin et al. 2014), resulting in first order modes $(n_f, m_f) \otimes (n_{LV}, m_{LV}) => (n_1, m_1)$, second order modes $(n_1, m_1) \otimes (n_{LV}, m_{LV}) => (n_2, m_2)$ and so on. The first-order response originates from coupling of the lateral variations wavelength and the forcing wavelength, while further couplings with the previous response (eg. first-order) lead to higher order responses (eg. second-order).

An example of mode couplings are illustrated in Figure 4.2. The coupling of wavelengths (2, 0) and (1, 1) in forcing and interior structure produce two spheroidal response modes $s^1(1,1)$, $s^1(3,1)$ and one toroidal response mode $t^1(2,-1)$. These first order modes couple with the interior structure to produce 5 additional modes.

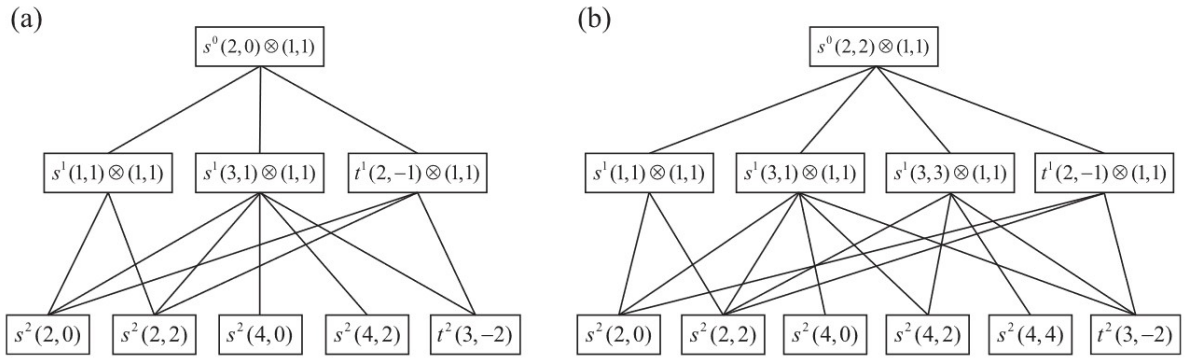

Figure 4.2: Example of mode couplings for a body with lateral variations of shear modulus of degree/order (1, 1) and a forcing of (a) (2, 0) and (b) (2, 2). Coupling modes up perturbation order 2 are shown. s and t are spheroidal and toroidal modes, while superscript 0, 1 and 2 denotes the response order number. Image Credit: (Qin et al. 2014)

If the outer shell is thin compared to the radius, shear modulus and shell thickness variations have equivalent effects in the tidal response, specifically the extension rigidity (Beuthe 2018). This is true when the thickness of the ice shell (H) is much smaller (below 5 % to 10 %) than the body's radius (R) ($(\frac{H}{R})^2 << 1$) so that bending effects are negligible. For Ganymede, the ice shell thickness is below that limit and allows to model a thickness variation in the outer ice shell (ΔH) directly via a variation in its shear modulus ($\Delta\mu$) (Qin et al. 2014):

$$\frac{\Delta\mu}{\mu_0} = \frac{\Delta H}{H_0} \tag{4.9}$$

where H_0 and μ_0 are the nominal thickness and shear modulus of the thin layer.

The tidal solution can be expressed in terms of complex Love numbers as explained in subsection 4.2.1. For bodies with lateral heterogeneity, a given forcing excites all other tidal response modes and the concept of love numbers has to be extended (Rovira-Navarro et al. 2024). A subset of the solution vector can then be rewritten to:

$$(U, V, W, \Phi) = \sum_{n_\alpha, m_\alpha} \sum_{n_\beta, m_\beta} (-\frac{h^{n_\beta,m_\beta}_{n_\alpha,m_\alpha}}{g_0}, -\frac{l^{n_\beta,m_\beta}_{n_\alpha,m_\alpha}}{g_0}, -\frac{t^{n_\beta,m_\beta}_{n_\alpha,m_\alpha}}{g_0}, \delta^{n_\beta}_{n_\alpha}\delta^{m_\beta}_{m_\alpha} + k^{n_\beta,m_\beta}_{n_\alpha,m_\alpha})\Phi^{(T)}{}^{m_\alpha}_{n_\alpha} Y^{m_\beta}_{n_\beta} e^{i\omega t} + c.c. \tag{4.10}$$

Compared to Equation 4.7, the solution of a laterally heterogeneous body contains the toroidal displacement (W). Love numbers $h^{n_\beta,m_\beta}_{n_\alpha,m_\alpha}$, $l^{n_\beta,m_\beta}_{n_\alpha,m_\alpha}$ and $t^{n_\beta,m_\beta}_{n_\alpha,m_\alpha}$ correspond to the radial, tangential and toroidal surface deformation of the body. The notation differs from Equation 4.7 as it differentiates between the degree and order of forcing (n_α, m_α) and of tidal response (n_β, m_β). $k^{n_\beta,m_\beta}_{n_\alpha,m_\alpha}$ represents the

gravitational Love numbers and δ the Kronecker Delta, which is 1 if $n_\alpha = n_\beta$ or $m_\alpha = m_\beta$ and 0 otherwise. By way of example, Love number $k_{2,0}^{3,1}$ describes the gravitational response at degree and order $(3,1)$ in response to a forcing at $(2,0)$. Equation 4.7 is a special case of the more general case in Equation 4.10 in which the only nonzero Love numbers are $k_{n_\alpha,m_\alpha}^{n_\alpha,m_\alpha}$, they are order independent and the extended Love number notation can be simplified to the standard k_n.

4.2.3. Sensitivity Study

The tidal response of Ganymede with lateral variations is obtained with the semi-analytical spectral method implemented in the code LOV3D, as detailed in (Rovira-Navarro et al. 2024). This new method agrees with results obtained by the perturbation approach (Qin et al. 2014) and FEM models (Berne et al. 2023; Berne et al. 2023) but its computational efficiency enables to simulate a large number of interior models in a short amount of time, which is essential for the sensitivity study.

As discussed in Subsection 4.2.2 shear modulus and ice shell thickness variations produce equivalent effects in the tidal response, given that the ice shell is thin compared to the radius and floating on a liquid layer (Beuthe 2018). In LOV3D, lateral variations are projected onto the reference model in terms of spherical harmonics:

$$\mu(r,\theta,\phi) = \mu_0(r) + \sum_{n\neq 0,m} \mu_0 \mu_n^m(r) \mathbf{Y}_\mathbf{n}^\mathbf{m}(\theta,\phi) \tag{4.11}$$

μ is the shear modulus at radius r, colatitude θ and longitude φ. $\mathbf{Y}_\mathbf{n}^\mathbf{m}$ are spherical harmonics at degree n and order m. An interior layer with lateral variations is defined by its mean shear modulus μ_0 and the amplitude (expressed in %) of peak-to-peak variations. The applied pattern of lateral variations is determined by the degree and order of spherical harmonics used, defining the spatial distribution of the variations across the layer.

As explained in Section 2.2, as a response to the time-dependent tidal forcing by Jupiter, Ganymede deforms and experiences a perturbation of its gravity field. Assuming Ganymede is in synchronous rotation and considering only eccentricity effects, this can be written as a sum of spherical harmonics as done in Equation 2.4. LOV3D works in the Fourier domain, where the tidal potential by Jupiter is generally written as:

$$\Phi^T(r,\theta,\varphi,t) = \sum_{n_\alpha,m_\alpha} \left((\frac{r}{R})^{n_\alpha} {\Phi^{(T)}}_{n_\alpha}^{m_\alpha,\omega} \mathbf{Y}_{\mathbf{n}_\alpha}^{\mathbf{m}_\alpha}(\theta,\varphi) e^{i\omega t} \right) \tag{4.12}$$

the complete response is a sum over the degree (n_α), order (m_α) and frequency (ω) of the forcing. ${\Phi^{(T)}}_{n_\alpha}^{m_\alpha,\omega}$ is the amplitude of the $+\omega$ component of the tidal forcing and depends on which tidal effects are considered. The tidal forcing frequency of Ganymede is equal to its orbital rate ($\omega = 1.016 \cdot 10^{-5}$) and the tidal forcing to this single forcing frequency can be written as:

$$\Phi^T(r,\theta,\varphi,t) = {\Phi^{(T)}}_{n_\alpha}^{m_\alpha,+} \mathbf{Y}_{\mathbf{n}_\alpha}^{\mathbf{m}_\alpha}(\theta,\varphi) e^{i\omega t} + (-1)^{m_\alpha} \overline{{\Phi^{(T)}}_{n_\alpha}^{m_\alpha,-}} \mathbf{Y}_{\mathbf{n}_\alpha}^{-\mathbf{m}_\alpha}(\theta,\varphi) e^{-i\omega t} \tag{4.13}$$

The forcing is real hence in the Fourier domain there is a $+\omega$ and $-\omega$ component of the forcing and $\overline{{\Phi^{(T)}}_{n_\alpha}^{m_\alpha,-}}$ corresponds to the complex conjugate of the amplitude. With the assumptions made for Ganymede of only considering eccentricity tides, the tidal forcing becomes:

$$\Phi^T(r,\theta,\varphi,t) = ({\Phi^{(T)}}_2^{0,+} \mathbf{Y_2^0}(\theta,\varphi) + \mathbf{\Phi^{(T)}}_2^{2,+} \mathbf{Y_2^2}(\theta,\varphi) + \mathbf{\Phi^{(T)}}_2^{-2,+} \mathbf{Y_2^{-2}}(\theta,\varphi)) e^{i\omega t} + c.c. \tag{4.14}$$

where only the degree 2 spherical harmonic terms (2,0), (2,2) and (2,-2) appear. The amplitudes of each component respectively are:

- ${\Phi^{(T)}}_2^{0,+} = \frac{3}{4}\sqrt{\frac{1}{5}} e (\omega R)^2$

- $\Phi^{(T)}{}_2^{2,+} = \frac{1}{8}\sqrt{\frac{6}{5}}e(\omega R)^2$
- $\Phi^{(T)}{}_2^{-2,+} = -\frac{7}{8}\sqrt{\frac{6}{5}}e(\omega R)^2$

In LOV3D, the tidal response is computed at one specific degree and order and the amplitude of forcing is normalized to a unit forcing (Rovira-Navarro et al. 2024).

The tidal response leads to a perturbation of the gravitational field of Ganymede as described in Section 2.2. This perturbation is described by the gravitational Love numbers. The tidal response of Ganymede, specifically the change in its gravitational field can be written in terms of extended Love numbers as:

$$\Phi = \sum_{n_\alpha, m_\alpha} \sum_{n_\beta, m_\beta} (\delta_{n_\alpha}^{n_\beta} \delta_{m_\alpha}^{m_\beta} + k_{n_\alpha, m_\alpha}^{n_\beta, m_\beta}) \Phi^{(T)}{}_{n_\alpha}^{m_\alpha} Y_{n_\beta}^{m_\beta} e^{i\omega t} + c.c. \tag{4.15}$$

This is a subset of the solution presented in Equation 4.10. To obtain the gravitational Love numbers, the forcing potential of Equation 4.14 can be substituted into Equation 4.15. It is important to note that everything up to this point, as well as the output of LOV3D, is in the Fourier domain and thus the gravitational Love numbers $k_{n_\alpha, m_\alpha}^{n_\beta, m_\beta}$ are complex numbers.

The interpretation of spacecraft observations, such as the determining the gravity field or estimating Love numbers, typically involves the use of real spherical harmonics and real Love numbers, as these directly relate to physical quantities and are easier to interpret. The complex spherical harmonics and complex Love numbers used in LOV3D can be transformed to their real counterpart. The following notation will be used to differentiate between real and complex numbers: $\mathcal{K}, \mathcal{Y}$ for real valued variables and k, Y for the complex numbers.

The complex spherical harmonic functions are:

$$Y_n^m(\theta, \varphi) = \sqrt{\frac{(2n+1)(n-m)!}{(n+m)!}} P_n^m(cos\theta) e^{im\varphi} \tag{4.16}$$

P_n^m are the associated Legendre functions that are normalized by the square-root term (normalization factor N_n^m). The real valued spherical harmonic functions are split into cosine (positive order $+m$) and sine terms (negative order $-m$) and are defined as (Qin et al. 2014):

$$\mathcal{Y}_n^m = \begin{cases} \sqrt{2}\bar{P}_n^m(\cos\theta)\cos m\varphi & \text{if } m > 0 \\ \bar{P}_n^m(\cos\theta) & \text{if } m = 0 \\ \sqrt{2}\bar{P}_{|n|}^m(\cos\theta)\sin|m|\varphi & \text{if } m < 0 \end{cases} \tag{4.17}$$

where $\bar{P}_n^m$ are the normalized associated Legendre functions. Both complex and real spherical harmonics are related by the following expression:

$$\mathcal{Y}_n^m = \begin{cases} \frac{1}{\sqrt{2}}(Y_n^m + (-1)^m Y_n^{-m}) & \text{if } m > 0 \\ Y_n^0 & \text{if } m = 0 \\ -\frac{i}{\sqrt{2}}(Y_n^m + (-1)^m Y_n^{-m}) & \text{if } m < 0 \end{cases} \tag{4.18}$$

The relationship between complex and real Love numbers is derived from the transformation of complex to real spherical harmonics, introducing a factor of $\sqrt{2}$ in some cases:

$$\mathcal{K}^{nm}_{n_\alpha m_\alpha} = \begin{cases} k^{n0}_{n_\alpha 0} \text{ if } m_\alpha = 0, m = 0 \\ \sqrt{2}\Re(k^{nm}_{n_\alpha 0}) \text{ if } m_\alpha = 0, m > 0 \\ -\sqrt{2}\Im(k^{n|m|}_{n_\alpha 0}) \text{ if } m_\alpha = 0, m < 0 \\ \sqrt{2}\Re(k^{n0}_{n_\alpha m_\alpha}) \text{ if } m_\alpha > 0, m = 0 \\ -\sqrt{2}\Im(k^{n0}_{n_\alpha |m_\alpha|}) \text{ if } m_\alpha < 0, m = 0 \\ \Re(k^{n|m|}_{n_\alpha |m_\alpha|}) + \text{sign}(m_\alpha)(-1)^m \Re(k^{n-|m|}_{n_\alpha |m_\alpha|}) \text{ if } \text{sign}(m_\alpha)\text{sign}(m) > 0 \\ -\text{sign}(m_\alpha)\Im(k^{n|m|}_{n_\alpha |m_\alpha|}) + (-1)^m \Im(k^{n-|m|}_{n_\alpha |m_\alpha|}) \text{ if } \text{sign}(m_\alpha)\text{sign}(m) < 0 \end{cases} \tag{4.19a}$$

All results obtained in this study are presented as real Love numbers and the notation k is adopted hereafter for convenience. The tidal response of a spherically-symmetric Ganymede is calculated using the reference model described in Table 4.2, and the results are summarized in Table 4.3. The obtained Love number $k_2 = 0.469$ corresponds to a degree 2 forcing signal and aligns with the expected range reported in literature ($k_2 = 0.3 - 0.6$) (Moore and Schubert 2003; Vance et al. 2018), while the value of $h_2 = 1.137$ falls within $h_2 = 1.1 - 1.6$ (Steinbrügge et al. 2015; Vance et al. 2018). The degree 3 gravitational Love number is also provided and will later be used to explore the impact of higher-order tidal forcings. While the magnitudes of Love numbers reported in literature varies significantly, the precise value obtained from this reference Ganymede model is less critical for the sensitivity analysis.

Table 4.3: Tidal response of a spherically-symmetric Ganymede based on reference interior model in Table 4.2. Radial points per layer = 400.

Parameter	Result
k_2	0.469
k_3	0.281
h_2	1.317

Introducing lateral variations into the interior model, results in a more complex tidal response, as described in Subsection 4.2.2. To demonstrate this effect, a near-side/far-side dichotomy in the ice shell will be introduced, corresponding to degree and order (1,1). The peak-to-peak amplitude of thickness variations is set to 10% and a tidal forcing of (2,0) is applied.

Figure 4.3 illustrates the different response patterns obtained for this example, following the selection rules shown in Figure 4.2. The response patterns in Figure 4.3 are shown as a Mollweide projection over the complete surface of Ganymede for a certain degree/order, highlighting positive and negative amplitude in red and blue respectively. Row 1 of Figure 4.3 illustrates a tidal forcing of degree (2,0) combined with a dichotomy of degree (1,1) in the ice shell thickness. The interaction between these components results in tidal responses at degree and order (1,1) and (3,1) with perturbation order 1, as shown in row 2. Second-order coupling generates four additional responses at (2,0), (2,2), (4,0), and (4,2), depicted in the final row.

Table 4.4 contains the magnitudes of all computed extended Love numbers for this example, above the numerical accuracy of LOV3D (see Section 4.3) and cut off at perturbation order 3. The magnitude of responses allows to see which responses are the most dominant in this case. Not shown in the figure are three third-order solutions arising: (3,3), (5,1) and (5,3). Note that the (1,1) first order solution is not significant enough to be considered above the chosen accuracy of 10^{-10}.

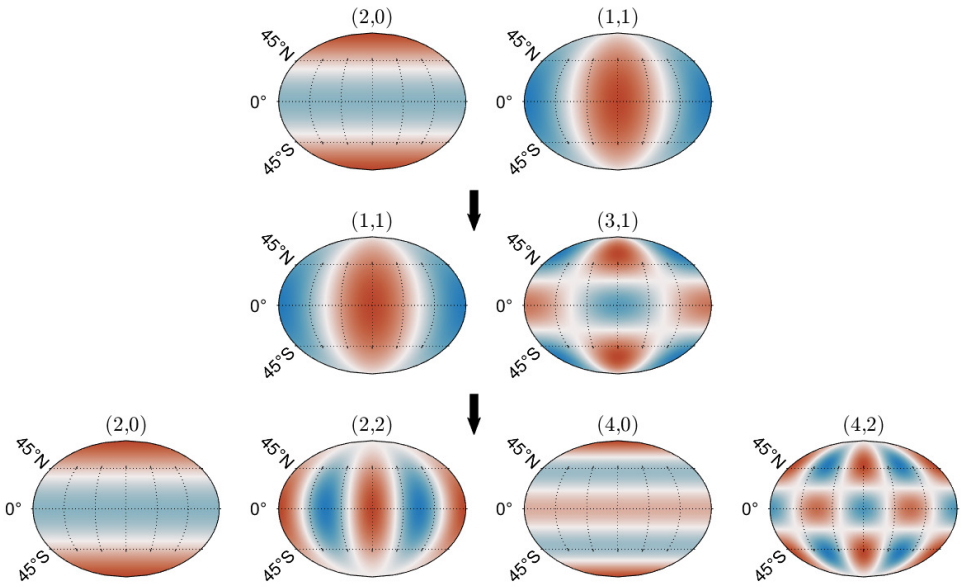

Figure 4.3: Visual representation of the most dominant tidal responses and resulting spherical harmonic patterns obtained for a forcing of (2,0) and lateral variations in the ice shell of Ganymede of (1,1). 1st order response modes are shown in row 2 and 2nd order response modes in row 3.

Table 4.4: Tidal response of Ganymede with (1,1) lateral variations in the ice shell due to a forcing of (2,0). Reference interior model taken from Table 4.2, $N_r = 400$, maximum perturbation order = 3. Only results above numerical accuracy shown.

Parameter	Result	Perturbation order
$k_{2,0}^{2,0}$	0.469	2
$k_{2,0}^{2,2}$	2.000×10^{-5}	2
$k_{2,0}^{3,1}$	-6.421×10^{-4}	1
$k_{2,0}^{3,3}$	-1.342×10^{-7}	3
$k_{2,0}^{4,0}$	-9.166×10^{-7}	2
$k_{2,0}^{4,2}$	1.025×10^{-6}	2
$k_{2,0}^{5,1}$	3.200×10^{-9}	3
$k_{2,0}^{5,3}$	-2.300×10^{-9}	3

The Love number $k_{2,0}^{2,0}$ deserves special attention, since it contains two tidal response effects. All other responses represent additional tidal signals that would not have been present in case of a spherically-symmetric interior. For $k_{2,0}^{2,0}$, the response wavelength matches the forcing wavelength and this response incorporates the spherically symmetric Love number k_2, which would arise in the absence of lateral variations, as well as an additional tidal signal due to second-order coupling. Notably, row 2 of Figure 4.3 contains the forcing pattern (2,0) again. In Table 4.4, the additional tidal signal $k_{2,0}^{2,0}$ is masked by the value of k_2 on top of it.

For the sensitivity study, only the additional tidal signals are of interest. Therefore the effect of the reference model, not including lateral variations (k_2), should be subtracted from the results. In this

example, the additional tidal signal $\Delta k_{2,0}^{2,0}$ is obtained by subtracting the standard Love number (k_2), without lateral variations, from the extended Love number $k_{2,0}^{2,0}$.

In general, for any forcing wavelength the additional tidal signal can be defined by ($\Delta k_{n_\alpha,m_\alpha}^{n_\beta,m_\beta}$) and for the case that the forcing wavelength (n_α, m_α) equals the response wavelength (n_β, m_β) the uniform Love number of the spherically-symmetric result needs to be subtracted. This applies equally for any forcing degree considered:

$$\Delta k_{n_\alpha,m_\alpha}^{n_\beta,m_\beta} = \begin{cases} k_{n_\alpha,m_\alpha}^{n_\beta,m_\beta} & \text{if } (n_\alpha, m_\alpha) \neq (n_\beta, m_\beta) \\ k_{n_\alpha,m_\alpha}^{n_\beta,m_\beta} - k_{n_\alpha}^{U} & \text{if } (n_\alpha, m_\alpha) = (n_\beta, m_\beta) \end{cases} \tag{4.20}$$

To assess the magnitude of the additional tidal signals, it is useful to normalize each additional tidal response ($\Delta k_{n_\alpha,m_\alpha}^{n_\beta,m_\beta}$) by the tidal response of the spherically-symmetric case ($k_{n_\alpha}^{U}$). The result describes the additional signal as percentage of the standard uniform Love number.

The sensitivity study examines which additional tidal signals arise from lateral variations in Ganymede and how they relate to Ganymede's interior by exploring several key factors. This includes the effect of the amplitude of lateral variations, the specific layer in which these variations are applied, the wavelength of the variations in terms of spherical harmonics, the impact of lateral variations occurring in multiple layers, and the overlaying effects of these variations and lastly the forcing wavelength. Each of these aspects is analyzed to understand their influence on the tidal response and the resulting Love numbers. The parameters investigated are summarized in table 4.5.

Table 4.5: Overview of methods and parameters investigated for sensitivity study of tidal signals to interior of Ganymede

Parameter	**Description**
Amplitude of lateral variations	Magnitude (%) of peak-to-peak variations
Layer of application	The specific interior layer affected
Wavelength of lateral variations	Spatial scale of the variations (degree/order)
Multiple-layer variations	Effects of variations in multiple layers and combined impact
Wavelength of tidal forcing	Degree and order of tidal forcing and resulting response

4.3. Verification

The sensitivity study was performed with the results from the software LOV3D and thorough verification is important before interpreting the results and making conclusions. This section contains a verification of the numerical accuracy of the code, after which the general model verification is shown with the results obtained by the authors. Lastly, the correct functioning of the liquid ocean layer is verified.

To compute the tidal response, the software discretises each layer into a number of radial points (N_r). The number of radial points per layer is a setting for the user to choose. The numerical accuracy of the software should increase with increasing N_r, up to a point where the accuracy is not limited by the level of discretisation and further refinement does not lead to better results. To check this, the reference model of Ganymede is used to repeatedly compute k_2 (see Table 4.3) for a wide range of N_r. The resulting change in k_2 per iteration is computed as difference: (eg. $\Delta k_2 = k_2(Nr = 400) - k_2(Nr = 200)$. The change in the computed Love number k_2 against the number of radial points is shown in Figure 4.4.

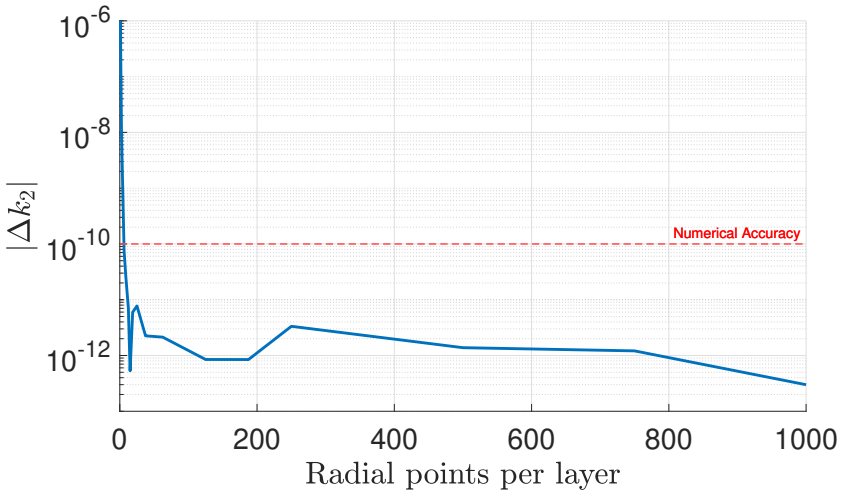

Figure 4.4: Change in subsequent k_2 values for decreasing the number of radial points per layer. The chosen numerical accuracy level of 10^{-10} is indicated in red.

Figure 4.4 shows that the value of k_2 changes with depending on the number of radial points per layer chosen up to about $N_r = 200$. Further decreasing N_r does not lead to smaller changes in Δk_2 and the value fluctuates around 10×10^{-12}. Assuming the differences in subsequent computations are a good measure for the discretisation error in solving the tidal response, this indicates two things: (1) Setting the number of radial points per layer to 200 or greater ensures that the results are not limited by truncation errors or inadequate discretisation. (2) The maximum numerical accuracy of LOV3D is approximately close to 10^{-11}, as beyond that point any further discretisation does not improve the computation of k_2. To maintain a conservative approach, any result obtained from LOV3D below an accuracy of 10^{-10} is likely attributed to numerical noise and should be excluded in the interpretation of the tidal response of Ganymede.

The accuracy of the software used for this study, LOV3D, has been verified by its authors in the original publication (Rovira-Navarro et al. 2024). The version of the software tested in that work was an earlier iteration, using a simplified interior structure consisting of a solid core, liquid layer and ice shell. To ensure the validity of their method, the authors compared their results with two alternative approaches: the spectral-perturbation method of (Qin et al. 2014) and the finite element method (FEM) model developed by (Berne et al. 2023; Berne et al. 2023). Figure 4.5 shows parts of the verification performed by the authors, where gravitational love numbers are computed for lateral variations in the top layer of degree and order (1,1). The amplitude (%) of shear modulus variation is varied and the difference between all three methods is seen in the lower panel.

Figure 4.5 shows that all three methods produce consistent results. The differences with respect to the perturbation method increase with higher amplitude lateral variations and reach up to 5 % for an amplitude of 50%. At large amplitudes the perturbation approach is not accurate as it requires the assumption of small lateral variations. The FEM method agrees best with the authors results and differences in both methods stay below 1% even for large amplitude variations. Remaining discrepancies in both methods are attributed to resolution-related errors. This analysis confirms that the software is accurate even for modeling high-amplitude lateral variations, although it lacks the capability of the FEM to simulate complex interior structures, such as cracks or faults within the ice shell.

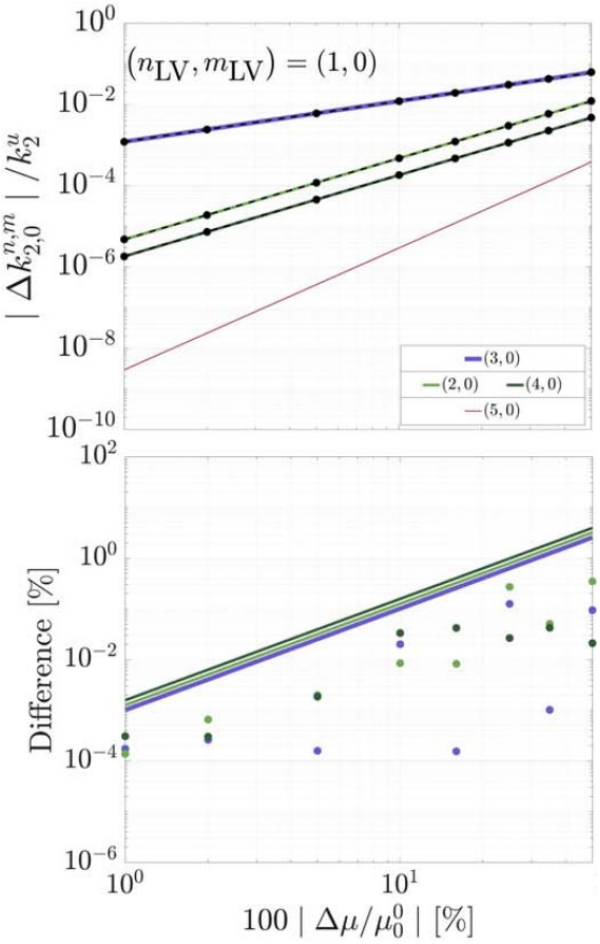

Figure 4.5: Verification of the LOV3D software as presented by authors in (Rovira-Navarro et al. 2024). Upper figure: Gravitational Love numbers obtained for lateral variations of (1,0) over a range of amplitudes (% of peak-to-peak shear modulus variations). Lower figure: differences in results between methods. Solid lines represent results obtained with LOV3D, dashed lines results from the perturbation method by (Qin et al. 2014), circles represent solutions obtained with FEM method (Berne et al. 2023; Berne et al. 2023).

An improved version of LOV3D allows to calculate lateral variations in multiple layers and model liquid layers. The addition of the ocean layer has been tested for a spherically-symmetric body with success. The addition of multiple layers has been tested against the perturbation method of (Qin et al. 2014). The correct functioning of the sub-surface ocean layer is checked by comparing results of two models. In one model, the ocean layer is defined using the new functionality and in the other model the ocean layer is simulated by defining a low shear modulus for that layer ($\mu = 100\,GPa$). A liquid layer essentially has a shear modulus of zero as it does not resist any deformation and thus both models should produce equivalent results. Figure 4.6a and 4.6b show the resulting gravitational Love numbers due to lateral variations (1,1) in the ice shell caused by a forcing of (2,0). The results agree except for the (2,0) response, which deviates from the ocean layer model at lower amplitudes (< 1%) of shear modulus variations applied. These differences can be explained by low values of μ causing numerical issues.

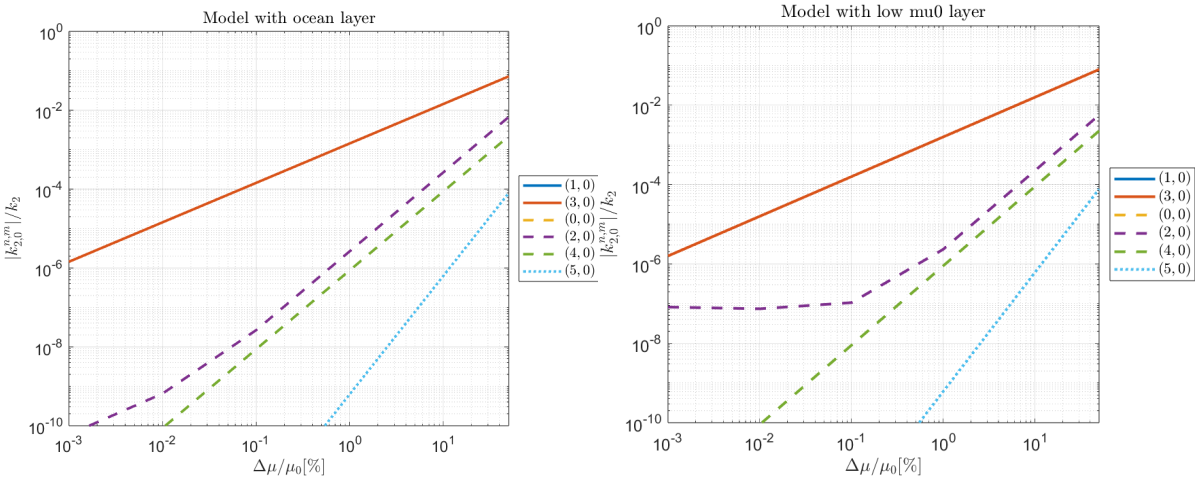

(a) Ocean layer

(b) Very low shear modulus layer

Figure 4.6: Gravitational Love numbers obtained for a Ganymede model with (a) an ocean layer and (b) using a very low shear modulus layer. Lateral variations (1, 1) in the ice shell are applied over a range of amplitudes due to a forcing at (2,0).

4.4. Results

The results of the sensitivity analysis are presented in this section, focusing on the additional tidal signals generated by lateral variations in Ganymede's interior structure. A large parameter space is explored, since the actual interior of Ganymede is poorly constrained. The primary aim is to quantify the effects of varying the amplitude, wavelength, and location of lateral variations, as well as the combined effects of multiple layers and forcing wavelengths. The amplitude of lateral variations and the effect on the tidal response is discussed in Subsection 4.4.1. Subsection 4.4.2 studies the effect of different forcing wavelengths, while the location of lateral variations and the sensitivity to the deep interior is explored in Subsection 4.4.3. Different types of lateral variations and the resulting tidal spectra are analyzed in Subsection 4.4.4 and Subsection 4.4.5 shows the amplitude of the leading tidal response modes and compares them to the uncertainty obtained in the covariance analysis.

The reference Ganymede model described in Table 4.2 is the baseline for all results and the gravitational Love numbers are obtained assuming a fully elastic incompressible interior. The additional tidal signals ($\Delta k^{n,m}_{n_\alpha,m_\alpha}$) are presented as real Love numbers with the uniform Love number removed from the response as outlined in Section 4.2. The maximum perturbation order considered is 3 and all results below 1×10^{-10} are neglected.

4.4.1. Amplitude of Lateral Variations

In the first step, the impact of amplitude of lateral variations in Ganymede's ice shell is explored in response to a tidal forcing of degree and order (2,0). Lateral variations of (1,1) are introduced and the resulting additional tidal signals ($\Delta k^{n,m}_{2,0}$) arising due to the presence of lateral variations are computed over a range of amplitudes. Figure 4.7b shows the percentage change of peak-to-peak shear modulus variations present in the ice shell with respect to its mean value ($\Delta\mu/\mu_0$) along the x-axis. Since this is equivalent to a change in thickness, this can be understood as the amplitude in % of thickness variations in the ice shell.

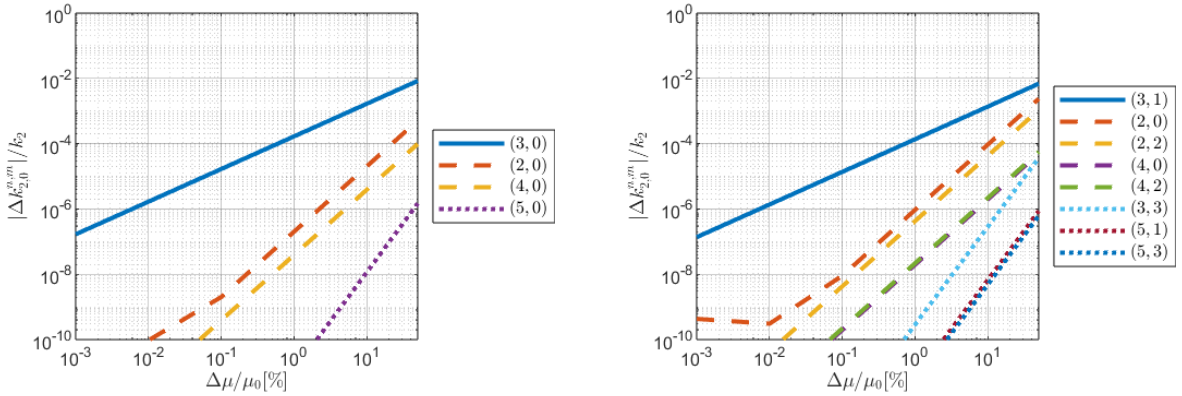

(a) Lateral variations (1,0) in the ice shell

(b) Lateral variations (1,1) in the ice shell

Figure 4.7: Additional tidal signals ($\Delta k_{2,0}^{n,m}$) obtained due to the presence of lateral variations in Ganymede's ice shell. Results shown as a function of the amplitude of lateral variations (% peak-to-peak variation) induced by tidal forcing of (2,0). Interior parameters found in Tab. 4.2, max. perturbation order is 3 and $n_r = 400$.

The results presented in Figure 4.7b correspond to lateral variations of (1,1) and align with the example shown in Table 4.4, discussed earlier in the methodology Section 4.2. These results were obtained under the assumption of having 10% variations in ice shell thickness, and the associated tidal response patterns for perturbation orders 1 and 2 were visualized in Figure 4.3. Figures 4.7a, 4.8a, and 4.8b present analogous results for different degrees and orders of lateral variations in the ice shell, specifically (1,0), (2,0), and (3,3).

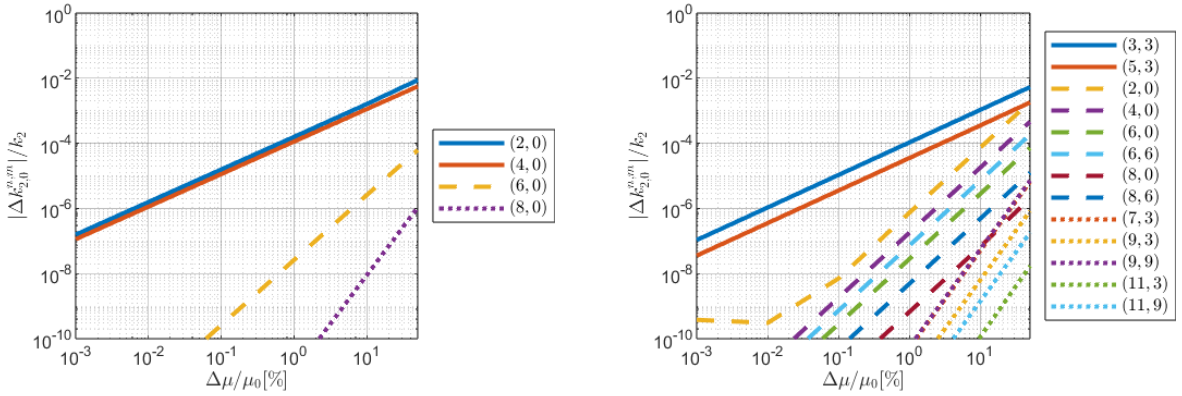

(a) Lateral variations (2,0) in the ice shell

(b) Lateral variations (3,3) in the ice shell

Figure 4.8: Additional tidal signals ($\Delta k_{2,0}^{n,m}$) obtained due to the presence of lateral variations in Ganymede's ice shell. Results shown as a function of the amplitude of lateral variations (% peak-to-peak variation) induced by tidal forcing of (2,0). Interior parameters found in Tab. 4.2, max. perturbation order is 3 and $n_r = 400$.

Several observations can be made from these results. The presence of lateral variations generates multiple additional tidal signals in addition to the spherically symmetric response, appearing not only at the forcing wavelength but also at additional wavelengths, as previously discussed. The magnitude of these additional tidal responses increases significantly with the amplitude of lateral variations applied, highlighting that the amplitude is a key factor driving these responses. The Love nubmers are highly sensitive to changes in amplitude, whereas the specific pattern of lateral variations (degree and order) plays a comparatively smaller role in influencing the overall response.

The order of perturbation is also linked to the strength of the tidal signal. As seen in Figures 4.7a-4.8b, first-order perturbation modes consistently produce the largest signals, followed by second-order modes and then third order modes. In the plots, the perturbation orders are visually distinguished by the use of solid lines for first-order modes, dashed lines for second-order modes, and dotted lines for third-order modes. At very large amplitudes, exceeding around 20%, this effect vanishes and also higher order

modes can become dominant. Higher-order perturbation modes display steeper curves, indicating that they are more sensitive to changes in the amplitude of lateral variations.

As expected and part of verification, the tidal response diminishes as the amplitude of lateral variations approaches zero, confirming that no additional response is present in the absence of variations. When the spherical harmonic pattern of lateral variations has an order of 0, the responses are likewise restricted to order 0, due to the forcing being at (2,0). Furthermore, as the degree and order of lateral variations increase representing more complex spatial thickness variation patterns more response modes are excited. The highest significant response wavelength for lateral variations of (1,0) is (5,0) while for lateral variations of (3,3) there are also responses at degree 11. It can be observed that the higher the degree and order of response wavelength is, the lower will be its signal and corresponding gravitational Love number.

Interestingly, the overall order of magnitude of the responses remains relatively consistent regardless of the degree and order of lateral variations applied. By way of example, the magnitude of additional signals can reach as high as 1×10^{-4} of the spherically symmetric signal k_2, assuming an amplitude of 1%. In contrast, second-order response modes appear at magnitudes between 1×10^{-6} to 1×10^{-8} of the k_2 signal. Third-order response modes, such as those arising from lateral variations of (3,3), require thickness variations exceeding 10% amplitude to produce response magnitudes greater than 1×10^{-10}, as evident in Figure 4.8b. A maximum of 50% was computed during the sensitivity analysis as values above this are not considered realistic, taking into account current knowledge about the ice shells of Enceladus and Europa, see Figure 2.3.

4.4.2. Impact of Tidal Forcing Wavelength

The impact of the forcing wavelength is explored next, where the forcing (2,2) is the second contribution, next to (2,0), arising from eccentricity tides on Ganymede. Figures 4.9a and 4.9b show the additional tidal signals ($\Delta k_{2,2}^{n,m}$) obtained for lateral variations in the ice shell of (1,1) and (3,3) respectively.

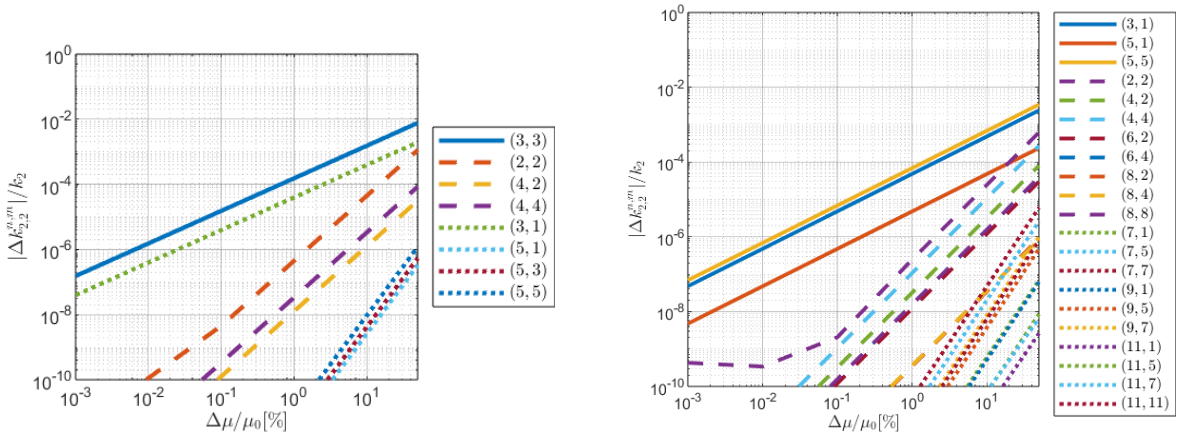

(a) Lateral variations (1,1) in the ice shell

(b) Lateral variations (3,3) in the ice shell

Figure 4.9: Additional tidal signals ($\Delta k_{2,2}^{n,m}$) obtained due to the presence of lateral variations in Ganymede's ice shell. Results shown as a function of the amplitude of lateral variations (% peak-to-peak variation) induced by tidal forcing of (2,2). Interior parameters found in Tab. 4.2, max. perturbation order is 3 and $n_r = 400$.

When comparing the effects of the (2,0) and (2,2) tidal forcing, it becomes evident that the overall magnitude of the resulting tidal signals is similar, even though distinct response modes are excited depending on the nature of the forcing. With 1% thickness variations in the shell, the maximum additional signals reach approximately 1×10^{-4} of the k_2 value in both cases. As illustrated in Figures 4.7b and 4.9a, different tidal response modes emerge, aligning directly with the selection rules presented in Figure 4.2.

Considering this example and checking the selection rules shown in Figure 4.2, it can be seen that a (1,1) response is predicted from first order coupling of the forcing and lateral variation wavelength. However,

the first-order response (1,1) does not produce a significant tidal signal in either forcing case. Instead, the dominant modes differ between the two forcings: for (2,0) forcing, the largest response comes from the (3,1) mode, while for (2,2) forcing, the strongest signals arise from the (3,1) and (3,3) modes. Among the second-order coupling responses, the self-coupling modes, ie. the (2,0) response due to a (2,0) forcing and (2,2) response due to (2,2) forcing, stand out. These modes exhibit the largest magnitudes among second-order responses, exceeding other second-order signals by an order of magnitude.

In this sensitivity analysis, the two forcing wavelengths have been considered separate and their tidal response can be computed independently. In reality, the two forcings contributions act simultaneously and equal response modes combine together. For lateral variations of (1,1), as illustrated in Figures 4.7b and 4.9a, the responses (2,2) and (4,2) appear for both forcing cases, albeit with differing magnitudes. From a measurement perspective, the measured gravitational signal at response (2,2) is likely to include contributions from several forcing wavelengths. This leads to the introduction of effective Love numbers, which provide a framework to describe the combined tidal responses felt by a spacecraft. These effective Love numbers are crucial for interpreting time-varying gravity field measurements and are explained in detail in the covariance analysis presented in Chapter 3.

Additionally, toroidal modes are also excited as part of the response. However, these modes are not considered here, as they do not contribute to the gravitational Love number responses. Notably, a first-order toroidal mode, such as (2,-1), can couple with the forcing to produce a second-order spheroidal mode, as indicated in Figure 4.2.

4.4.3. Location of Lateral Variations

To explore the sensitivity of tidal responses to the location of lateral variations within Ganymede, the analysis is extended by repeating the results from Figure 4.7b for lateral variations of (1,1) in response to a (2,0) forcing, applied to different internal layers. Figures 4.10a and 4.10b illustrate the outcomes when lateral variations are located in the high-pressure ice layer and the mantle, respectively.

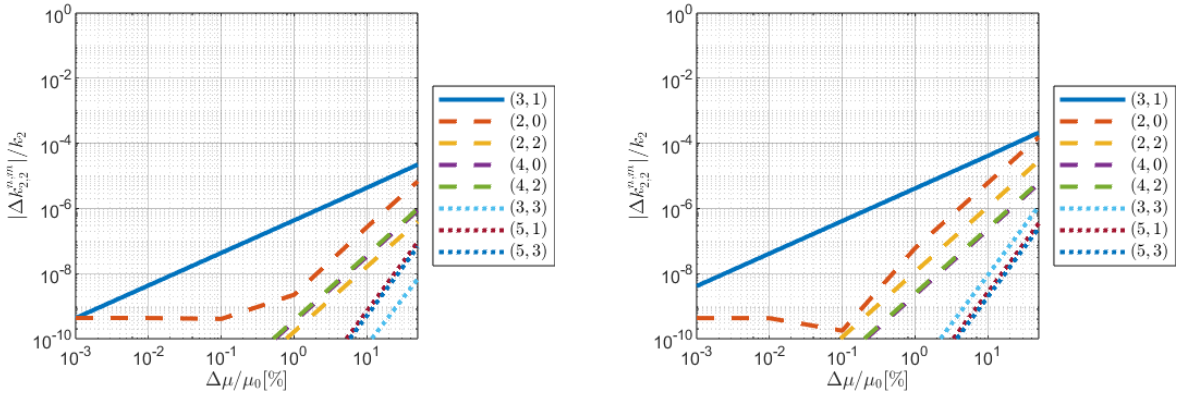

(a) Lateral variations (1,1) in the high-pressure ice layer

(b) Lateral variations (1,1) in the mantle layer

Figure 4.10: Additional tidal signals ($\Delta k_{2,0}^{n,m}$) obtained due to the presence of lateral variations (1,1). Results shown as a function of the amplitude of lateral variations (% peak-to-peak variation) induced by tidal forcing of (2,0). Interior parameters found in Tab. 4.2, max. perturbation order is 3 and $n_r = 400$.

The results reveal significantly lower additional tidal signals in both cases compared to when the lateral variations are located in the ice shell. Specifically, the magnitudes of these signals are approximately one order of magnitude lower when variations occur in the mantle and two orders of magnitude lower when they arise in the HP ice layer. For thickness variations with an amplitude of 10%, the maximum tidal signals are approximately 6×10^{-4} of of k_2 for the ice shell, 2×10^{-5} of of k_2 for the mantle, and 2×10^{-6} of of k_2 for the high pressure ice layer.

In the case of the high pressure ice layer, the dominance of certain response modes shifts, with the (2,2) response becoming less significant compared to the (4,0) and (4,2) modes. These findings underscore the high sensitivity of gravitational Love numbers to lateral variations in the ice shell, while variations

deeper in the interior have a much smaller impact. Although the high pressure ice layer is closer to the surface, the mantle layer spans over 1000 km and thus variations in its thickness have a larger influence than the high pressure ice layer does.

From a practical perspective, any observed tidal signal could theoretically stem from lateral variations in the mantle or ice shell. It is most likely, that they can be attributable to variations in the ice shell however, as significantly smaller amplitudes of lateral variations are sufficient to produce the same response. To examine the combined impact of lateral variations in both the mantle and ice shell, two scenarios are analyzed: (I) lateral variations of degree and order (2,0) and (II) lateral variations of (1,0), both under a (2,0) forcing. In each case, the most dominant additional tidal signal is studied, as this signal is the most likely to be detectable by the JUICE spacecraft. For the (2,0) lateral variation, the dominant signal is the (2,0) response, while for the (1,0) variation, the dominant signal is the (3,0) response. These signals are analyzed over a wide range of amplitudes of thickness variations in both layers.

The combined effect of having lateral variations in the ice shell and mantle on the largest tidal response are presented in Figures 4.11a and 4.11b for case I and II respectively. The contour lines show which combination of thickness variations in the ice shell and mantle lead to the same signal strength.

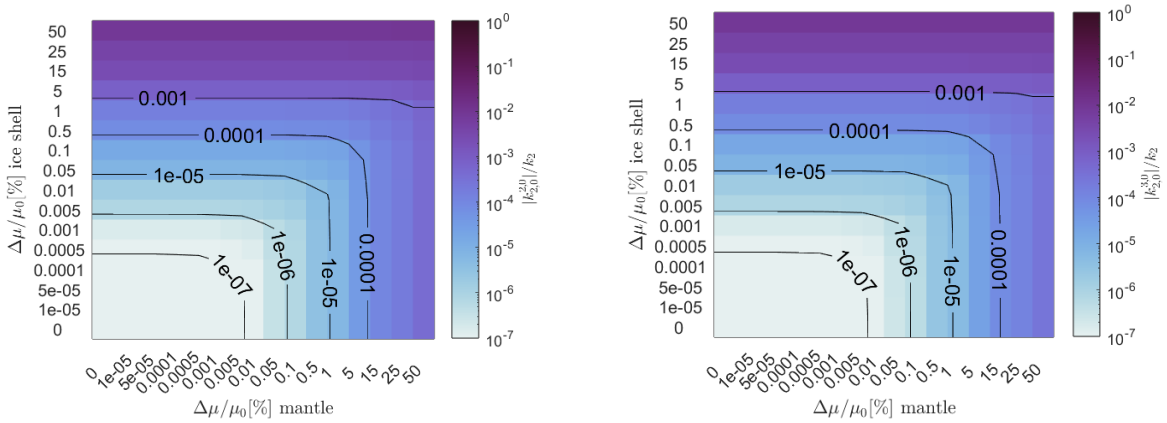

(a) Magnitude of largest response ($\Delta k^{2,0}_{2,0}$) for lateral variations (2,0).

(b) Magnitude of largest response ($\Delta k^{3,0}_{2,0}$) for lateral variations (1,0).

Figure 4.11: Combined effect of lateral variations in Ganymede's mantle and ice shell due to a forcing at (2,0). The x-axis represents the amplitude of lateral variations in the mantle, while the y-axis represents the amplitude of lateral variations in the ice shell. The magnitude of the largest tidal signal for each case is shown on the color plot with with contour lines added to highlight regions of equal signal magnitude. Interior parameters found in Tab. 4.2, max. perturbation order is 3 and $n_r = 400$.

As seen in Figure 4.11a, an additional tidal signal $\Delta k^{2,0}_{2,0}$ with a magnitude of 1×10^{-5} of k_2 is obtained for either 2% mantle thickness variations or 0.05% shell thickness variations. When the ice shell exhibits lateral variations, even small amplitudes (e.g., 0.1% in this example) dominate the tidal signal. As a result, the mantle variations, regardless of their magnitude, cannot produce a significant additional signal that overshadows the shell's influence. This leads to horizontal contour lines where the tidal signal is largely insensitive to mantle variations.

Conversely, when the mantle reaches a critical amplitude (e.g., 1% for this example), it dominates the response until the ice shell variations reach a minimum threshold (e.g., 0.1%) to become noticeable. This creates vertical contour lines where the mantle primarily drives the signal. The ice shell variations have a disproportionately higher impact on the tidal signal than the mantle, requiring far smaller amplitudes to produce equivalent effects as seen before. Any additional signal with a magnitude of 1×10^{-3} of the k_2 Love number, is completely insensitive to the amplitude of lateral variations in the mantle.

Given the sensitivity of the gravitational Love numbers is highest to the ice shell and the fact that the JUICE mission is expected to operate at the threshold of detecting any additional tidal signals, it is more practical to concentrate on ice shell variations for the remainder of the study. For a given tidal response, the largest responses arising would require an order of magnitude larger thickness variations in the mantle than explainable by an ice shell, making the focus on constraining the ice shell both more

feasible and realistic.

4.4.4. Wavelength of Lateral Variations

To investigate the impact of the degree and order of lateral variations in the ice shell on the tidal response, models were computed using 10% amplitude of lateral variations, ranging from degree and order (1,0) to (3,3). The resulting spectral plots are depicted in Figures 4.12 and 4.13, which present the complete tidal response spectra for forcing scenarios of (2,0) and (2,2), respectively.

The tidal spectra plots show that each type of lateral variation patterns produces a unique pattern of response modes. In these figures, the degree and order of the lateral variations in the ice shell are shown on the y-axis, while the degree and order of the resulting tidal response appear on the x-axis. Each row in the plot corresponds to a specific structure of lateral variations in the ice shell, with the corresponding tidal response magnitude indicated by the color scale. Each column reveals which types of lateral variations contribute to a specific tidal response wavelength, while the perturbation order of each solution can be identified by a cross (first order), circle (second order) or square (third order).

As the degree and order of lateral variations increase, the number of response modes also rise, while the magnitude of the tidal signals generally decreases with longer response wavelengths. Certain patterns stand out, for example in Figure 4.12, where vertical bars are visible at (2,0), (4,0), and (6,0). These correspond to second order responses which consistently appear as multiples of the forcing degree and order. These bars highlight the self-coupling effects of the forcing wavelength with itself, which produce the strongest second-order signals.

Additionally, Figure 4.12 reveals that most first-order responses align along two distinct diagonal lines. One of these lines corresponds to cases where there is self-coupling (response = forcing D/O). The other diagonal line shows an offset pattern that varies with the degree of the lateral variations in the ice shell. Specifically: a degree ice shell structure produces first-order responses at degree 3, a degree 2 structure produces first-order responses at degree 4 and a degree 3 structure produce first-order responses at degree 5. These patterns also show how the first order responses increase linearly with an increasing degree and order of lateral variation pattern applied, while the number of higher order responses grows much faster.

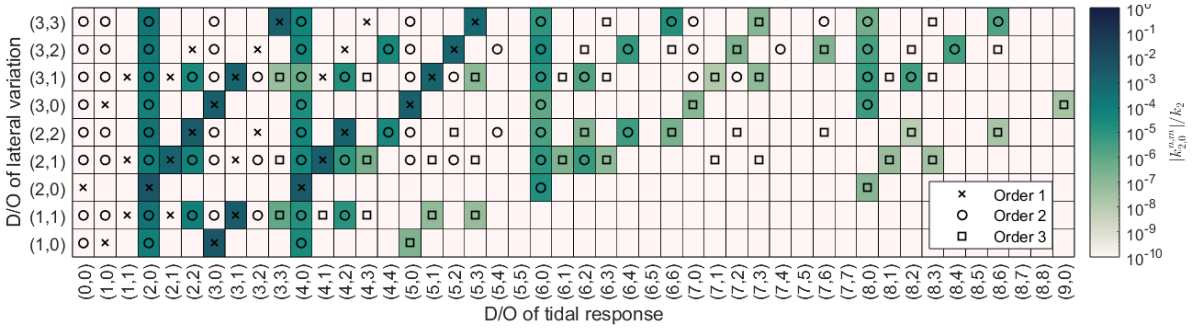

Figure 4.12: Tidal spectra induced by a forcing of (2,0) for degrees and orders of lateral variations in the ice shell at 10% amplitude. The colour scale shows the magnitude of the response obtained and the perturbation orders are identified with different markers. Interior parameters found in Tab. 4.2, max. perturbation order is 3 and $n_r = 400$.

The challenge of using tidal tomography to recover any information about lateral variations becomes clear when looking at the spectral plots. Although in theory each row has a unique set of responses, the responses found in the columns of Figures 4.12 and 4.13 are not unique, hence there are certain lateral variations that produce very similar results. Both a (1,1) structure and (3,1) structure induce the same type of tidal response. To distinguish them requires being able to observe the degree 7 responses that are unique to (3,1) or observing the degree 5 signals which are stronger in magnitude for the (3,1) response. Assuming that degree 3 signals could be measured, the spectral plots show that this allows to constrain the ice shell structure to degree 1 and degree 3.

Looking at Figure 4.12, for a forcing of (2,0), a response of (2,0) can originate from all types of lateral variations and does itself given not any information. The (2,2) response is excited by less degrees and

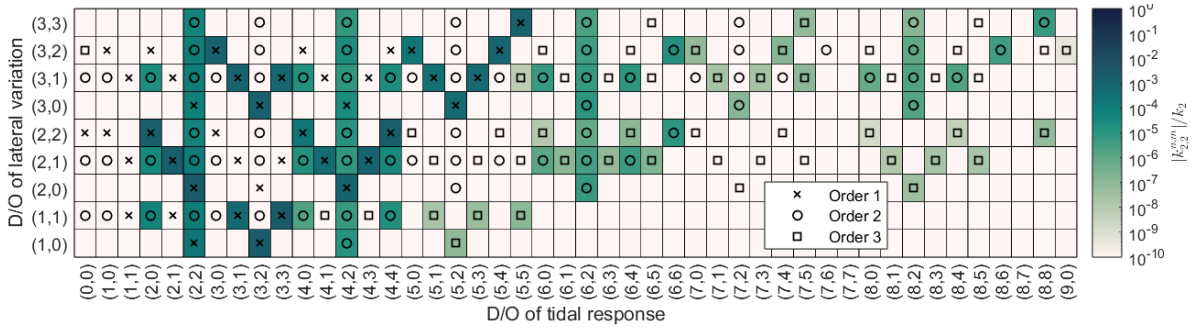

Figure 4.13: Tidal spectra induced by a forcing of (2,2) for different degrees and orders of lateral variations in the ice shell at 10% amplitude. The colour scale shows the magnitude of the response obtained and the perturbation orders are identified with different markers. Interior parameters found in Tab. 4.2, max. perturbation order is 3 and $n_r = 400$.

orders of lateral variations and thus distinguishing both could give information to constrain the ice shell in more detail. The tidal forcing of Ganymede has both (2,0) and (2,2) contributions present, thus the magnitudes of both spectral plots would combine. If the additional tidal signals created at orders 0 and 2 could be distinguished from the main response, this may allow to confirm the presence of lateral variations.

4.4.5. Comparison of Leading Mode Signals to JUICE Uncertainty

As JUICE is expected to be on the verge of observing any of these additional signals, which are relatively small in magnitude compared to the main response k_2, it is useful to focus on the most dominant signals. For each type of lateral variations, the largest amplitude signal and the corresponding response mode can be extracted from the tidal spectra plot. The maximum additional signals for each type of lateral variation in the ice shell are combined into a single plot for clarity. Figures 4.14 and 4.15 illustrate these maximum additional tidal signals for each lateral variation type under the two forcing scenarios: (2,0) and (2,2). The signals are presented over a range of amplitudes of variations in the ice shell. Lateral variations of degrees 1, 2, and 3 are represented by black, red, and blue lines, respectively, with solid lines corresponding to order = 0, dashed lines to order = 1, and so forth.

Figures 4.14 and 4.15 highlight the expected amplitudes of the leading tidal signals for various lateral variations in Ganymede's ice shell. It is evident that degree 1 and degree 2 lateral variations generate significantly larger signals compared to degree 3 variations. The largest tidal signals arising are the (2,0) and (3,0) response induced by a forcing of (2,0) and the (2,2) and (3,2) response induced by a forcing of (2,2). These signals correspond to the Love numbers $k_{2,0}^{2,0}$, $k_{2,2}^{2,2}$ and $k_{2,0}^{3,0}$, $k_{2,2}^{3,2}$, where the former two are produced by lateral variations of (1,0) and the latter two arise with lateral variations of type (2,0). For ice shell thickness variations between 1% and 10%, these additional tidal signals would have a magnitude of approximately 1×10^{-4} to 1×10^{-3}. Lateral variations of (1,0) and (2,0) produce the largest responses and these correspond to zonal (order = 0) variations in the ice shell, meaning no variations in longitude.

The covariance analysis in Chapter 3 showed that JUICE will be able to observe the degree 2 diagonal Love numbers with an uncertainty of $\sigma_{k_{2,0}^{2,0}} = 4.4 \cdot 10^{-4}$ and $\sigma_{k_{2,2}^{2,2}} = 2.05 \cdot 10^{-4}$. Higher order responses, such as the degree 3 responses arising from lateral variations of H_{10}, H_{20} were shown to have a accuracies around $\sigma_{k_{2,0}^{3,0}} = 4.17 \cdot 10^{-4}$ and $\sigma_{k_{2,2}^{3,2}} = 1.38 \cdot 10^{-4}$. To answer the research question, the expected uncertainty of JUICE observations, indicated by the horizontal lines in Figures 4.14 and 4.15, is compared with the corresponding leading mode tidal signals, resulting in a required amplitude of lateral variations at which these signals could be detected.

The $k_{2,0}^{2,0}$ and $k_{2,0}^{3,0}$ signals from a forcing at (2,0) require an amplitude of lateral variations of at least $\Delta H \approx 5\%$. Likewise the $k_{2,2}^{2,2}$ and $k_{2,2}^{3,2}$ signals shown in Figure 4.15 would be detectable at an amplitude of $\Delta H \approx 2 - 3\%$. These signals are largest in magnitude and given the obtained uncertainties of JUICE, would be most likely to observe. The covariance analysis also showed that JUICE would be sensitive to

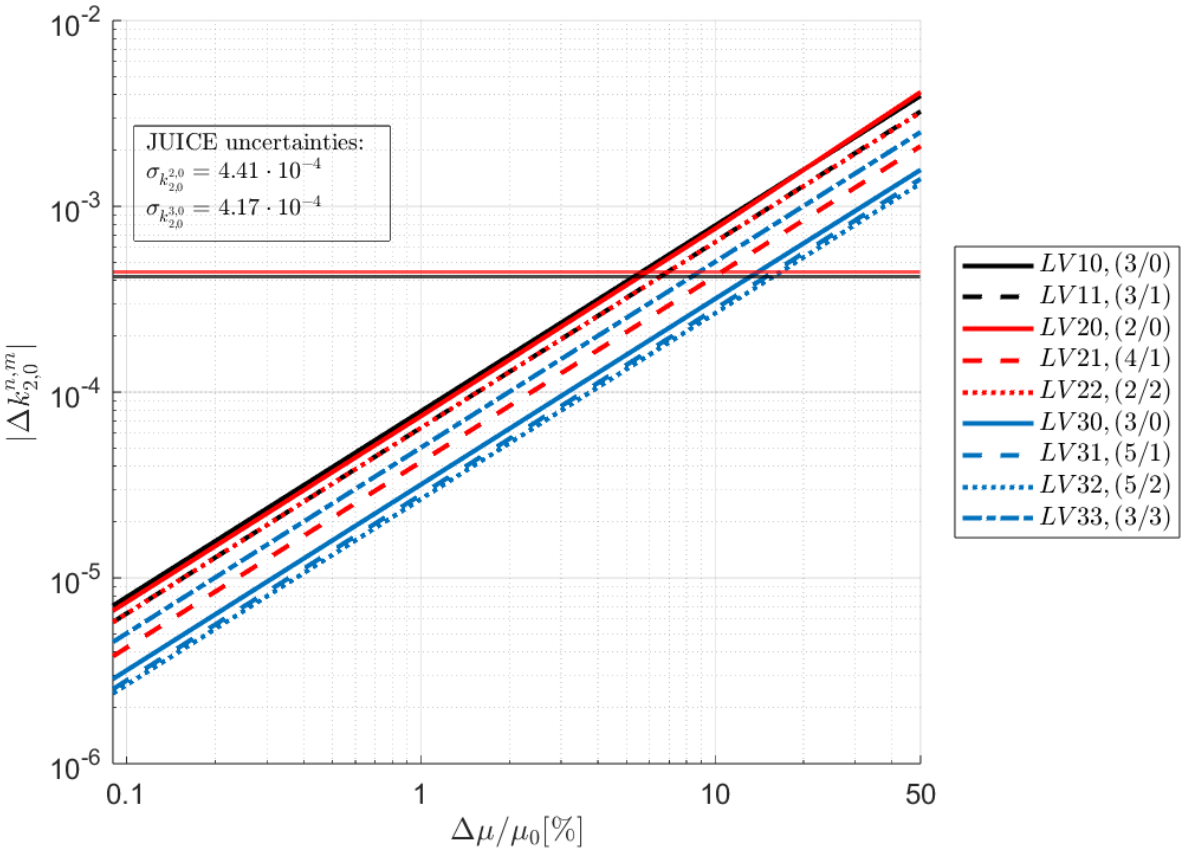

Figure 4.14: Largest additional tidal signals ($\Delta k_{2,0}^{n,m}$) obtained for different degree/order of lateral variations in Ganymede's ice shell. Uncertainties of k_{20}^{20} and k_{20}^{30} observations by JUICE are indicated with a horizontal lines. Results shown as a function of the amplitude of lateral variations (% peak-to-peak variation) induced by tidal forcing of (2,0). Interior parameters found in Tab. 4.2, max. perturbation order is 3 and $n_r = 400$.

higher order responses with similar magnitude as $\sigma_{k_{2,0}^{2,0}}$. The amplitude of lateral variations at which the additional signals in Figures 4.14 and 4.15 intersect this uncertainty are are provided in Table 4.6.

If these numbers are not too optimistic this implies that lateral variations of type (2,0), hence a flattening of the ice shell around the equator of Ganymede and (1,0), a polar dichotomy in the ice shell, could be detected if their amplitudes is at least $\Delta H \approx 5\%$. Higher order lateral variations that are not zonal but have a more complicated spatial structure would require a larger amplitude of thickness variations in the ice shell of roughly $\Delta H \approx 6 - 17\%$.

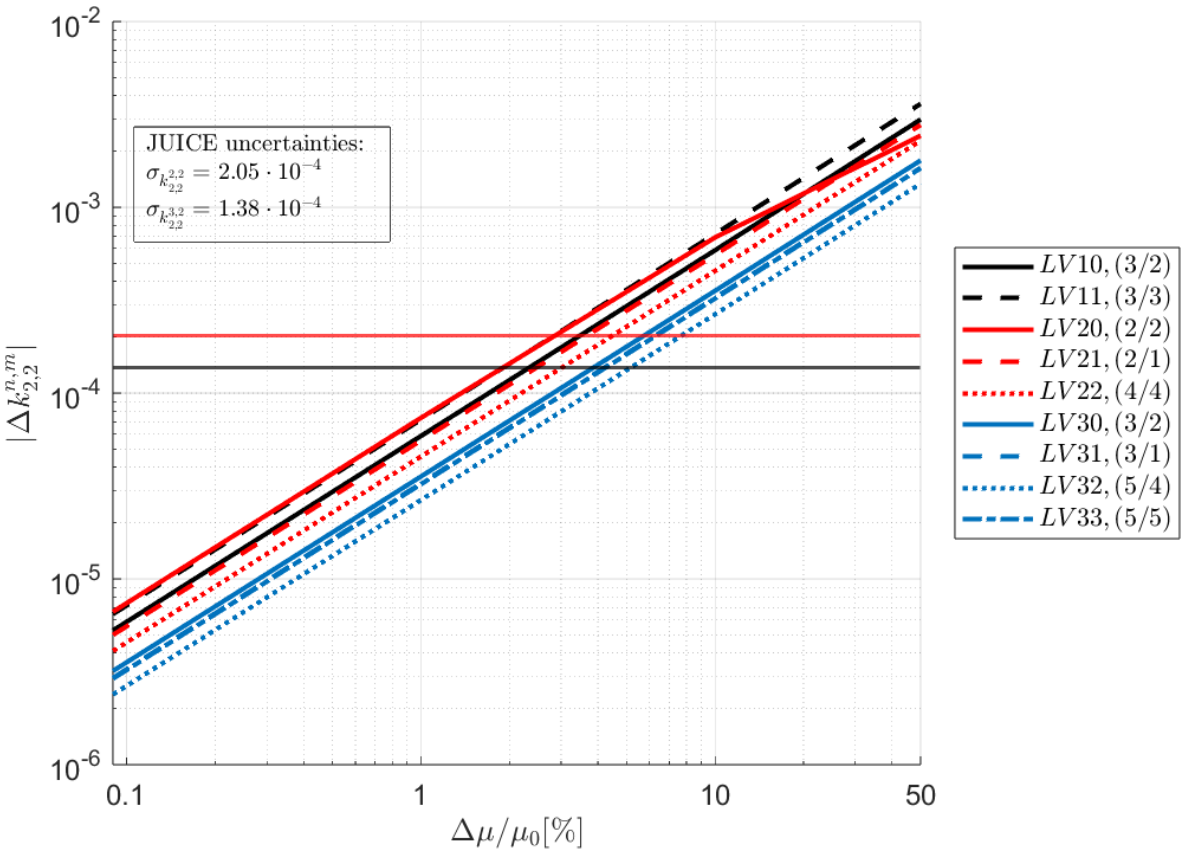

Figure 4.15: Largest additional tidal signals ($\Delta k_{2,2}^{n,m}$) obtained for different degree/order of lateral variations in Ganymede's ice shell. Uncertainties of k_{22}^{22} and k_{22}^{32} observations by JUICE are indicated with a horizontal lines. Results shown as a function of the amplitude of lateral variations (% peak-to-peak variation) induced by tidal forcing of (2,2. Interior parameters found in Tab. 4.2, max. perturbation order is 3 and $n_r = 400$.

Table 4.6: Comparison of tidal response signals for different lateral variation patterns in Ganymede's ice shell. Signal magnitudes are shown for a 1% amplitude of lateral variations, along with the required amplitude to achieve a detectable signal at $\sigma = 4.4 \cdot 10^{-4}$.

Lateral variations structure	Additional tidal signals Δk at 1% amplitude	Required amplitude ΔH for an uncertainty of $\sigma = 4.4e-4$
(1,0)	$\Delta k_{22}^{32} = 5.86 \times 10^{-5}, \Delta k_{20}^{30} = 7.86 \times 10^{-5}$	7.51, 5.60
(1,1)	$\Delta k_{22}^{33} = 7.18 \times 10^{-5}, \Delta k_{20}^{31} = 6.42 \times 10^{-5}$	6.13, 6.85
(2,0)	$\Delta k_{22}^{22} = 7.34 \times 10^{-5}, \Delta k_{20}^{20} = 7.41 \times 10^{-5}$	6.38, 5.82
(2,1)	$\Delta k_{22}^{21} = 5.54 \times 10^{-5}, \Delta k_{20}^{41} = 4.20 \times 10^{-5}$	7.94, 10.46
(2,2)	$\Delta k_{22}^{44} = 4.54 \times 10^{-5}, \Delta k_{20}^{22} = 6.40 \times 10^{-5}$	9.68, 6.87
(3,0)	$\Delta k_{22}^{32} = 3.55 \times 10^{-5}, \Delta k_{20}^{30} = 3.17 \times 10^{-5}$	12.34, 13.92
(3,1)	$\Delta k_{22}^{31} = 3.26 \times 10^{-5}, \Delta k_{20}^{31} = 2.82 \times 10^{-5}$	13.50, 15.70
(3,2)	$\Delta k_{22}^{54} = 2.65 \times 10^{-5}, \Delta k_{20}^{52} = 2.65 \times 10^{-5}$	16.52, 16.58
(3,3)	$\Delta k_{22}^{55} = 3.22 \times 10^{-5}, \Delta k_{20}^{33} = 5.02 \times 10^{-5}$	13.62, 8.77

5

Conclusions & Discussions

This chapter reflects on the findings and aims to answer the research question posed in Section 2.4. The results of the covariance analysis and sensitivity study in Chapters 3 and 4 are summarized and linked to the research question in Section 5.1. A discussion on the implications of this research in a broader sense and recommendations for future work are detailed in Section 5.2.

5.1. Summary & Conclusions

The main goal of this thesis was to investigate whether JUICE measurements will be precise enough to constrain lateral variations in the thickness of Ganymede's ice shell. In Chapter 3, the concept of mode coupled Love numbers was implemented into the time-varying gravity field functionality of Tudat. These mode coupled Love number arise specifically if Ganymede has lateral variations in its interior properties and differ substantially from the typical diagonal Love numbers (eg. k_{2m}^{2m} induced by a degree 2 forcing). Using simulated range and Doppler observations during the GCO500 phase, a covariance analysis was set up to obtain the expected uncertainties with which JUICE is able to observe these tidal effects. In Chapter 4, an interior model of Ganymede was built, consistent with the latest state of knowledge about Ganymede. A sensitivity analysis of Love numbers to the interior properties of Ganymede was done to assess which additional signals would arise if lateral variations are present in Ganymede and how sensitive these are to the interior. These findings allow to reflect back on the research questions:

What is the expected uncertainty in observing the additional tidal signals, and if it is low enough, which response modes could be observed?

The results show show that the spherically-symmetric degree 3 Love number can be estimated with an uncertainty of $\sigma_{k_3} = 0.03$ and off-diagonal degree 3 Love numbers have an uncertainty of $\sigma_{k_{3m}^{3m}}$ 0.1. Comparing this to the Love number $k_3 = 0.281$, the degree 3 Love numbers are at the verge of detectability. The degree 2 diagonal Love numbers have an uncertainty of $\sigma_{k_{20}^{20}}$ $4.4 \cdot 10^{-4}$ and $\sigma_{k_{20}^{20}}$ $2.05 \cdot 10^{-4}$. JUICE is also sensitive to the off-diagonal terms (eg. k_{20}^{30} and k_{22}^{32}) and the uncertainty of higher order responses is in the same order of magnitude as the degree 2 response ($\sigma_{k_{2m}^{2m}} \approx \sigma_{k_{2m}^{3m}} \approx \sigma_{k_{2m}^{4m}}$). The contributing of Love numbers at different forcing wavelengths to the same response mode, lead to correlation and makes the estimation process difficult. Correlated parameters such as k_{20}^{20} and k_{22}^{20} result in large uncertainties as JUICE cannot recover the individual tidal contributions. JUICE is able to distinguish the signals in the response of the C_{22} coefficient but not for C_{20}, which could be due to the orbit geometry and observability of the tides. Comparing the covariance results with the expected response induced in the gravity field coefficients shows that zonal lateral variations have the highest change of being detectable, while higher order responses seemed to have an overly optimistic sensitivity.

What additional tidal contributions are expected for Ganymede assuming an interior with lateral variations?

As response to a degree 2 forcing of Jupiter on a Ganymede with spherically symmetric interior properties, the main tidal signal arising is $k_2 = 0.469$. It was found that in the presence of lateral variations, additional tidal signals arise ($\Delta k^{n,m}_{n_\alpha,n_\beta}$) on top of the main tidal signal. These additional tidal signals depend on the amplitude, wavelength (degree/order) and location of lateral variations in the interior.

The magnitude of additional tidal signals increases with the amplitude of lateral variations, with first-order responses consistently dominating the spectrum. For ice shell thickness variations of 1% the additional signals produced range from roughly 1×10^{-4} to 1×10^{-10}. Each type of lateral variation (degree/order) generates a unique response, with more complex structures inducing a broader range of response modes. However, higher-order responses exhibit diminishing amplitudes, reducing their potential detectability.

Tidal signals with the highest amplitudes primarily result from the degree 1 and degree 2 lateral variations within the ice shell. Notably, the largest additional signals are associated with zonal variations (order = 0) in the ice shell, which lack longitudinal dependence. The leading tidal signals reach magnitudes close to the expected uncertainty of JUICE's tidal measurements.

How sensitive are the tidal signals to changes in the interior parameters?

The type of signals expected depends on the coupling of the degree 2 forcing with the lateral variation type. Common to all types are responses at multiples of the forcing (e.g. (2,0), (2,2), (4,0), (4,2) etc.). degree 1 variations exhibit a strong degree 3 response, degree 2 variations produce strong degree 4 signals, and degree 3 variations yield the strongest signals at degrees 3 and 5.

The analysis highlighted the critical role of the ice shell, which is most sensitive to lateral variations, whereas the deep interior produces significantly smaller signals approximately an order of magnitude lower for the mantle and two orders of magnitude lower for the high-pressure ice layer. Consequently, any combined effects of lateral variations in both the mantle and ice shell do not significantly influence the results, as the ice shell dominates the overall tidal response, see Figures 4.11a and 4.11b. For the mantle to have a comparable impact, it would require unrealistically large amplitudes of thickness variations.

Does the observational error during JUICE's GCO500 phase allow to realistically observe higher order components (degree > 2) of Ganymede's tidal response?

The most realistic tidal signals that JUICE could observe are the responses $k^{2,0}_{2,0}$, $k^{2,2}_{2,2}$, $k^{3,0}_{2,0}$ and $k^{3,2}_{2,2}$, corresponding to zonal lateral variations. If the amplitude of thickness variations in the ice shell is at least $\Delta H \approx 5\%$ these signals are on the verge of detectability. This corresponds to lateral variations of type (2,0) and (1,0), thus a flattening of the ice shell around the equator of Ganymede or a polar dichotomy in the ice shell. The results of the covariance analysis are certainly optimistic and suggest that uncertainty of higher order components of the tidal response is around $\sigma \approx 4.4 \times 10^{-4}$. With this uncertainty, an ice shell with a more complicated spatial structure needs to have an amplitude of $\Delta H \approx 6 - 15\%$ to produce signals that can be detected by JUICE.

The amplitude and wavelength of potential lateral variations on Ganymede is not known, but examples have been seen other icy moons such as Europa and Enceladus and lateral variations of 5% are not unrealistic to expect.

5.2. Discussions & Future Work

In a broader context, this research contributes to the goal of using tidal tomography to recover lateral variations in the interior of a body from spacecraft gravity field observations. Measuring the off-diagonal Love number responses allows to obtain information about lateral variations due to the mode coupling of response modes. While this research investigated to what extent the expected signals are detectable, the next step would be to use these uncertainties in a type of statistical inversion to recover the type and amplitude of lateral variations given the observed gravity response on JUICE. The use of tidal tomography for the exploration of icy moons is an exciting opportunity to constrain more complex information about the ice shell from an orbiting spacecraft. Information about the lateral structure of the ice shell is relevant to understand the exchange of material between the ocean and shell, the ocean dynamics and tidal heating distribution. These processes are key to assess the habitability of a subsurface ocean.

During the research, the following areas of improvement have been identified, that could not be included mainly due to time constraints:

The GCO500 phase was used as basis for all simulations and the covariance analysis and uncertainties were calculated for an orbit altitude of 500 km. Following a well performed launch of JUICE, an additional phase of 30 days at an even lower altitude of 200 km is confirmed. Since the gravity field and tidal effects are stronger at lower altitude, the estimation of mode coupled Love numbers and uncertainties in gravity field coefficients and their time variability would greatly benefit. Thus, a future analysis of results should include the confirmed GCO200 phase in assessing the sensitivity of JUICE to observe lateral variations.

The estimation of Love numbers caused correlation problems during the covariance analysis, where the contributions of two forcing wavelengths flowing into the same gravity signal response could not be distinguished by JUICE. An example was the gravity field coefficient C_{20}, where time-varying tidal effects from a forcing at (2,0) and (2,2) contribute to a response. Estimating the corresponding Love numbers k_{20}^{20} and k_{22}^{20} lead to high correlation and large uncertainties. For future estimations, a different parametrization could be chosen that does not estimate only Love numbers but the time-varying gravity signals them selves.

This could be done by estimating the time-varying gravity field coefficients with $\Delta C_{nm}(t) = \Delta C_{nm}^{A} \cdot cos(nt)$ where C_{nm}^{A} is the amplitude and would include the effects of k_{20}^{20} and k_{22}^{20}. Another idea could be to estimate these Love numbers jointly and imposing constraints in the estimation process, such as estimating $Ak_{20}^{20} + Bk_{22}^{20}$, where A and B are coefficients relating the correlated Love numbers.

References

A, G., Wahr, J., & Zhong, S. (2014). The effects of laterally varying icy shell structure on the tidal response of Ganymede and Europa. *Journal of Geophysical Research: Planets*, *119*(3), 659–678. https://doi.org/10.1002/2013JE004570

Anderson, J. D., Lau, E. L., Sjogren, W. L., Schubert, G., & Moore, W. B. (1996). Gravitational constraints on the internal structure of Ganymede. *Nature*, *384*(6609), 541–543. https://doi.org/10.1038/384541a0

Anderson, J. D., Schubert, G., Jacobson, R. A., Lau, E. L., Moore, W. B., & Palguta, J. L. (2004). Discovery of Mass Anomalies on Ganymede. *Science*, *305*(5686), 989–991. https://doi.org/10.1126/science.1099050

Bagheri, A., Efroimsky, M., Castillo-Rogez, J., Goossens, S., Plesa, A.-C., Rambaux, N., Rhoden, A., Walterová, M., Khan, A., & Giardini, D. (2022). Tidal insights into rocky and icy bodies: An introduction and overview. In *Advances in Geophysics* (pp. 231–320, Vol. 63). Elsevier. https://doi.org/10.1016/bs.agph.2022.07.004

Baland, R.-M., Yseboodt, M., & Hoolst, T. V. (2012). Obliquity of the Galilean satellites: The influence of a global internal liquid layer. *Icarus*, *220*(2), 435–448. https://doi.org/10.1016/j.icarus.2012.05.020

Berne, A., Simons, M., Keane, J. T., & Park, R. S. (2023a). Using Tidally-Driven Elastic Strains to Infer Regional Variations in Crustal Thickness at Enceladus. *Geophysical Research Letters*, *50*(22), e2023GL106656. https://doi.org/10.1029/2023GL106656

Berne, A., Simons, M., Keane, J. T., & Park, R. S. (2023b). Inferring the Mean Thickness of the Outer Ice Shell of Enceladus From Diurnal Crustal Deformation. *Journal of Geophysical Research: Planets*, *128*(6), e2022JE007712. https://doi.org/10.1029/2022JE007712

Bertotti, B. & Comoretto, G. (1993). Doppler tracking of spacecraft with multi-frequency links. *Astronomy and Astrophysics*, *269*(1-2), 608–616.

Beuthe, M. (2018). Enceladus's crust as a non-uniform thin shell: I tidal deformations. *Icarus*, *302*, 145–174. https://doi.org/10.1016/j.icarus.2017.11.009

Beuthe, M., Rivoldini, A., & Trinh, A. (2016). Enceladus's and Dione's floating ice shells supported by minimum stress isostasy. *Geophysical Research Letters*, *43*(19). https://doi.org/10.1002/2016GL070650

Bland, M. T., Showman, A. P., & Tobie, G. (2009). The orbital–thermal evolution and global expansion of Ganymede. *Icarus*, *200*(1), 207–221. https://doi.org/10.1016/j.icarus.2008.11.016

Boutonnet, A., Langevin, Y., & Erd, C. (2024). Designing the JUICE Trajectory. *Space Science Reviews*, *220*(6), 67. https://doi.org/10.1007/s11214-024-01093-y

Čadek, O., Souček, O., Běhounková, M., Choblet, G., Tobie, G., & Hron, J. (2019). Long-term stability of Enceladus' uneven ice shell. *Icarus*, *319*, 476–484. https://doi.org/10.1016/j.icarus.2018.10.003

Campbell, J. K., & Synnott, S. P. (1985). Gravity field of the Jovian system from Pioneer and Voyager tracking data. *The Astronomical Journal*, *90*, 364. https://doi.org/10.1086/113741

Cappuccio, P., Hickey, A., Durante, D., Di Benedetto, M., Iess, L., De Marchi, F., Plainaki, C., Milillo, A., & Mura, A. (2020). Ganymede's gravity, tides and rotational state from JUICE's 3GM experiment simulation. *Planetary and Space Science*, *187*, 104902. https://doi.org/10.1016/j.pss.2020.104902

Cappuccio, P., Sesta, A., Di Benedetto, M., Durante, D., De Filippis, U., Di Stefano, I., Iess, L., Mackenzie, R., & Godard, B. (2025). Analysis of Radio Science Data from the KaT Instrument of the 3GM Experiment During JUICE's Early Cruise Phase. *Aerospace*, *12*(1), 56. https://doi.org/10.3390/aerospace12010056

Choukroun, M., & Grasset, O. (2010). Thermodynamic data and modeling of the water and ammonia-water phase diagrams up to 2.2 GPa for planetary geophysics. *The Journal of Chemical Physics*, *133*(14), 144502. https://doi.org/10.1063/1.3487520

Crary, F. J., & Bagenal, F. (1998). Remanent ferromagnetism and the interior structure of Ganymede. *Journal of Geophysical Research: Planets*, *103*(E11), 25757–25773. https://doi.org/10.1029/98JE02497

De Marchi, F., Cappuccio, P., Mitri, G., & Iess, L. (2022). Frequency-dependent Ganymede's tidal Love number k 2 detection by JUICE's 3GM experiment and implications for the subsurface ocean thickness. *Icarus*, *386*, 115150. https://doi.org/10.1016/j.icarus.2022.115150

Dirkx, D., Lainey, V., Gurvits, L., & Visser, P. (2016). Dynamical modelling of the Galilean moons for the JUICE mission. *Planetary and Space Science*, *134*, 82–95. https://doi.org/10.1016/j.pss.2016.10.011

Downey, B. G., Nimmo, F., & Matsuyama, I. (2020). Inclination damping on Callisto. *Monthly Notices of the Royal Astronomical Society*, *499*(1), 40–51. https://doi.org/10.1093/mnras/staa2802

Durante, D., Hemingway, D., Racioppa, P., Iess, L., & Stevenson, D. (2019). Titan's gravity field and interior structure after Cassini. *Icarus*, *326*, 123–132. https://doi.org/10.1016/j.icarus.2019.03.003

Gomez Casajus, L., Ermakov, A. I., Zannoni, M., Keane, J. T., Stevenson, D., Buccino, D. R., Durante, D., Parisi, M., Park, R. S., Tortora, P., & Bolton, S. J. (2022). Gravity Field of Ganymede After the *Juno* Extended Mission. *Geophysical Research Letters*, *49*(24), e2022GL099475. https://doi.org/10.1029/2022GL099475

Grasset, O., Dougherty, M., Coustenis, A., Bunce, E., Erd, C., Titov, D., Blanc, M., Coates, A., Drossart, P., Fletcher, L., Hussmann, H., Jaumann, R., Krupp, N., Lebreton, J.-P., Prieto-Ballesteros, O., Tortora, P., Tosi, F., & Van Hoolst, T. (2013). JUpiter ICy moons Explorer (JUICE): An ESA mission to orbit Ganymede and to characterise the Jupiter system. *Planetary and Space Science*, *78*, 1–21. https://doi.org/10.1016/j.pss.2012.12.002

Gurnett, D. A., Kurth, W. S., Roux, A., Bolton, S. J., & Kennel, C. F. (1996). Evidence for a magnetosphere at Ganymede from plasma-wave observations by the Galileo spacecraft. *Nature*, *384*(6609), 535–537. https://doi.org/10.1038/384535a0

Hammond, N. P., & Barr, A. C. (2014). Formation of Ganymede's grooved terrain by convection-driven resurfacing. *Icarus*, *227*, 206–209. https://doi.org/10.1016/j.icarus.2013.08.024

Hansen, C. J., Bolton, S., Sulaiman, A. H., Duling, S., Bagenal, F., Brennan, M., Connerney, J., Clark, G., Lunine, J., Levin, S., Kurth, W., Mura, A., Paranicas, C., Tosi, F., & Withers, P. (2022). Juno's Close Encounter With Ganymede—An Overview. *Geophysical Research Letters*, *49*(23), e2022GL099285. https://doi.org/10.1029/2022GL099285

Helled, R., Anderson, J. D., Schubert, G., & Stevenson, D. J. (2011). Jupiter's moment of inertia: A possible determination by Juno. *Icarus*, *216*(2), 440–448. https://doi.org/10.1016/j.icarus.2011.09.016

Hendrix, A. R., Hurford, T. A., Barge, L. M., Bland, M. T., Bowman, J. S., Brinckerhoff, W., Buratti, B. J., Cable, M. L., Castillo-Rogez, J., Collins, G. C., Diniega, S., German, C. R., Hayes, A. G., Hoehler, T., Hosseini, S., Howett, C. J., McEwen, A. S., Neish, C. D., Neveu, M., . . . Vance, S. D. (2019). The NASA Roadmap to Ocean Worlds. *Astrobiology*, *19*(1), 1–27. https://doi.org/10.1089/ast.2018.1955

Hoppa, G., Greenberg, R., Geissler, P., Tufts, B., Plassmann, J., & Durda, D. D. (1999). Rotation of Europa: Constraints from Terminator and Limb Positions. *Icarus*, *137*(2), 341–347. https://doi.org/10.1006/icar.1998.6065

Hoppa, G. V., Tufts, B. R., Greenberg, R., & Geissler, P. E. (1999). Formation of Cycloidal Features on Europa. *Science*, *285*(5435), 1899–1902. https://doi.org/10.1126/science.285.5435.1899

Hussmann, H., Shoji, D., Steinbrügge, G., Stark, A., & Sohl, F. (2016). Constraints on dissipation in the deep interiors of Ganymede and Europa from tidal phase-lags. *Celestial Mechanics and Dynamical Astronomy*, *126*(1-3), 131–144. https://doi.org/10.1007/s10569-016-9721-0

Jara-Orué, H. M., & Vermeersen, B. L. (2011). Effects of low-viscous layers and a non-zero obliquity on surface stresses induced by diurnal tides and non-synchronous rotation: The case of Europa. *Icarus*, *215*(1), 417–438. https://doi.org/10.1016/j.icarus.2011.05.034

Jara-Orué, H., & Vermeersen, B. (2016). Tides on Jupiter's moon Ganymede and their relation to its internal structure. *Netherlands Journal of Geosciences - Geologie en Mijnbouw*, *95*(2), 191–201. https://doi.org/10.1017/njg.2015.23

Journaux, B., Kalousová, K., Sotin, C., Tobie, G., Vance, S., Saur, J., Bollengier, O., Noack, L., Rückriemen-Bez, T., Van Hoolst, T., Soderlund, K. M., & Brown, J. M. (2020). Large Ocean Worlds with High-Pressure Ices. *Space Science Reviews*, *216*(1), 7. https://doi.org/10.1007/s11214-019-0633-7

Kamata, S., Kimura, J., Matsumoto, K., Nimmo, F., Kuramoto, K., & Namiki, N. (2016). Tidal deformation of Ganymede: Sensitivity of Love numbers on the interior structure. *Journal of Geophysical Research: Planets*, *121*(7), 1362–1375. https://doi.org/10.1002/2016JE005071

Kamata, S., Matsuyama, I., & Nimmo, F. (2015). Tidal resonance in icy satellites with subsurface oceans. *Journal of Geophysical Research: Planets*, *120*(9), 1528–1542. https://doi.org/10.1002/2015JE004821

Kaula, W. M. (1964). Tidal dissipation by solid friction and the resulting orbital evolution. *Reviews of Geophysics*, *2*(4), 661–685. https://doi.org/10.1029/RG002i004p00661

Kaula, W. M. (1966). *Theory of satellite geodesy*. Blaisdell.

Kivelson, M. G., Khurana, K. K., Russell, C. T., Walker, R. J., Warnecke, J., Coroniti, F. V., Polanskey, C., Southwood, D. J., & Schubert, G. (1996). Discovery of Ganymede's magnetic field by the Galileo spacecraft. *Nature*, *384*(6609), 537–541. https://doi.org/10.1038/384537a0

Kivelson, M., Khurana, K., & Volwerk, M. (2002). The Permanent and Inductive Magnetic Moments of Ganymede. *Icarus*, *157*(2), 507–522. https://doi.org/10.1006/icar.2002.6834

Kuskov, O. (2001). Core Sizes and Internal Structure of Earth's and Jupiter's Satellites. *Icarus*, *151*(2), 204–227. https://doi.org/10.1006/icar.2001.6611

Lau, H. C. P., Mitrovica, J. X., Davis, J. L., Tromp, J., Yang, H.-Y., & Al-Attar, D. (2017). Tidal tomography constrains Earth's deep-mantle buoyancy. *Nature*, *551*(7680), 321–326. https://doi.org/10.1038/nature24452

Love, A. (1911). *Some Problems of Geodynamics*. Cambridge University Press.

Martins, Z. et al. (2021). Report of the Expert Committee for the Large-class mission in ESA's Voyage 2050 plan covering the science theme Moons of the Giant Planets.

McCarthy, C., & Castillo-Rogez, J. C. (2013). Planetary ices attenuation properties. In M. S. Gudipati & J. Castillo-Rogez (Eds.), *The science of solar system ices* (pp. 183–225). Springer New York. https://doi.org/10.1007/978-1-4614-3076-6_7

McKinnon, W. B., & Desai, S. S. (2003). Internal structures of the galilean satellites: What can we really tell?

Mitri, G., Meriggiola, R., Hayes, A., Lefevre, A., Tobie, G., Genova, A., Lunine, J. I., & Zebker, H. (2014). Shape, topography, gravity anomalies and tidal deformation of Titan. *Icarus*, *236*, 169–177. https://doi.org/10.1016/j.icarus.2014.03.018

Montenbruck, O., & Gill, E. (2000). *Satellite Orbits: Models, Methods, and Applications*. Springer.

Moore, W. B., & Schubert, G. (2003). The tidal response of Ganymede and Callisto with and without liquid water oceans. *Icarus*, *166*(1), 223–226. https://doi.org/10.1016/j.icarus.2003.07.001

Mueller, S., & McKinnon, W. B. (1988). Three-layered models of Ganymede and Callisto: Compositions, structures, and aspects of evolution. *Icarus*, *76*(3), 437–464. https://doi.org/10.1016/0019-1035(88)90014-0

Nimmo, F., Thomas, P., Pappalardo, R., & Moore, W. (2007). The global shape of Europa: Constraints on lateral shell thickness variations. *Icarus*, *191*(1), 183–192. https://doi.org/10.1016/j.icarus.2007.04.021

Notaro, V., Durante, D., & Iess, L. (2019). On the determination of Jupiter's satellite-dependent Love numbers from Juno gravity data. *Planetary and Space Science*, *175*, 34–40. https://doi.org/10.1016/j.pss.2019.06.001

Null, G. W. (1976). Gravity field of Jupiter and its satellite from Pioneer 10 and Pioneer 11 tracking data. *The Astronomical Journal*, *81*, 1153. https://doi.org/10.1086/111999

Ojakangas, G. (1989). Thermal state of an ice shell on Europa. *Icarus*, *81*(2), 220–241. https://doi.org/10.1016/0019-1035(89)90052-3

Padovan, S., Margot, J.-L., Hauck, S. A., Moore, W. B., & Solomon, S. C. (2014). The tides of Mercury and possible implications for its interior structure. *Journal of Geophysical Research: Planets*, *119*(4), 850–866. https://doi.org/10.1002/2013JE004459

Palguta, J., Anderson, J. D., Schubert, G., & Moore, W. B. (2006). Mass anomalies on Ganymede. *Icarus*, *180*(2), 428–441. https://doi.org/10.1016/j.icarus.2005.08.020

Palguta, J., Schubert, G., Zhang, K., & Anderson, J. D. (2009). Constraints on the location, magnitude, and dimensions of Ganymede's mass anomalies. *Icarus*, *201*(2), 615–625. https://doi.org/10.1016/j.icarus.2009.02.004

Parisi, M., Finocchiaro, S., & Iess, L. (2012). Multi-arc and batch-sequential filters for the orbit determination of ESA's JUICE mission.

Park, R. S., Jacobson, R. A., Gomez Casajus, L., Nimmo, F., Ermakov, A. I., Keane, J. T., McKinnon, W. B., Stevenson, D. J., Akiba, R., Idini, B., Buccino, D. R., Magnanini, A., Parisi, M., Tortora, P., Zannoni, M., Mura, A., Durante, D., Iess, L., Connerney, J. E. P., . . . Bolton, S. J. (2024). Io's tidal response precludes a shallow magma ocean. *Nature*. https://doi.org/10.1038/s41586-024-08442-5

Park, R. S., Asmar, S. W., Buffington, B. B., Bills, B., Campagnola, S., Chodas, P. W., Folkner, W. M., Konopliv, A. S., & Petropoulos, A. E. (2011). Detecting tides and gravity at Europa from multiple

close flybys: DETECTING TIDES AND GRAVITY AT EUROPA. *Geophysical Research Letters*, *38*(24), n/a–n/a. https://doi.org/10.1029/2011GL049842

Petit, G., & Luzum, B. (2010). *(IERS Technical Note; No. 36)* (tech. rep.).

Plainaki, C., Milillo, A., Massetti, S., Mura, A., Jia, X., Orsini, S., Mangano, V., De Angelis, E., & Rispoli, R. (2015). The H2O and O2 exospheres of Ganymede: The result of a complex interaction between the jovian magnetospheric ions and the icy moon. *Icarus*, *245*, 306–319. https://doi.org/10.1016/j.icarus.2014.09.018

Qin, C., Zhong, S., & Wahr, J. (2014). A perturbation method and its application: Elastic tidal response of a laterally heterogeneous planet. *Geophysical Journal International*, *199*(2), 631–647. https://doi.org/10.1093/gji/ggu279

Renaud, J. P., & Henning, W. G. (2018). Increased Tidal Dissipation Using Advanced Rheological Models: Implications for Io and Tidally Active Exoplanets. *The Astrophysical Journal*, *857*(2), 98. https://doi.org/10.3847/1538-4357/aab784

Ritsema, J., Deuss, A., Van Heijst, H. J., & Woodhouse, J. H. (2011). S40RTS: A degree-40 shear-velocity model for the mantle from new Rayleigh wave dispersion, teleseismic traveltime and normal-mode splitting function measurements: S40RTS. *Geophysical Journal International*, *184*(3), 1223–1236. https://doi.org/10.1111/j.1365-246X.2010.04884.x

Rovira-Navarro, M. (2022). *Tidal Dynamics of Moons with Fluid Layers* [Doctoral dissertation].

Rovira-Navarro, M., Matsuyama, I., & Berne, A. (2024). A Spectral Method to Compute the Tides of Laterally Heterogeneous Bodies. *The Planetary Science Journal*, *5*(5), 129. https://doi.org/10.3847/PSJ/ad381f

Sabadini, R., & Vermeersen, B. (2004). *Global Dynamics of the Earth* (Vol. 20). Springer Netherlands. https://doi.org/10.1007/978-94-017-1709-0

Sabadini, R., Vermeersen, Bert, & Cambiotti, Gabriele. (2016). *Global Dynamics of the Earth: Applications of Viscoelastic Relaxation Theory to Solid-Earth and Planetary Geophysics*. Springer Netherlands. https://doi.org/10.1007/978-94-017-7552-6

Saur, J., Duling, S., Roth, L., Jia, X., Strobel, D. F., Feldman, P. D., Christensen, U. R., Retherford, K. D., McGrath, M. A., Musacchio, F., Wennmacher, A., Neubauer, F. M., Simon, S., & Hartkorn, O. (2015). The search for a subsurface ocean in Ganymede with Hubble Space Telescope observations of its auroral ovals. *Journal of Geophysical Research: Space Physics*, *120*(3), 1715–1737. https://doi.org/10.1002/2014JA020778

Schenk, P. M. (2002). Thickness constraints on the icy shells of the galilean satellites from a comparison of crater shapes. *Nature*, *417*(6887), 419–421. https://doi.org/10.1038/417419a

Schubert, G., Spohn, T., & McKinnon, W. B. (2004). Interior Composition, Structure and Dynamics of the Galilean Satellites.

Schubert, G., Stevenson, D., & Ellsworth, K. (1981). Internal structures of the Galilean satellites. *Icarus*, *47*(1), 46–59. https://doi.org/10.1016/0019-1035(81)90090-7

Schubert, G., Zhang, K., Kivelson, M. G., & Anderson, J. D. (1996). The magnetic field and internal structure of Ganymede. *Nature*, *384*(6609), 544–545. https://doi.org/10.1038/384544a0

Singer, K. N., Bland, M. T., Schenk, P. M., & McKinnon, W. B. (2018). Relaxed impact craters on Ganymede: Regional variation and high heat flows. *Icarus*, *306*, 214–224. https://doi.org/10.1016/j.icarus.2018.01.012

Soderlund, K. M., Kalousová, K., Buffo, J. J., Glein, C. R., Goodman, J. C., Mitri, G., Patterson, G. W., Postberg, F., Rovira-Navarro, M., Rückriemen, T., Saur, J., Schmidt, B. E., Sotin, C., Spohn, T., Tobie, G., Van Hoolst, T., Vance, S. D., & Vermeersen, B. (2020). Ice-Ocean Exchange Processes in the Jovian and Saturnian Satellites. *Space Science Reviews*, *216*(5), 80. https://doi.org/10.1007/s11214-020-00706-6

Soderlund, K. M., Rovira-Navarro, M., Le Bars, M., Schmidt, B. E., & Gerkema, T. (2024). The Physical Oceanography of Ice-Covered Moons. *Annual Review of Marine Science*, *16*(1), 25–53. https://doi.org/10.1146/annurev-marine-040323-101355

Sohl, F., Solomonidou, A., Wagner, F. W., Coustenis, A., Hussmann, H., & Schulze-Makuch, D. (2014). Structural and tidal models of Titan and inferences on cryovolcanism. *Journal of Geophysical Research: Planets*, *119*(5), 1013–1036. https://doi.org/10.1002/2013JE004512

Sohl, F., Spohn, T., Breuer, D., & Nagel, K. (2002). Implications from Galileo Observations on the Interior Structure and Chemistry of the Galilean Satellites. *Icarus*, *157*(1), 104–119. https://doi.org/10.1006/icar.2002.6828

Spohn, T., & Schubert, G. (2003). Oceans in the icy Galilean satellites of Jupiter? *Icarus*, *161*(2), 456–467. https://doi.org/10.1016/S0019-1035(02)00048-9

Steinbrügge, G., Padovan, S., Hussmann, H., Steinke, T., Stark, A., & Oberst, J. (2018). Viscoelastic Tides of Mercury and the Determination of its Inner Core Size. *Journal of Geophysical Research: Planets*, *123*(10), 2760–2772. https://doi.org/10.1029/2018JE005569

Steinbrügge, G., Stark, A., Hussmann, H., Sohl, F., & Oberst, J. (2015). Measuring tidal deformations by laser altimetry. A performance model for the Ganymede Laser Altimeter. *Planetary and Space Science*, *117*, 184–191. https://doi.org/10.1016/j.pss.2015.06.013

Steinke, T., Hu, H., Höning, D., Van Der Wal, W., & Vermeersen, B. (2020). Tidally induced lateral variations of Io's interior. *Icarus*, *335*, 113299. https://doi.org/10.1016/j.icarus.2019.05.001

Van Hoolst, T., Baland, R.-M., & Trinh, A. (2013). On the librations and tides of large icy satellites. *Icarus*, *226*(1), 299–315. https://doi.org/10.1016/j.icarus.2013.05.036

Van Hoolst, T., Tobie, G., Vallat, C., Altobelli, N., Bruzzone, L., Cao, H., Dirkx, D., Genova, A., Hussmann, H., Iess, L., Kimura, J., Khurana, K., Lucchetti, A., Mitri, G., Moore, W., Saur, J., Stark, A., Vorburger, A., Wieczorek, M., … Witasse, O. (2024). Geophysical Characterization of the Interiors of Ganymede, Callisto and Europa by ESA's JUpiter ICy moons Explorer. *Space Science Reviews*, *220*(5), 54. https://doi.org/10.1007/s11214-024-01085-y

Vance, S., Bouffard, M., Choukroun, M., & Sotin, C. (2014). Ganymedes internal structure including thermodynamics of magnesium sulfate oceans in contact with ice. *Planetary and Space Science*, *96*, 62–70. https://doi.org/10.1016/j.pss.2014.03.011

Vance, S. D., Panning, M. P., Stähler, S., Cammarano, F., Bills, B. G., Tobie, G., Kamata, S., Kedar, S., Sotin, C., Pike, W. T., Lorenz, R., Huang, H.-H., Jackson, J. M., & Banerdt, B. (2018). Geophysical Investigations of Habitability in Ice-Covered Ocean Worlds. *Journal of Geophysical Research: Planets*, *123*(1), 180–205. https://doi.org/10.1002/2017JE005341

Wagner, F. W., Sohl, F., & Hussmann, H. (2013). Physical Structure and Tidal Distortion of Ganymede: Implications for the JUICE mission.

Wahr, J. M., Zuber, M. T., Smith, D. E., & Lunine, J. I. (2006). Tides on Europa, and the thickness of Europa's icy shell. *Journal of Geophysical Research: Planets*, *111*(E12), 2006JE002729. https://doi.org/10.1029/2006JE002729

Wahr, J., Selvans, Z. A., Mullen, M. E., Barr, A. C., Collins, G. C., Selvans, M. M., & Pappalardo, R. T. (2009). Modeling stresses on satellites due to nonsynchronous rotation and orbital eccentricity using gravitational potential theory. *Icarus*, *200*(1), 188–206. https://doi.org/10.1016/j.icarus.2008.11.002

Watters, T. R., McGovern, P. J., & Irwin Iii, R. P. (2007). Hemispheres Apart: The Crustal Dichotomy on Mars. *Annual Review of Earth and Planetary Sciences*, *35*(1), 621–652. https://doi.org/10.1146/annurev.earth.35.031306.140220

Wieczorek, M. A., Neumann, G. A., Nimmo, F., Kiefer, W. S., Taylor, G. J., Melosh, H. J., Phillips, R. J., Solomon, S. C., Andrews-Hanna, J. C., Asmar, S. W., Konopliv, A. S., Lemoine, F. G., Smith, D. E., Watkins, M. M., Williams, J. G., & Zuber, M. T. (2013). The Crust of the Moon as Seen by GRAIL. *Science*, *339*(6120), 671–675. https://doi.org/10.1126/science.1231530

Williams, J. G., & Boggs, D. H. (2015). Tides on the Moon: Theory and determination of dissipation. *Journal of Geophysical Research: Planets*, *120*(4), 689–724. https://doi.org/10.1002/2014JE004755

Zerilli, F. J. (1970). Tensor Harmonics in Canonical Form for Gravitational Radiation and Other Applications. *Journal of Mathematical Physics*, *11*(7), 2203–2208. https://doi.org/10.1063/1.1665380

Zhong, S., Qin, C., A, G., & Wahr, J. (2012). Can tidal tomography be used to unravel the long-wavelength structure of the lunar interior? *Geophysical Research Letters*, *39*(15), 2012GL052362. https://doi.org/10.1029/2012GL052362